Optical Spectroscopy on Single and Coupled Microspheres Doped With Semiconductor Nanocrystals

Dissertation
zur Erlangung des Grades eines
Doktors der Naturwissenschaften
des Fachbereichs Physik
der Universität Dortmund

vorgelegt von
Dipl.-Phys. Björn Möller
aus Unna

Universität Dortmund
Experimentelle Physik IIb
November 2005

Vom Fachbereich Physik der Universität Dortmund
als Dissertation angenommen.

Tag der mündlichen Prüfung:	14.12.2005
Dekan:	Prof. Dr. M. Tolan
Erste Gutachterin:	Prof. Dr. U. Woggon
Zweiter Gutachter:	Prof. Dr. K. Wille
Vertretung der promovierten wissenschaftlichen Mitarbeiter:	Dr. C. Sternemann

Publications on the Subject

Articles in Refereed Journals

1. **Photons in Coupled Microsphere Resonators**
   B. Möller, U. Woggon, and M. V. Artemyev,
   accepted for publication in J. Opt. A: Pure Appl. Opt., invited (2005)

2. **Coupled-Resonator Optical Waveguides (CROWs) Doped With Nanocrystals**
   B. M. Möller, U. Woggon, and M. V. Artemyev,
   Opt. Lett. **30** (16), 2116 (2005)

3. **Photonic Molecules Doped With Semiconductor Nanocrystals**
   B. M. Möller, M. V. Artemyev, U. Woggon, and R. Wannemacher,
   Phys. Rev. B **70** (11), 115323 (2004)
   (selected for the Virtual Journal of Nanoscale Science & Technology, **10** (15) (2004))

4. **Mode Control by Nanoengineering Light Emitters in Spherical Microcavities**
   B. Möller, M. V. Artemyev, U. Woggon, and R. Wannemacher,
   Appl. Phys. Lett. **83** (16), 2686-2688, 2003
   (selected for the Virtual Journal of Nanoscale Science & Technology, **8** (14) (2003))

5. **Mode identification in spherical microcavities doped with quantum dots**
   B. Möller, M. V. Artemyev, U. Woggon, and R. Wannemacher,
   Appl. Phys. Lett. **80** (18), 3253-3255, 2002
   (selected for the Virtual Journal of Nanoscale Science & Technology, **5** (19) (2002))

6. **Unidirectional Alignment of CdSe nanorods**
   Mikhail Artemyev, Björn Möller, and Ulrike Woggon, Nano Lett. **3** (4), 509-512 (2003)

7. **Dot-in-a-dot: Electronic and Photonic Confinement in all Three Dimensions**
   U. Woggon, R. Wannemacher, M. V. Artemyev, B. Möller, N. LeThomas, V. Anikeyev, and O. Schöps, Appl. Phys. B **77**, 469-484 (2003)

Refereed Contributions to International Conferences

8. **Coupled-Resonator Optical Waveguides (CROWs) Doped With Semiconductor Quantum Dots**,
   B. Möller, U. Woggon, M. V. Artemyev,
   CLEO/IQEC 2005 (QWA5), Baltimore, 2005 (oral)

9. **Nanocrystal-doped Polymer Spheres as Building Blocks for Coupled Resonator Optical Waveguides**,
   B. Möller, U. Woggon, M. V. Artemyev,
   Photonics West 2005 (5708-45), San Jose, 2005 (oral))
   SPIE Proceedings, Vol. 5708, 271-277 (2005),

10. **Photonic Molecules Doped With Quantum Dots**,
    B. Möller, U. Woggon, M. V. Artemyev, and R. Wannemacher,
    CLEO/IQEC 2004 (IWD4), San Francisco, 2004 (oral)

11. **Nanocrystals for Controlling Photons in Single and Coupled Microspheres**,
    B. M. Möller, M. V. Artemyev, R. Wannemacher, and U. Woggon,
    Quantum Dot Conference QD 2004 (WP 22), Banff, 2004

12. **Spectroscopy of Single CdSe Nanorods**,
    N. LeThomas, O. Schöps, B. Möller, M. V. Artemyev, and U. Woggon,
    CLEO/IQEC 2004 (IThF6), San Francisco, 2004 (oral)

13. **Nanocrystals for controlling photons in single and coupled microspheres**,
    U. Woggon, B. Möller, and M. V. Artemyev,
    ACS Meeting 2004 (E 140), Anaheim, 2004 (oral)

14. **Nanocrystal-doped polymer spheres as building blocks for Coupled Resonator Optical Waveguides**,
B. M. Möller, N. LeThomas, M. V. Artemyev, R. Wannemacher, U. Woggon
MRS Fall Meeting 2004 (GG 10.28), Boston, 2004

15. **Nanoengineering of CdSe Nanorods in Spherical Microcavities**,
B. Möller, M. V. Artemyev, R. Wannemacher, and U. Woggon,
11. Int. Conf. on II-VI Compounds (NC 4.3), Niagara Falls, 2003 (oral)

16. **CdSe Nanorods and Nanodots in Various Structures**,
M. Artemyev, B. Möller, U. Woggon, and G. Khomutov,
MRS Meeting 2003 (N 1.9), Boston 2003 (oral)

17. **CdSe Nanodots and Nanorods in Photonic Dots**,
B. Möller, M. V. Artemyev, V. Anikeyev, U. Woggon, and R. Wannemacher
Quantum Dot Conference QD 2002 (I 2), Tokyo, 2002 (oral)

18. **Dot-in-a-dot: Electronic and Photonic Confinement in Three Dimensions**,
B. Möller, M. V. Artemyev, W. Langbein, C. Ell, U. Woggon, and R. Wannemacher,
ICPS 2002, Edinburgh, 2002

19. **Photons Confined in 3D Microcavities Doped With Quantum Dots**,
U. Woggon, M. V. Artemyev, B. Möller, W. Langbein, and R. Wannemacher,
MRS Meeting 2002 (E 7.2), Boston, 2002 (oral)

Contributions to Spring Meetings of the German Physical Society (DPG)

20. **Coupled Resonator Optical Waveguides (CROWs) Doped With Quantum Dots**,
B. M. Möller, M. V. Artemyev, R. Wannemacher, U. Woggon
Spring Meeting of the German Physical Society 2005 (HL 49.3), Berlin, 2005 (oral)

21. **Formation of Photonic Molecules in Ensembles of Spherical Microcavities**,
B. M. Möller, M. V. Artemyev, R. Wannemacher, and U. Woggon,
Spring Meeting of the German Physical Society 2004 (HL 15.6), Regensburg, 2004 (oral)

22. **Nanodots und Nanorods in sphärischen Mirkoresonatoren**,
B. M. Möller, M. V. Artemyev, R. Wannemacher, W. Langbein, and U. Woggon,
Spring Meeting of the German Physical Society 2003 (Q 53.8), Hannover, 2003 (oral)

23. **Photolumineszenzexperimente an Halbleiterquantenpunkten in sphärischen Mikroresonatoren**,
B. Möller, M. V. Artemyev und U. Woggon,
Spring Meeting of the German Physical Society 2002 (HL 20.4), Regensburg, 2002 (oral)

Contents

Contents

1. Introduction

> *Waves always behave in a similar way, whether they are longitudinal or transverse, elastic or electric. Scientists of the last century always kept this idea in mind [...]*
> *The invention of linear accelerators lead to the discussion of a variety of structures yielding a low velocity of propagation for electromagnetic waves. Most of these structures are periodical...*
>
> Léon Brillouin, 1946 (taken from ref. [Bri53])

Spherical microcavities doped with semiconductor nanocrystals represent an artificial compound system, that attracted significant research interest in recent years, both in the fields of fundamental and applied physics: Microcavities, confining light to a quasi zero-dimensional region in space, exhibit discrete energy eigenstates and can concentrate enormous field strengths inside the cavity. This can therefore enormously enhance light-matter interaction phenomena, such as low-threshold microlasers [Cha96] and weak and strong coupling of photonic resonances with electronic resonances [Ush99, Buc03].

At first, atoms and dye molecules have been used as an active material in cavities, later, research extended to artificial systems like semiconductor quantum dots, [Gér01, Gay01, Wog03,] which exhibit increased photostability. Semiconductor quantum dots, constituted by nanometer-sized islands of semiconductor material, drastically modify the properties of bound electron-hole-complexes, the excitons: The wave functions of excitons are confined in a three-dimensional nanocavity on a size scale comparable to the excitonic Bohr radius and let the energy dependence of the density of states collapse into delta-like distributions. Since the confinement of excitons in semiconductor nanocrystals (or quantum dots, QDs) depends on the quantum dot radius, the excitonic emission can be tuned easily from the ultraviolet to the far-infrared spectral range simply by varying the quantum dot size during the synthesis at will.

However, for any approach in the field of light-matter interaction, the incoupling of light into the individual resonators is a critical issue. A possibility of engineering the transition dipole moment in quantum dots relative to the photonic modes is highly desired. One successful approach will be covered in this thesis.

Furthermore, attention is paid to photonic microcavities not only with respect to coupling these with active emitters, but also to coupling cavities with each other, especially in the field of optical computation:

1 Introduction

This interest is inspired by replacing conventional electronic circuits by photonic circuits, thereby reducing cross-talk between different circuits. However, for any real-life signal processing, information has frequently to be stored meanwhile, which is currently realized by converting optical signals into electrical signals, which are read out later. This limits the potential of circuits at high data rates. To overcome these limitations, activities were growing to realize slow wave structures, thus replacing information storage by a *delayed* transmission of photonic signals.

An impressive slowing down of light down to 17 m/s was demonstrated in 1999 by Hau *et al.* [Hau99], who used the effect of electromagnetically induced transparency (EIT) in a sodium gas, cooled down to nanokelvin temperatures. The sodium atoms exhibit two electronic ground states and one common excitation level. Here, the interference of a control and a signal laser tuned to the transition energies to the common excited state leads to a quantum interference of the two excitation paths and absorbtion can be significantly suppressed for the signal beam. The opened tiny transmission window is accomplished with a strong variation of the refractive index, leading to a huge group velocity dispersion. Using population oscillations in an EIT-like fashion, these approaches are recently continued to room temperature in a solid state system. Recently, impressive approaches towards using coherent phenomena involving excitonic transitions [Pal05, Frö05] have been reported, e.g., to modify excitation densities for the achievement of Bose-Einstein condensation. In the frame of optical storage, the parameter space is still quite limited in these systems, since these effects rely on the presence of a suitable transition frequency in a concrete realization. Moreover, the application as optical buffers would require a high fractional delay of light propagation normalized to the applied pulse widths. Recent reviews [Mat05, Khu05] suggest, that for coherent atomic media fundamental restrictions for the realization of high fractional delays occur.

In 2004, *R. W. Boyd* pointed out, that EIT-like effects can be modeled by a wave-optical analogue: Here, two optical microresonators with degenerate resonances are discretely attached to a waveguide [Hee02], so that light is subsequently transferred from resonator to resonator with substantial delay. In another approach [Smi04a], the waveguide is coupled to a pair of ring resonators in which the loss rates of the individual resonators have to differ by orders of magnitude. In the waveguide, a small transmission window at the single-resonator frequency is opened, at which no light from the waveguide is trapped in the coupled-resonator system. Here again, the transmission window involves a dramatic group velocity dispersion.

A different concept concerning slow wave structures built-up of almost equally designed coupled resonators has been proposed independently by Stefanou *et al.* in 1998 [Ste98] and *Amnon Yariv et al.* in 1999 [Yar99]: In their theoretical approach, a waveguide model is introduced, which consists of a line of coupled resonators itself. The optical fields of the microcavities are mainly localized in the respective resonator and weakly coupled to the fields of their next neighbors. The electromagnetic eigenstates of the entire coupled-resonator optical waveguide (CROW) are modeled in strong analogy to electronic

states in crystalline solids by a Bloch function, treating the single resonators as weakly coupled photonic atoms. This can be regarded as a tight-binding approach to periodically modulated dielectrics, opposed to the nearly free-photon approach in photonic bandgap materials.

However, the current state-of-the-art in realizing CROW structures mainly covers theoretical investigations [Hee04], and practical realizations using fairly large microcavities ranging in sizes of about a tenth millimeter [Pal03b] and explorations of photonic crystal defects [Alt05a]. A realization in the visible spectral range using cavities with circular cross section has been less explored. Therefore, this thesis aims to demonstrate several key features of CROW structures using polymeric microspheres with radii of a few optical wavelengths*.

This thesis is organized as follows:

Chapter 2 gives an overview about the basic underlying physical properties of the samples used. I will briefly review the mode structure of single spherical photonic dots, comment on wave propagation in materials with a periodically modulated refractive index and explain how CROWs fit into the classification of photonic materials. I will also give a brief overview of the electronic processes in semiconductor nanocrystals, which are used to efficiently illuminate the single and coupled cavity systems. At the end of chapter 2, we discuss the feasibility of elongated CdSe nanocrystals as ideal dipole emitters, e.g. the strong polarization of emitted photons. Therefore, the linearly polarized emission of CdSe nanorods will be discussed with respect to their use for cavity mode control.

In chapter 3, we will examine the incoupling of spontaneously emitted nanocrystal photons into specific cavity modes. Here, we make use of polarized emitting elongated nanocrystals, which by alignment on the microspheres will efficiently emit into the desired TE mode polarization. The experimental results will be compared with theoretical calculations and demonstrate the realization of a three-color TE emitter at room temperature.

Chapter 4 will explore the signatures of coherent coupling of individual cavity light fields. We investigate the different spectral and spatial overlap conditions of closely arranged microspheres. Their impact on the mode volume and the resonator quality (Q) will be discussed. The coherent multisphere coupling is measured applying spatially and spectrally resolved photoluminescence spectroscopy combined with polarization-sensitive mode mapping. The mode structures of different one- and two-dimensional arrangements will be compared.

Chapter 5 will explore the feasibility of the realization of a coupled-resonator optical waveguide. Here we examine the required key features of a CROW, namely the coherent coupling between the resonator light fields in an extended structure and the existence of

*Let me point out — in the Einstein year—, that whispering gallery mode patterns in spherical cavities designed for the microwave range are currently used for tests of Lorentz-invariance. Additionally, a proposal for the detection of gravitational waves relies on the realization of a two sphere cavity, where the individual resonators are coupled by a short waveguide.

multisphere photon states that couple more than simply two spheres at a time. As an experimental method, I introduce measurements on a multisphere "hockey stick" geometry. The successful CROW realization in a bent structure is explored.

In chapter 6, I propose a simplified model of coupled-resonator optical waveguide structures. The model is based on the similarities of the CROW formalism with the description of chains of coupled harmonic oscillators. With this model at hand, an extension of the formalism towards finite structures is presented. The modes confined in a finite CROW display alternating oscillator strengths along the coupled-resonator structure, which serves as an additional tool for the demonstration of coherent interresonator coupling. Furthermore, due to the broken translational symmetry, an additional class of mode superpositions is explored, which could be utilized for entanglement transfer via single photons in the frame of quantum information processing.

The thesis will end with a summary and an outlook gives suggestions for potential future work.

2. Basic Concepts

2.1 Spherical Microresonators

2.1.1 Photonic Dots

In *photonic dots* the light is trapped in three dimensions comparable to or slightly larger than the photonic wavelength, analogously to the three-dimensional confinement of the excitonic wave functions in semiconductor quantum dots, which originally inspired their name.

Due to the confinement, the density of states in photonic cavity structures is no more a continuous function like in free space. In photonic microstructures, in general, we obtain a strong dependence on the dimensionality of the confinement [Yam00]: In free space, we are faced with the usual quadratic form of the photonic density of states as can be seen in fig. 2.1 a). If in one dimension a confinement condition is imposed, the density of k-vectors available to form photon states is reduced in this dimension, leading to a linear energy dependence of the density of states. When the photon energy rises to values, at which the decreasing wavelength matches the boundary conditions for additional k-vectors in the confinement direction, sudden jumps to higher values of the density of states occur (b). The increase of the photonic density of states in the energy regions between those jumps can be easily understood regarding the density of states in the k-space and taking into account the photonic energy dispersion. In k-space, the number of states associated with a given wave number is proportional to the surface of the volume which is spanned by the allowed wave vectors. This surface is proportional to k^{d-1}, d being the dimensionality of the confinement. Since the photon energy is proportional to the wave number, $dE \propto dk$ also holds, and the density of states in terms (DOS) of energy simply reads

$$\mathrm{DOS}(E) \propto E^{d-1} \ . \tag{2.1}$$

If the photon in a photonic dot is faced with confinement in all three directions, the density of states reduces further to a series of delta-like peaks at discrete resonances or cavity eigenmodes. For quasi zero-dimensional structures, the density of states collapses into a series of delta-like spikes at the respective resonance energies. We will see later, that this dependence exactly resembles that of the excitonic states in a semiconductor quantum dot (see sect. 2.3.3). Because of the discrete nature of these cavity eigenmodes, photonic dots are regarded as photonic atoms with a specific level structure. Therefore, a similar terminology may be applied, i.e. as to optical selection rules for the excitation

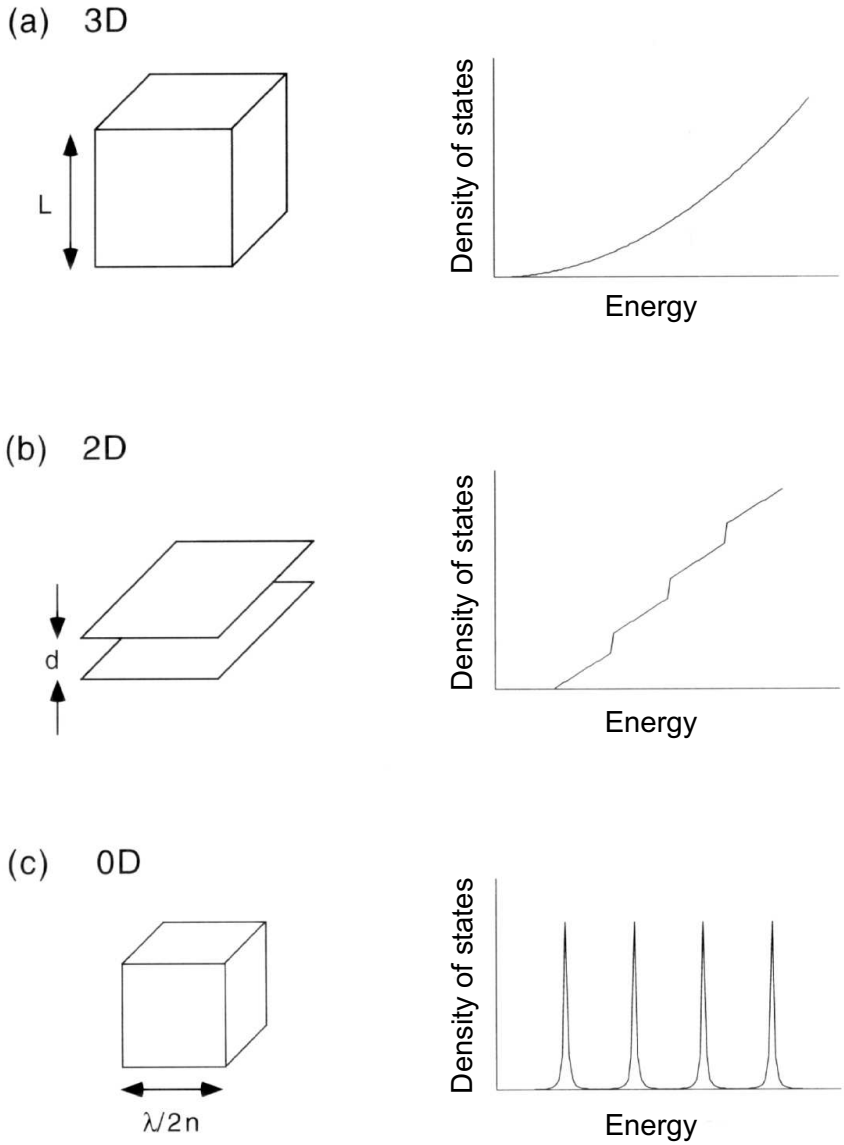

Figure 2.1: Photonic density of states in dependence on energy for different dimensionalities. The exponent expression is given by eq. (2.1), taken from ref. [Yam00].

of photonic modes via nanostructures (see chapter 3) or the coupling of photonic atoms to photonic molecules (as described in chapter 4).

In the following, we will review the mode structure of the light field in spherical photonic dots. The size regime of the microresonators used throughout this thesis, is determined by two important properties: First, the sphere size has to be large enough to guarantee an efficient confinement of light inside our microspheres and thus to lead to delta-like mode densities. This requires dielectric microspheres to be larger than the optical wavelength. Second, the spheres have also to be small enough to provide a non-vanishing leakage of light to the outside world. This latter requirement is essential for two different coupling mechanisms: For the tuning of the coupling with dopants brought onto the surface (see chapter 3) and to achieve an efficient coupling of the spherical light field with that of

neighboring spheres (see section 4 to 6). Thus, the desired microspheres range in sizes of a few micrometers for optical frequencies, for which neither the limits of geometric optics (suitable for large spheres, see, e.g., [Zho03, Rol00]), nor Rayleigh-scattering apply.

The treatment of light scattering by dielectric micron-sized spheres has originally been carried out independently by Debye and Mie in 1908/9 [Deb09, Mie08], and is commonly referred to as *Lorenz-Mie Theory*. The ansatz used is the scattering of a plane wave of light shining on a dielectric sphere placed in a homogenous medium with a lower refractive index, e.g. vacuum. The solution of this problem is governed by Maxwell's equations, which read for the case of absent sources:

$$\begin{array}{ll} \nabla \cdot \mathbf{E} = 0 & \nabla \cdot \mathbf{H} = 0 \\ \nabla \times \mathbf{E} = \mu_0 \mu_r \dot{\mathbf{H}} & \nabla \times \mathbf{B} = -\epsilon_0 \epsilon_r \dot{\mathbf{E}} \ , \end{array} \tag{2.2}$$

and the imposed boundary conditions, which require the matching of the tangential components of the internal and external fields separately for both fields $\mathbf{E}$ and $\mathbf{H}$ at the sphere surface.

After separation of the harmonic time variation for the fields, Maxwell's equations result in the vector wave equations

$$\nabla^2 \mathbf{E} + \omega^2 \epsilon_0 \epsilon_r \mu_0 \mu_r \mathbf{E} = 0 \text{ and } \nabla^2 \mathbf{H} + \omega^2 \epsilon_0 \epsilon_r \mu_0 \mu_r \mathbf{H} = 0 \ . \tag{2.3}$$

Following the derivation of Bohren and Huffman [Boh96], these can be simplified by expressing the vector solution in dependence on a scalar function in spherical coordinates

$$\mathbf{M} = \nabla \times (\mathbf{r} \cdot \psi) \tag{2.4}$$

$$\mathbf{N} = \frac{1}{k} \nabla \times \mathbf{M} \ , \tag{2.5}$$

where $\mathbf{r}$ denotes the spatial position measured from the sphere origin. Thereby, $\mathbf{M}$ and $\mathbf{N}$ are solutions if the scalar function $\psi(r, \theta, \phi)$ solves the scalar wave equation

$$\nabla^2 \psi + \omega^2 \epsilon_0 \epsilon_r \mu_0 \mu_r \psi = 0 \ . \tag{2.6}$$

A separation ansatz in spherical coordinates for $\psi(r, \theta, \phi)$ leads to solutions built from products involving trigonometric functions for ϕ, associated Legendre-functions P_n^m for θ, spherical Bessel functions $j_n(x)$ of the first kind for the argument r in internal fields and Hankel functions $z_n(x)$ for outgoing fields. The new parameters m and n follow as separation constants from the separation ansatz and represent the node numbers along the sphere circumference. With the following abbreviations

$$\pi_n^m = \frac{P_n^m}{\sin\theta}, \qquad \tau_n^m = \frac{dP_n^m}{d\theta} \tag{2.7}$$

the solutions $\mathbf{N}$ and $\mathbf{M}$ can be written using unit vectors in spherical coordinates $\hat{\mathbf{e}}_\phi$, $\hat{\mathbf{e}}_\theta$ and $\hat{\mathbf{e}}_r$,

$$\begin{aligned} \mathbf{M}_{\left\{ {}^{o}_{e} \right\} 1n} \ = \ & \left\{ \begin{array}{c} \cos\phi \\ -\sin\phi \end{array} \right\} \pi_n(\cos\theta) z_n(\rho) \hat{\mathbf{e}}_\theta \\ & - \left\{ \begin{array}{c} \sin\phi \\ \cos\phi \end{array} \right\} \tau_n(\cos\theta) z_n(\rho) \hat{\mathbf{e}}_\phi \ , \text{ and} \end{aligned} \tag{2.8}$$

$$\begin{aligned}\mathbf{N}_{\left\{\begin{smallmatrix}o\\e\end{smallmatrix}\right\}1n} &= \left\{\begin{array}{c}\sin\phi\\ \cos\phi\end{array}\right\} n(n+1)\sin\theta\pi_n(\cos\theta)\frac{z_n(\rho)}{\rho}\hat{\mathbf{e}}_{\mathbf{r}} \\ &- \left\{\begin{array}{c}\sin\phi\\ \cos\phi\end{array}\right\} \tau_n(\cos\theta)\frac{[\rho z_n(\rho)]'}{\rho}\hat{\mathbf{e}}_\theta \\ &+ \left\{\begin{array}{c}\cos\phi\\ -\sin\phi\end{array}\right\} \pi_n(\cos\theta)\frac{[\rho z_n(\rho)]'}{\rho}\hat{\mathbf{e}}_\phi \ .\end{aligned} \tag{2.9}$$

The subscripts above, e and o, indicate even and odd functions with respect to the trigonometric functions involving ϕ. Here, for the case of a plane wave excitation, the separation constant m leads to non-vanishing contributions for the quantum number $m = 1$ only. With the above solutions, the Fields $\mathbf{E}$ and $\mathbf{H}$ can be constructed as series expansions in the fields $\mathbf{M}$ and $\mathbf{N}$, in which the respective expansion coefficients have to be evaluated according to the boundary conditions. The respective expressions for the fields are then given by the following superposition

$$\begin{aligned}\mathbf{E}_{\text{Sca}} &= \textstyle\sum_{n=1}^{\infty} = i^n E_0 \frac{2n+1}{n(n+1)}(ia_n\mathbf{N}_{e1n} - b_n\mathbf{M}_{o1n}) \ , \\ \mathbf{H}_{\text{Sca}} &= \frac{k}{\omega\mu}\textstyle\sum_{n=1}^{\infty} i^n E_0 \frac{2n+1}{n(n+1)}(ib_n\mathbf{N}_{o1n} + a_n\mathbf{M}_{e1n}) \ .\end{aligned} \tag{2.10}$$

For the expansion coefficients we get

$$a_n = \frac{m\psi_n(mx)\psi_n'(x) - \psi_n(x)\psi'(mx)}{m\psi_n(mx)\xi_n'(x) - \xi_n(x)\psi_n'(mx)} \tag{2.11}$$

$$b_n = \frac{\psi_n(mx)\psi_n'(x) - m\psi_n(x)\psi_n'(mx)}{\psi_n(mx)\xi_n'(x) - m\xi_n(x)\psi_n'(mx)} \ , \tag{2.12}$$

with the Riccati-Bessel function

$$\Psi_n(x) = xj_n(x), \text{ and } \chi_n(x) = x(j_n(x) + iy_n(x)) \ , \tag{2.13}$$

where $j_n(x)$ and $y_n(x)$ are the spherical Bessel functions of the fist and second kind, respectively. Here, the dimensionless quantity $x = \frac{2\pi na}{\lambda}$ is commonly referred to as the size parameter and the new parameter m here represents the ratio of the refractive indices of the dielectric sphere and the surrounding medium. From the equations above, we readily notice, that microcavity fields dominated by the coefficients b_n lead to electric field vectors with no radial component. Similarly, dominant b_n coefficients result in cavity fields without any radial component in the magnetic field vectors. Therefore, these fields can be divided into transverse electric modes exhibiting electric fields always *tangentially* oriented with respect to the sphere surface and transverse magnetic modes with the same behavior for the magnetic field. We already point out here, that this classification by the transverse field character also holds for a quantum electrodynamical treatment, since the directionality of the field vectors is fully preserved in the quantization calculus. We will meet this classification again, when we will deal with anisotropic emitters in section 3. As an example of the light localization in dielectric microspheres, a field distribution will be discussed in chapter 3, where we will treat the resonator mode excitation via anisotropic nanoemitters. The confinement in the radial dimension can be understood

by the separated equations for the radial field component. This equation, as discussed in ref. [Chi96], has a formal similarity with the Schrödinger equation in the presence of a potential. The solution of this equation can be interpreted as standing waves in the potential well formed by the spherically shaped dielectric. However, this analogy is not fully accurate, e.g., the potential is energy dependent.

For the internal field, similar expressions like (2.11) and (2.12) hold true. Since the denominators of the expansion coefficients for the internal field turn out to be exactly equal to those of the scattered field, we can determine the spherical resonance positions via calculating the resonance features apparent in the scattered field: One mode dominating the internal field of the sphere leads to the same set of quantum numbers for the corresponding mode dominating the scattered field outside the sphere. In order to evaluate the resonance conditions, it is useful to display the *scattering efficiency*, i.e. the fraction of energy scattered by the sphere normalized to the energy illuminated on the geometrical sphere cross section. This can be expressed via the expansion coefficients a_n and b_n as the scattering efficiency Q_{Sca}:

$$Q_{\text{Sca}} = \frac{2}{(kR^2)} \sum_{n=1}^{\infty} (2n+1) \left(|a_n|^2 + |b_n|^2 \right) \ . \tag{2.14}$$

We note from the equation above, that the scattering efficiency is composed as a sum over all mode orders. Since the resonance positions remain essentially unaffected by different excitation conditions, e.g. light emitted by embedded nanocrystals in a microsphere, we can make use of equation (2.14) for the determination of the mode orders and polarization character. For the comparison with experimental spectra, we evaluate (2.14) in dependence on the wavelength, which is contained in the size parameter dependence of the expansion coefficients a_n and b_n. Since the size parameter is a quantity proportional to the fraction of the sphere radius and the light wave length, the modification of the spectra due to size variation of the microspheres can be easily predicted: If we regard a certain size parameter for a given resonance to be fixed, then an increase of the microsphere radius is accompanied with a larger light wavelength. Thus, for larger microspheres, resonances with a given set of quantum numbers shift to the red spectral range. Additional resonances appear, when the size of the microsphere is large enough, so that higher angular quantum numbers dominate with significant contributions in eqs. (2.11) and (2.12). Similar conditions hold for changes of the refractive index, which enlarges the optical path length inside the cavity, so that their effects are similar to those of an increase of the microsphere radius. The overview over the spectral modifications is given in fig. 2.2, where the scattering efficiency is evaluated using a modified routine after [Boh98] for varying microsphere radii from 1.2 μm to 1.6 μm. The spectral sensitivity of the resonances to size modifications on the nanometer scale is given in the inset of fig. 2.2, where the microsphere radius has been varied in steps of 1 nm only. The resonances accordingly respond with a shift of 1.6 nm.

A somewhat simplified picture of the resonance shifts with the resonator size is available considering the geometrical ray optics picture, which is commonly applied for an accessible

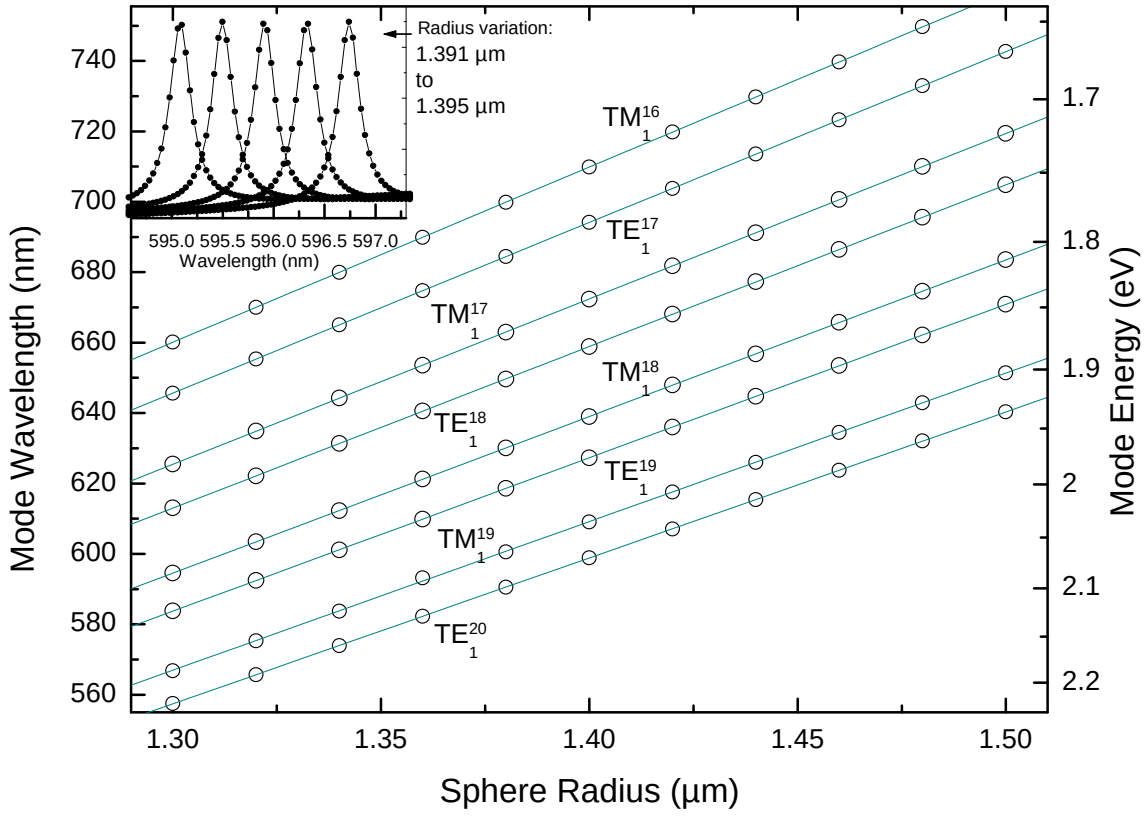

Figure 2.2: Size dependence of cavity resonances in dielectric microspheres. The sphere radius has been varied from 1.3 μm to 1.5 μm. For the refractive index, the dispersion of polystyrene has been taken into account for the spectrum evaluation. The inset shows the sensitivity of the cavity resonances to radius variations in the nanometer scale from 1.391 μm to 1.395 μm.

explanation of the rainbow, trapping mechanisms in optical tweezers and alike. Here, a resonance is formed by straight optical rays continuously falling onto the resonator rim in a small angle. Subsequent total internal reflection leads to a closed ray path, giving the resonance pattern [Lab99]. Thus, a regular polygon is inscribed into the resonator and the resonance condition for the highest order whispering gallery modes is fulfilled for wavelengths exactly matching the polygon sizes. This approximation for the N-th resonance can be written as

$$N \cdot \frac{\lambda}{n_{\mathrm{ref}}} = 2\pi R \text{ , or } N = \frac{2\pi R n_{\mathrm{ref}}}{\lambda} \text{ ,} \tag{2.15}$$

which makes the occurrence of the dimensionless size parameter in the equations (2.11) and (2.12) above more transparent. A schematic representation of this ray optical approach is given in fig. 2.3. This mode scaling behavior represents a general characteristic of microresonators, even with a more complicated shape, see e.g. ref. [Nob04] for the mode scaling in hexagonally shaped microcavities. Since the length of the optical ray path can be modified via refractive index changes of the cavity material as well, ansatzes have been developed to tune cavity resonances by postprocessing treatments of the cavities [Poo04a] and slight deformations [vK01]. The sensitivity of the cavity resonances to the

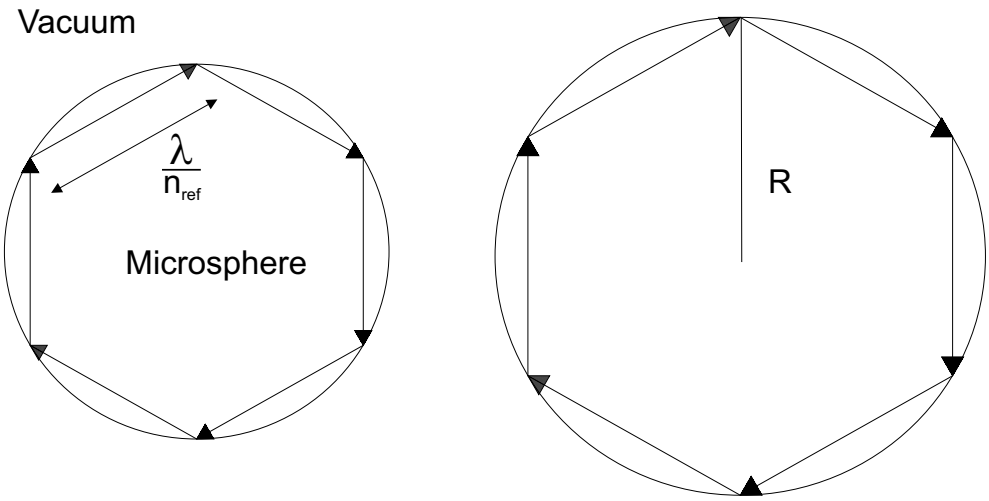

Figure 2.3: The size sensitivity of microsphere modes is transparently predicted in the ray optics model.

optical properties of the environment, like the refractive index, etc. leads to the proposal of microspheres as sensors [Arn03]. Due to its spectral accuracy, scattering calculations using Mie theory allow for a precise determination of diameters of dielectric spheres or thin fibers down to the nanometer scale, see e.g. [War04].

To efficiently engineer the excitation of the cavity field using semiconductor nanocrystals, we have to optimize the orientation of the transition dipole moment of the semiconductor nanocrystals with respect to the cavity field. As we already mentioned, the treatment, which in general has to be worked out including the interplay of quantum mechanics with quantum electrodynamics, does not impose further difficulties concerning the cavity field. To make this more evident, let us have a brief look at the quantization procedure for microspheres. The discussion of mode quantization follows refs. [Chi87b] and [Chi87a]: Here the dielectric sphere is placed into an imaginary conducting sphere which is considered to be way larger than the microsphere. The fields $\mathbf{E}(r,t)$ and $\mathbf{B}(r,t)$ can be generally written in the form

$$\begin{aligned} \mathbf{E} &= \textstyle\sum_s \frac{1}{\omega_s}\frac{d\alpha}{dt}\mathbf{e}(s,r) \\ \mathbf{B} &= \textstyle\sum_s \alpha(s,t)\mathbf{b}(s,t)\ , \end{aligned} \tag{2.16}$$

with the multi-index s containing the mode quantum numbers $l, m, n, \left\{ {e \atop o} \right\}$. Both fields then have to satisfy the macroscopic Maxwell's equations and the additional condition of a vanishing tangential component of the **E**-field at the boundary of the large quantization sphere. The solutions of this geometry for scattered fields, internal fields, etc. coincide with the solutions of Maxwell's equations discussed in (2.10), the remaining modification due to the quantization volume is a limitation of the allowed frequencies, which satisfy the boundary conditions for the quantization sphere. The functions $\alpha(s,t)$ have to guarantee in accordance with Maxwell's equations

$$\frac{d^2\alpha(s,t)}{dt^2} = -\omega_s^2\alpha(s,t)\ . \tag{2.17}$$

This equation of motion (2.17) can be deduced from an effective Lagrangian

$$L = \sum_s \frac{1}{2} \left\{ \frac{1}{\omega_s^2} \left[\frac{d}{dt} \alpha \right]^2 - \alpha(s,t)^2 \right\} \tag{2.18}$$

with the canonical momenta

$$\pi(s,t) = \frac{\partial L}{\partial \dot{\alpha}(s,t)} \ . \tag{2.19}$$

Therefore, one can readily construct creation and annihilation operators $a^\dagger$ and a_s for the mode s:

$$\begin{aligned} a_s^\dagger(t) &= \frac{1}{\sqrt{2}} \left[\alpha(s,t) - i\omega_s \pi(s,t) \right] \\ a_s(t) &= \frac{1}{\sqrt{2}} \left[\alpha(s,t) + i\omega_s \pi(s,t) \right] \ . \end{aligned} \tag{2.20}$$

With the operators above, the field operators read

$$\begin{aligned} \mathbf{E}(\mathbf{r}) &= -\frac{i}{\sqrt{2}} \textstyle\sum_s \left[a_s(0) - a_s^\dagger(0) \right] \mathbf{e}(s,\mathbf{r}) \text{ and} \\ \mathbf{B}(\mathbf{r}) &= \frac{1}{\sqrt{2}} \textstyle\sum_s \left[a_s(0) - a_s^\dagger(0) \right] \mathbf{b}(s,\mathbf{r}) \ . \end{aligned} \tag{2.21}$$

As we see from the previous expressions, we might leave the usual formalism for light-matter-interactions unchanged, whereas the orientation of the fields are solely contained in the expressions obtained from Maxwell's equations. Thus, in the light-matter interaction term, the directionality of the dipole moment of the nanocrystals attached to the microspheres remains to be engineered:

$$H_{\text{int}} = -f \mathbf{p} \cdot \mathbf{E}(\mathbf{r}) \ , \tag{2.22}$$

for which we give an example in chapter 3.

2.2 Periodic Structures — Photonic Crystals

As mentioned in the introduction, the largest part of this thesis will deal with periodic arrangements of photonic atoms to coupled-resonator optical waveguide geometries. This concept shares some similarities with the well established concept of photonic crystals, pioneered by Yablonovitch and John in 1987 [Yab87, Joh87], which consist of a periodic dielectric structure as well. For example, colloidal photonic crystals can be built from submicrometer sized spheres, made from optically transparent polymers, which are sedimented from a solution. However, the size variation of the refractive index inside the structured dielectric medium exhibits in both structures a different characteristic scale compared to the wavelength of the guided light. In a photonic crystal, the index modulation is in the size range of approximately one half of the light wavelength. Thus, in a single photonic crystal constituent, the confinement is comparatively low. Due to this low confinement, waveguiding in a photonic crystal can be described via a nearly free photon approach analogous to the nearly free electron approach in solid state physics.

In a coupled-resonator optical waveguide, as will be discussed in the following sections, a comparatively weak optical coupling between the constituents is desired, which can be directly translated into a larger light confinement in a single waveguide unit and — in the case of dielectric microspheres — leads to the choice of microspheres ranging in size of several micrometer for the visible spectrum. Due to this fact, a coupled-resonator optical waveguide and a photonic crystal can be regarded as two complementary concepts, in which photonic crystals display a weak modulation of an optical wave [Cas96], whereas the coupled-resonator optical waveguide constitutes the tight-binding limit in a photonic description [Yar99].

2.3 Semiconductor Nanocrystals

In this section, a short review of the properties of the light emitting species probing the photonic states, i.e. semiconductor nanocrystals, will follow. This section will not only cover the respective features of the quantum confined nanocrystal material in an isolated fashion, but also already focus on the underlying features of the highly crystalline material, which in turn obeys a nearly perfect periodic structure for the electron propagation. As we will demonstrate in section 4.1, where we investigate the photon states in photonic structures, many analogies like *Bloch waves* and *band structure formalism* may be adopted from solid state physics for ready use. Doing as such, we are acting on safe ground and are prepared for the subsequently discussed photonic experiments.

2.3.1 Semiconductors

The most striking feature in crystals is the formation of electronic bands due to the periodic potential experienced by electrons in the vicinity of highly ordered lattices. This periodicity gives rise to the formation of electronic bandstructures. The energetic difference between the resulting valence band and the conduction band leads to the classification of metals, semiconductors and insulators. For noninteracting carriers, an ansatz is given by an Hamiltonian for a single electron in a periodic lattice, the so-called *single electron picture* [Ash76]

$$H\Psi(\mathbf{r}) = \left(\frac{\hbar^2}{2m}\nabla^2 + V_{\text{lattice}}(\mathbf{r})\right)\Psi(\mathbf{r}) = E\Psi(\mathbf{r}) \ , \tag{2.23}$$

with a potential V_{lattice}, that obeys the spatial periodicity of the underlying lattice by translation of a lattice vector $\mathbf{R}$

$$V_{\text{lattice}}(\mathbf{r}) = V_{\text{lattice}}(\mathbf{r}+\mathbf{R}) \ . \tag{2.24}$$

According to the Bloch-Floquet theorem, a solution of (2.23) can be generally written as [Kit96]

$$\Psi_{\mathbf{k}}(\mathbf{r}) = u_{\mathbf{k}}e^{ikr} \ , \text{ with } u_{\mathbf{k}}(\mathbf{r}+\mathbf{R})\Psi_{\mathbf{k}+\mathbf{G}}(\mathbf{r}) = \Psi_{\mathbf{k}}(\mathbf{r}) \ , \tag{2.25}$$

where the function $u_{\mathbf{k}}$ describes a lattice periodic function and the exponential term corresponds to an envelope function, which in this case can be assumed to be a free wave with the wave number k. One approach to find a suitable Bloch function for the solution of (2.23) constitutes the *tight-binding model*, in which the Bloch waves can be constructed as a superposition of the electronic wave functions of the single atoms that constitute the lattice. Therefore, it is assumed, that the Hamiltonian for an electron single atom is already solved, leading to a single atom wave function ϕ. Then, from the Hamiltonian (2.23), it follows, that the energy dispersion can be evaluated from

$$E(\mathbf{k}) = \frac{\langle \Psi_{\mathbf{k}} | H | \Psi_{\mathbf{k}} \rangle}{\langle \Psi_{\mathbf{k}} | \Psi_{\mathbf{k}} \rangle} \ . \tag{2.26}$$

It can be shown, that the expression above leads to higher energy eigenvalues for trial values, which do not exactly solve (2.23), while the minimum energy is reached for the exact wave function. This is the basis of the *Rayleigh-Ritz principle*, which in an analogous manner can be applied for photonic states in periodic dielectrics. Let us assume, that a sufficiently good trial function is given as a superposition of the electron wave functions of single atoms ϕ. Then Ψ can be written as

$$\Psi_{\mathbf{k}} = \sum_n e^{i\mathbf{k}\mathbf{R}_n} \cdot \phi_i(\mathbf{r} - \mathbf{R}_n) \ . \tag{2.27}$$

This superposition now fulfills the requirements of a Bloch function defined above and the energy dispersion can be obtained from the Ritz expression. For the simple case of s-type functions in a cubic lattice, the resulting energy dispersion now takes the form

$$E(\mathbf{k}) = E_{\text{single atom}} - A - B\left(\cos(k_x a) + \cos(k_y a) + \cos(k_z a)\right) \ , \tag{2.28}$$

where the parameters A and B, respectively, are given by the matrix elements involving the atomic wave functions at the same or neighboring sites and the correction potential of the crystal potential to the single atom potential. A very similar expression will be obtained for coupled-resonator optical waveguides structures, which will be dealt with in section 4.1. For small wave-vectors, eq. (2.28) can be approximated by the first elements of a Taylor-series, written as:

$$E(\mathbf{k}) \approx E(\mathbf{k} = 0) + \frac{\hbar^2 \mathbf{k}^2}{2m_{\text{eff}}} \ . \tag{2.29}$$

Thus, an electron in a crystal can be approximated as a traveling wave, while the effect of the periodic lattice is solely contained in an effective mass m_{eff}. For small k-values, the dispersion can be approximated by parabolic expressions. The expression (2.28) describes the formation of an electronic band. The characteristic bandstructure of semiconductors is formed by highest fully occupied bands, followed by an initially completely unoccupied band, the conduction band, which are distanced from each other by a few electronvolts, so that excitations between both are possible using electrical or optical means. For optical spectroscopy, especially direct semiconductors are relevant, having the minimum of the

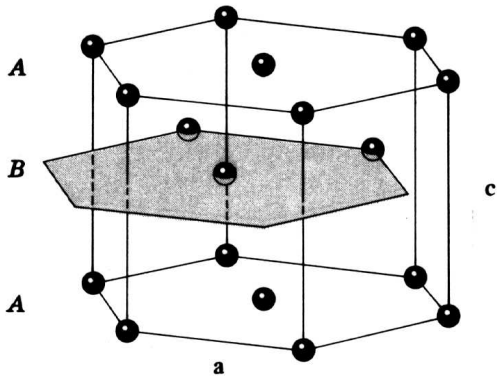

Figure 2.4: Crystal structure of CdSe, taken from ref. [Kit96].

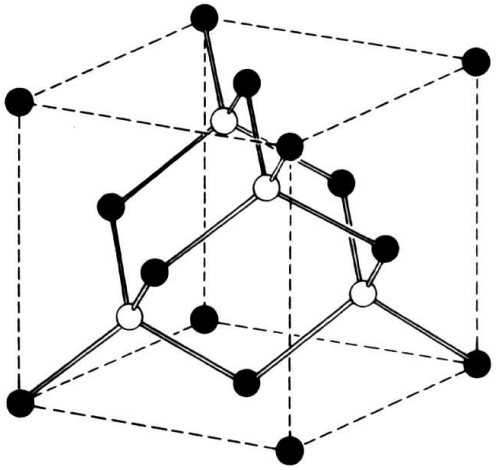

Figure 2.5: Crystal lattice of ZnS, taken from ref. [Kit96].

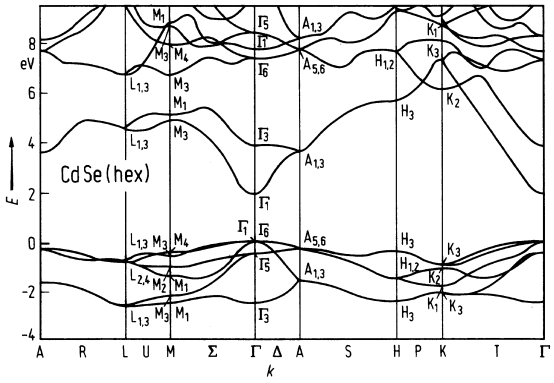

Figure 2.6: Bandstructure of CdSe, calculated with a pseudopotential ansatz, after [LB82].

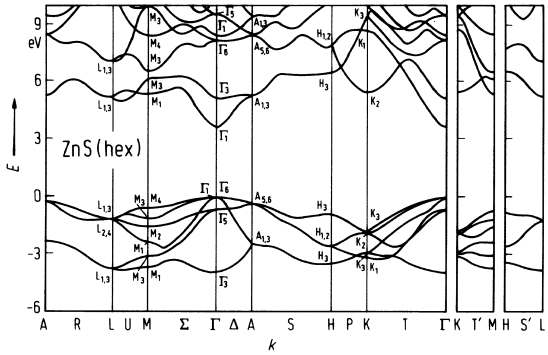

Figure 2.7: Bandstructure of ZnS, calculated with a pseudopotential ansatz, after [LB82].

conduction band and the maximum of the valence band at the same wave vector, so that transitions can efficiently be induced or observed by photon absorption or emission. The nanocrystals used in this thesis consist of the direct semiconductors CdSe and ZnS. Both belong to the class of II-VI compound semiconductors, i.e. they are constituted by two elements of the second and sixth chemical group. Thus, the constituents have metallic and insulator characteristics, respectively. In both semiconductors the atoms are connected via tetrahedron bonds to their neighbors. The crystal structure of CdSe is the wurtzite structure, which can be described by an hexagonally closed-packed anion structure of the selenium ions, in which every second tetrahedron gap is occupied by cadmium ions. The wurtzite lattice is depicted in fig. 2.4 and its Brillouin zone is shown in fig. 2.8. ZnS crystallizes in this case in the zincblende structure. The zincblende structure is constructed as a combination of two face-centered cubic lattices for both elements, which are shifted by a quarter of a cubic diagonal against each other [Kit96]. The zincblende structure is shown in fig. 2.5, and the corresponding Brillouin zone is given in fig. 2.9.

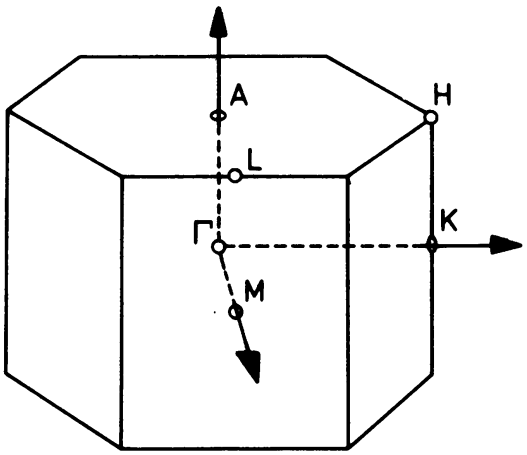

Figure 2.8: First Brillouin zone of the wurtzite lattice,taken from ref. [Iba90].

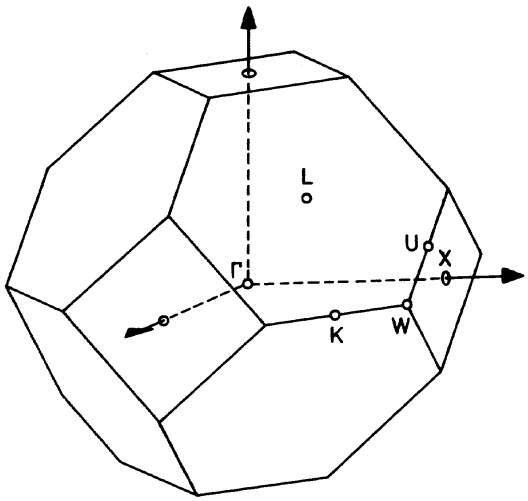

Figure 2.9: First Brillouin zone of the zincblende lattice, taken from ref. [Iba90].

The tetrahedron bonds in both structures stem from hybridized sp^3 orbitals, whose s-contribution originates from the metal ions, cadmium and zinc, respectively, whereas the p-character is contributed by the p orbitals from the insulators sulphur or selenium. The resulting band structures for CdSe and ZnS are given in figs. 2.6 and 2.7. The different curvature of the valence bands at the Γ points leads to the terminology of light and heavy holes for optical excitations. Additionally, the degeneracy at the Γ points is removed by spin-orbit coupling in the case of ZnS and spin-orbit coupling and crystal-field splitting in the case of CdSe.

2.3.2 Excitons

Transition energies in semiconductors are not completely determined by the energy gap between the highest occupied bands. The excitation of an electron from the valence band into the conduction band moreover leads to the creation of a new quasi-particle constituted by the electron itself and the left net positive charge, formed by one unoccupied state in the valence band, the hole. The attractive Coulomb interaction between electron and hole leads to the formation of a bound state, the *exciton*. These bound states can be modeled as two oppositely charged particles with effective masses stemming from the band dispersion and from the Coulomb force, mediated through the crystal with an effective dielectric background constant ϵ [Pey93]

$$\left(-\frac{\hbar^2}{2m_e}\nabla_e^2 - \frac{\hbar^2}{2m_h}\nabla_h^2 - \frac{e^2}{\epsilon\,|\mathbf{r}_e - \mathbf{r}_h|}\right)\Psi = e\Psi \ . \tag{2.30}$$

Analogously to the hydrogen atom, this equation can be solved with a separation ansatz. The resulting energy eigenvalues are given by

$$E_n^{\text{Exciton}} = E_{\text{Gap}} - E_{\text{Ryd}} \cdot \frac{1}{n^2} + \frac{\hbar^2\mathbf{K}^2}{2\,(m_e + m_h)} \ , \tag{2.31}$$

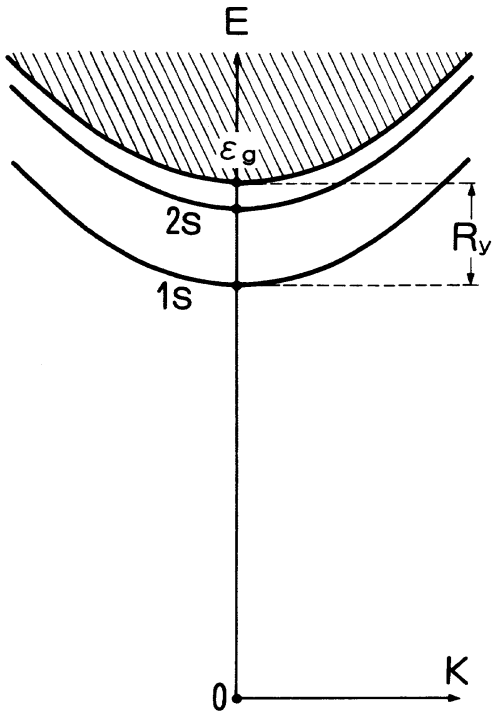

Figure 2.10: Energy levels of excitons in bulk semiconductors. The eigenenergies vary quadratically with the center-of-mass momentum, after [Uet86].

where n labels the n-th energy state, and $E_{\mathrm{Ryd}} = \frac{\hbar^2}{\left(2m_e^{-1}+m_h^{-1}\right)a_{\mathrm{Bohr}}}$ denotes the excitonic Rydberg energy with the excitonic Bohr radius $a_{\mathrm{Bohr}} = \frac{\epsilon\hbar^2}{\left(2m_e^{-1}+m_h^{-1}\right)e^2}$. The energy here is calculated from the top of the valence band. Thus, the excitonic energies are reduced by the Coulomb interaction compared to the bandgap and display a discrete series of energies in addition to their kinetic energy. A scheme of the resulting energy values for excitons is given in fig. 2.10. For CdSe, the excitonic Bohr radius is 5.4 nm and thus one order of magnitude higher than the lattice constant of approximately 0.6 nm, which justifies the neglection of details in the underlying lattice.

2.3.3 Quantum Confinement

The movement of carriers in nanostructured semiconductor material is significantly modified compared to the bulk case, leading to quantum confinement for the carrier wave functions. Analogously to the optical confinement, which we discussed in subsection 2.1.1, quantum confinement leads to a drastic redistribution of the density of states. Similarly, this confinement can be classified by the dimensionality, in which the confinement is applied, leading to quantum wells, quantum wires, and quantum dots [Kli95]. The carriers — electrons, holes, or excitons — can be treated as traveling waves inside the semiconductor. In case of bulk material, the density of states follows the common square root dispersion. If the semiconductor is reduced in one dimension to a size comparable to the de-Broglie wavelength of the carriers, a quantization condition is imposed on the

k-vectors of the corresponding carrier waves. In such a two-dimensional confinement, new states are only available, if the energy crosses a threshold value, at which the small enough de-Broglie wavelength satisfies the quantization condition, leading to a stepwise increase of the density of states. Between these steps, the dispersion of the density of states can be deduced from the density of states in k-space. In a d-dimensional confinement geometry, the number of states is proportional to the surface of the k-volume spanned by the k-vector under consideration. Thus, the number of states dependent on k is proportional to k^{d-1}. Since the energy is proportional to the square of the wave number, the energy interval scales with the wave number interval as $dE = kdk$. Therefore, if we express the energetic density of states (DOS) in dependence on the k-vector, the proportionality follows an exponent reduced by unity as k^{d-2}. This can be expressed in energy terms solely, using again the quadratic dependence of the energy on the k-vector

$$\mathrm{DOS}(E) \propto E^{\frac{d}{2}-1} \ . \tag{2.32}$$

Here, dealing with semiconductors, the energy is set to zero at the top of the bandgap. For a quasi zero-dimensional system, like a quantum dot, quantum confinement occurs in all three dimensions. Thereby, only energy values, that satisfy the quantization condition are allowed. This concentrates the allowed states to discrete energies. In-between, the density of states remains zero, resulting in a delta-like distribution. Thus, the density of states in a zero-dimensional limit of the quantum dot obeys the same function of energy like we obtained in subsection (2.1.1) for the photonic density of states in a photonic dot. This again demonstrates the similarity between both concepts. A schematic plot of the dependence of the density of states on the dimensionality of the confinement can be found in fig. 2.11

2.3.4 Excitons in Nanocrystals

In nanocrystals, the excitonic states are significantly modified compared to the bulk system. The three-dimensional confinement, as discussed in the preceding subsection, leads to the formation of discrete three-dimensional states whose energies depend on the spatial extension of the confinement potential, namely the nanocrystal size. The size dependence of the excitonic states can be understood in comparatively simple terms in the limit of strong confinement: Here, the nanocrystal is large enough, so that the effective mass approximation is still valid, and at the same time small enough, so that the imposed confinement constitutes the dominant energy contribution, whereas the impact of the Coulomb interaction between electron and hole can be neglected. In this picture, the confined exciton model separates into the confinement of two carriers, which can be treated separately in an equivalent manner. Strictly speaking — we ignore the Coulomb interaction in this picture — we are in principle dealing with a confinement of an electron-hole pair, and not with the confinement of an exciton. The nanocrystals dealt with in this thesis are prepared by wet chemical means in solution, leading to an almost perfect spherical shape. Hence, in the strong confinement limit, the spherical confinement potential

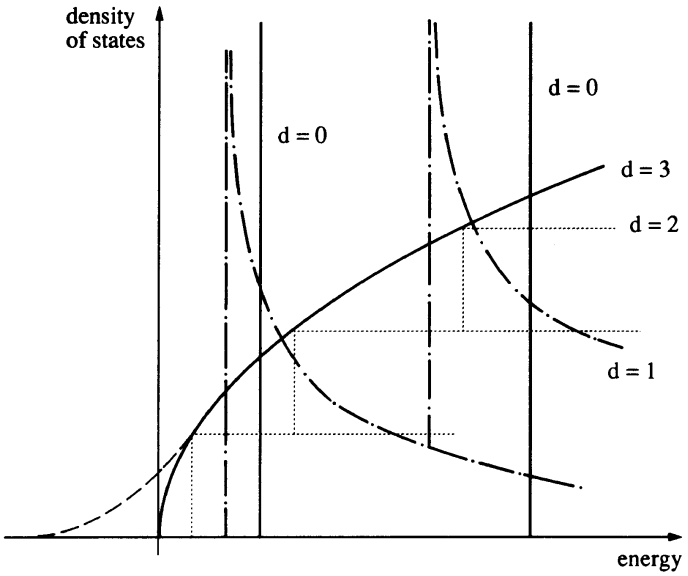

Figure 2.11: Density of states in confinement geometries of different dimensionality, taken from ref. [Kli95]

for the individual charge carriers can be written as spherically symmetric. Additionally, the confinement potential is assumed to be infinite, thus, the charge carriers are ideally confinement in the nanocrystal. The confinement potential for electron and hole $V_{e/h}$ can be written as

$$V_{e/h} = 0 \text{ for } |\mathbf{r}| < R, \text{ and} \tag{2.33}$$

$$V_{e/h} = \infty \text{ for } |\mathbf{r}| \geq R \ , \tag{2.34}$$

where R denotes the nanocrystal radius. The problem can now be represented by the Hamiltonian [Bán93]

$$\left(-\frac{\hbar^2}{2m_e}\nabla_e^2 - \frac{\hbar^2}{2m_h}\nabla_e^2 + V_e(\mathbf{r}_e) + V_h(\mathbf{r}_h)) \right) \Psi(\mathbf{r}_e, \mathbf{r}_h) \ . \tag{2.35}$$

Since the problem ignores the Coulomb-interaction between individual charges and is stated in spherical symmetry, the solution can be obtained by a separation ansatz for the individual wave functions $\Psi(\mathbf{r}_e)$ and $\Psi(\mathbf{r}_h)$. The separation into spherical Bessel functions $j_l(kr)$ for the radial part and spherical harmonics for the angular part expresses the confinement condition — and subsequently the eigenenergy condition — solely through the radial part of the wave function, which must vanish at the nanocrystal boundary $|\mathbf{r}| = R$:

$$j_l(kr) = 0 \equiv j_l(\chi_{n,l}) \ , \tag{2.36}$$

with $\chi_{n,l}$ being the roots of the spherical Bessel function. The allowed k-values are therefore given by the roots of the spherical Bessel function divided by the nanocrystal radius. The resulting eigenenergies of the charge carriers can accordingly be written as

$$E_{e,nlm} = \frac{E_g}{2}\frac{\hbar^2}{2m_e}\left(\frac{\chi_{n,l}}{R}\right)^2 \text{ and} \tag{2.37}$$

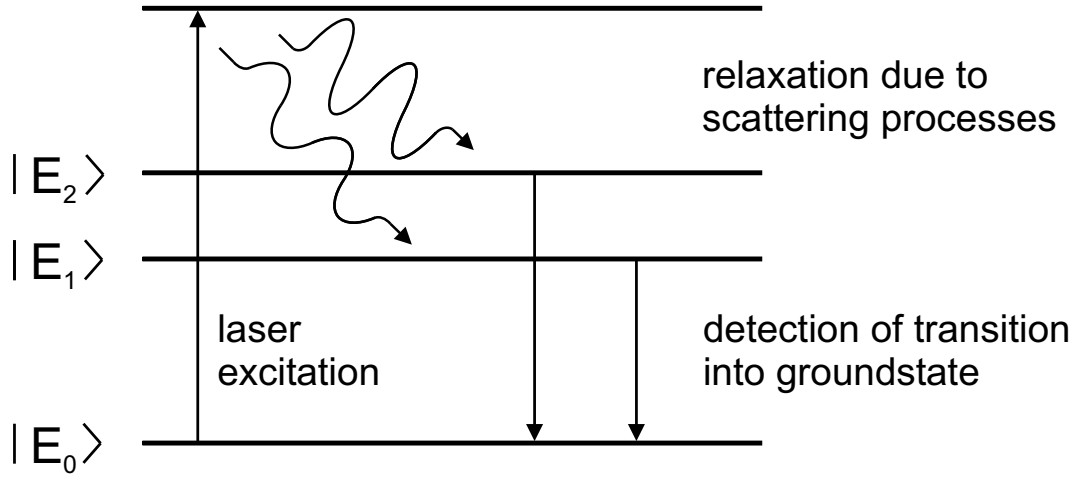

Figure 2.12: Level scheme of nonresonant photoluminescence: A laser excites higher energy states. After phonon assisted relaxation to the excitonic ground state, photons emitted during radiative recombination to the crystal ground state can be detected.

$$E_{h,nlm} = \frac{E_g}{2}\frac{\hbar^2}{2m_h}\left(\frac{\chi_{n,l}}{R}\right)^2 . \tag{2.38}$$

In more realistic calculations, the confinement potential is not considered to be infinite. This can be accounted for by modifications of the confinement conditions by matching the wave function expansion inside and outside the nanocrystal at the semiconductor boundary. Furthermore, the Coulomb-interaction can not be completely ignored [Wog97]. However, the electron-pair energies as treated above, serve as suitable basis states for the expansion of more accurate solutions for the excitonic states. The general trend, however, especially with respect to the confinement induced blue shift, is still preserved. The energy expression above indicates a confinement induced blue shift of the electron-hole pair energy with decreasing nanocrystal size. The excitonic energy can thereby be controlled over a large range, by changing only the geometric scale of the quantum confinement. For the case of CdSe nanocrystals, the energy range from far-infrared to ultraviolet can be covered. The confinement potential can be increased during the chemical synthesis by an additional surface layer of semiconductor material with a larger bandgap, i.e. ZnS, as used for the nanocrystals referred to in this thesis.

2.3.5 Polarization-Sensitive Mode Mapping

In the experiments presented in this thesis, we observe the photoluminescence of semiconductor nanocrystals. In order to distinguish between optical signals stemming from the excitation process and the subsequent emission, we deal with nonresonant photoluminescence throughout this thesis. Here, the excitation is performed optically by an Argon-Ion laser emitting at 488 nm, which is focussed onto the sample. The photon energy is absorbed by the semiconductor quantum dots by creating electron-hole pairs in energetically higher excitonic states. These excitonic states are subject to phonon scattering and can relax to lower energetic exciton states. The electron-hole pair now recombines radiatively

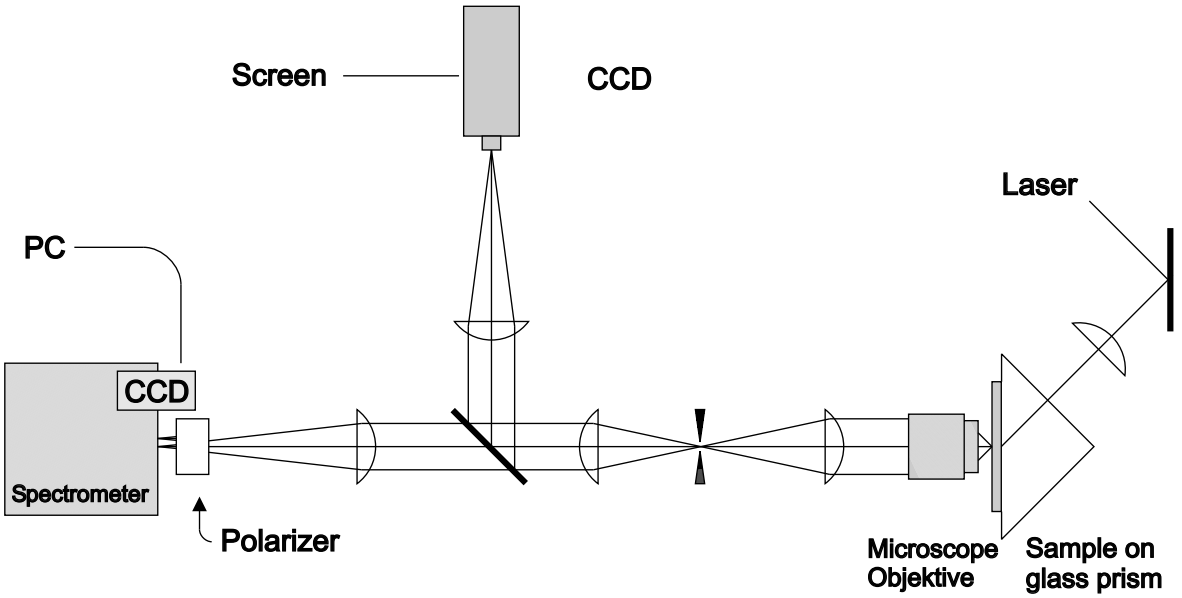

Figure 2.13: Microphotoluminescence setup: The sample is mounted on the front face of a glass prism. The excitation of the sample is provided by frustrated total internal reflection. A microscope objective collects the nonresonant emission from the sample.

and the emitted photons can be detected directly or coupled into photonic dots as a probe of its photonic levels and detected subsequently. The principle of nonresonant photoluminescence is depicted in fig. 2.12. In order to guarantee an efficient excitation of the sample, it is adhesively mounted onto the hypotenuse facet of a quartz prism and illuminated through one of the back facets. This geometry allows an efficient incoupling of light into microsphere modes as has been discussed, e.g., in ref. [Gor99]. The exciting laser light is focussed onto the front facet and coupled into the sample through frustrated total internal reflection inside the prism. A homogeneous excitation for large regions, e.g. in the case of spatially resolved spectroscopy on coupled microresonators is achieved using a spot-size of several tens of microns. The emitted photoluminescence light is collected by a piezo controlled microscope objective with a numerical aperture of 0.9 NA. According to the Rayleigh-criterion, we can acquire a spatial resolution of

$$\Delta x = 0.61 \cdot \frac{\lambda}{\mathrm{NA}} \ , \tag{2.39}$$

which for emission wavelengths around 580 nm results in a resolution limit of about 0.4 μm.

A subsequent lens images the sample onto a virtual image with 63-fold magnification. Here, a pinhole can be adjusted relative to the sample in order to spatially filter out the signals of interest. Spectral filters separate scattered light from the excitation source. The image is then focussed with a net magnification of 100.8 onto the entrance slit of an imaging spectrometer and subsequently detected by a CCD camera. An adjustment of the sample position can be performed via coupling the emission into a video camera, giving a direct feedback for finding appropriate sample positions. A scheme of the experimental setup is shown in fig. 2.13.

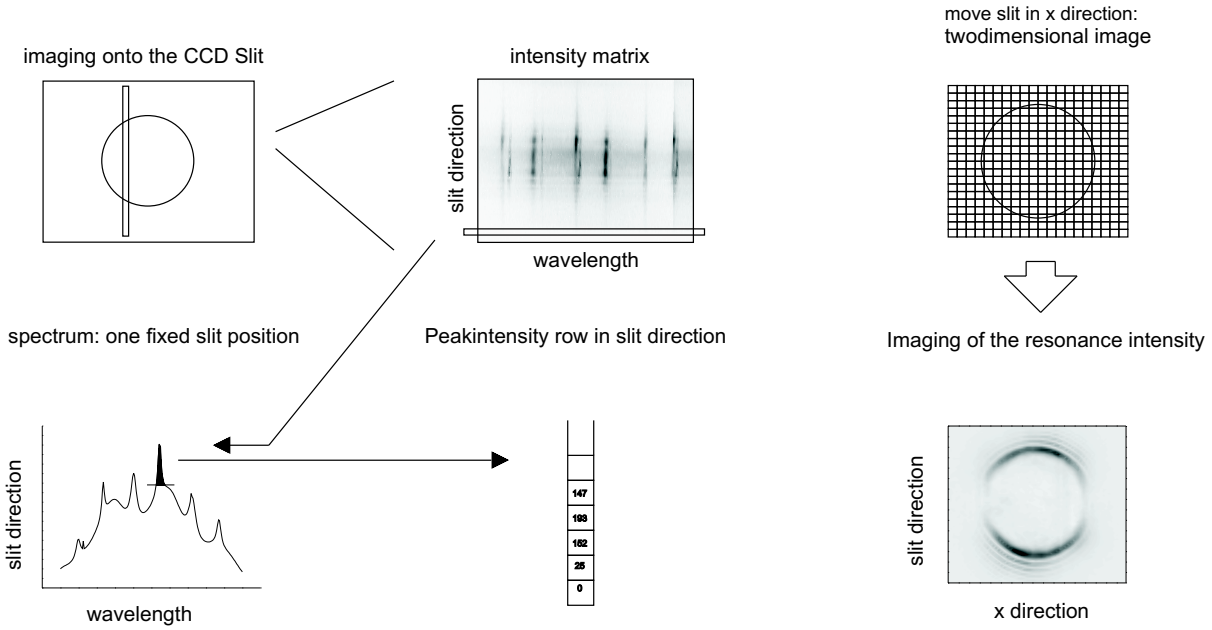

Figure 2.14: Scheme of the mode mapping technique: The nonresonant photoluminescence is spatially and spectrally scanned by shifting the sample image across a spectrometer slit. For any point of the resulting two-dimensional image a spectrum is measured. The integrated intensities of the resonances are visualized in a reconstructed spatial matrix.

In order to study the effects of localization and the polarization nature of the microsphere trapped nanocrystal emission, a polarization-sensitive and spatially and spectrally resolved mode mapping technique has been performed. A scheme of the mode mapping technique is depicted in fig. 2.14.

The image of single or coupled microspheres is focussed onto the entrance slit of a spectrometer as described above. The detected intensity is dispersed in the spectrometer and falls onto an imaging CCD attached to the exit image plane of the spectrometer. Thus, the CCD matrix detects a two-dimensional dataset containing the spectral information in one direction and the spatial information along the slit dimension in the other, i.e., for any point along the spectrometer slit a spectrum is obtained. The acquisition of the spatial information in the dimension perpendicular to the slit direction is performed with a stepwise movement of the sample image across the spectrometer slit. This is achieved via an electronic control of the position of the microscope objective, which is mounted on a x-y-z piezo stage. For any shift of the microscope objective, the CCD information is read out, resulting in a two-dimensional image, in which for any image point a photoluminescence spectrum is obtained. Additionally, a polarizer can be inserted into the detection beam path, resulting in an intensity dataset dependent on four parameters.

From this dataset, mode images can be constructed [Möl02, Möl01]: For a given resonance energy and a specific polarizer direction, a spectrum for the two spatial directions is evaluated. As a measure for the resonance intensity, a spectral window around the resonance peak is fixed, for which the peak integral is computed. Intensity values measured at neighboring wavelength positions around this spectral window then fix a base line, which

is set as the background for a specific resonance. This background can be subtracted from the peak integral and plotted for any point of the two-dimensional sample image. Thus, an analysis of measurements with varied polarizer positions can reveal both the light localization and the polarization properties of the detected structures.

2.4 Nanostructured Semiconductors

2.4.1 Growth of Semiconductor Nanocrystals

The samples covered in this thesis have been prepared by Dr. M. Artemyev (Belarussian State University, Minsk) via a wet chemical synthesis. First of all, this method allows to precisely control the nanocrystal radius, and thereby the extension of the confinement potential, which according to eqs. (2.37) and (2.38) results in a tunable emission energy. Not less importantly, the chemical procedure allows for flocculation and re-dissolution of nanocrystals for chemical functionalization with e.g. surface molecules, which becomes essential especially for linking to the surface of microresonators. For example, nanocrystals can be easily linked to or incorporated in polymer or glass-like material, see e.g. [Ols04].

The CdSe nanocrystal growth is performed using a route initially introduced by Murray *et al.* [Mur93, Hin96, Tal01]. Cadmium and selenium is added to a TOP/TOPO (trioctylphosphine/trioctylphosphine oxide) solution in the form of selenium powder and dimethylcadmium. Heating of the solution leads to a separation of cadmium out of its organometallic compound and the nucleation of CdSe clusters starts. The agglomerates are held in solution by the TOPO molecules whose oxygen part can dock with the cadmium ions of the nanocrystal, whereas the three octyl ends hinder the flocculation out of the TOP solution. The nucleation then leads to a nearly spherical crystal shape due to minimization of the crystal surface. The nanocrystal size can be monitored simultaneously by absorption measurements. The size is mainly determined by the growth duration. The reaction can be stopped via adding continuously methanol, a molecule with a higher polarity, to the solution, which lowers the solubility of the TOPO capped nanocrystals. Since the larger nanocrystals leave the solution first, the size can be controlled in a very narrow range, leading to a monodispersity of about 4%. A transmission electron microscope (TEM) image of a spherical CdSe nanocrystal is given in figure 2.15.

To passivate the nanocrystal surface and to improve the confinement potential, a surface layer of a compound semiconductor with a larger bandgap, ZnS is finally grown on top. For this Zinc and Sulphur are added as organometallic compounds to a CdSe nanocrystal solution in TOPO and HDA (hexadecylamine) [Tal01]. Heating of the solution leads to nucleation of ZnS on the CdSe surface, until the strain due to the lattice mismatch stops the layer growth after one or two monolayers. The nucleation principle is schematically displayed in fig. (2.4.1). After surface passivation, the quantum yield of spherical nanocrystals can reach values of around 70%, even at room temperature. A modified

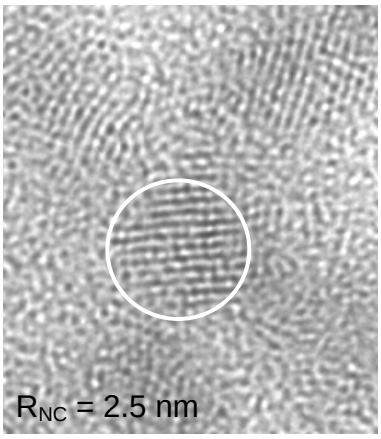

Figure 2.15: Transmission electron microscope image of a spherical CdSe nanocrystal. The nanocrystal radius is approximately 2.5 nm.

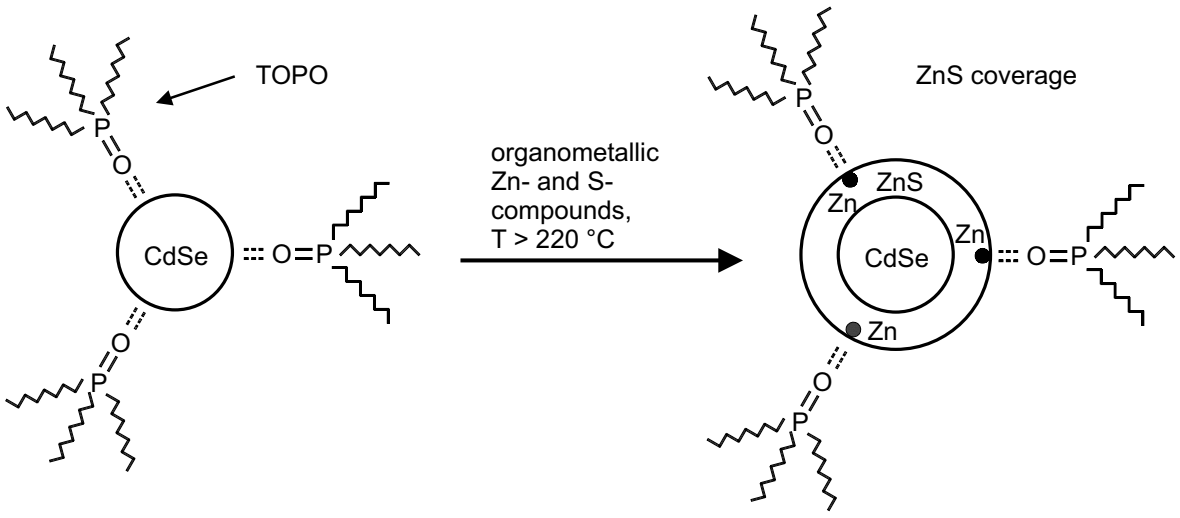

Figure 2.16: Schematic illustration of CdSe nanocrystal synthesis and capping formation.

preparation leads to the formation of elongated CdSe nanorods, as will be discussed in section 2.4.2.

2.4.2 Growth of Semiconductor Nanorods

The transition from spherical nanocrystals to elongated nanocrystals can be controlled by a modification of the wet chemical synthesis mentioned in subsection (2.4.1). For gaining the anisotropic growth, one uses the anisotropy of the hexagonal lattice of CdSe. During the growth, the c-axis of the crystal (the vector perpendicular to the (001)-facet) is energetically preferred as growth direction, as was initially discovered by A. P. Alivisatos' group in 2000 [Pen00]. The proposed growth mechanism assumes a different degree of passivation of outer cadmium bonds on the different surfaces. According to Manna *et*

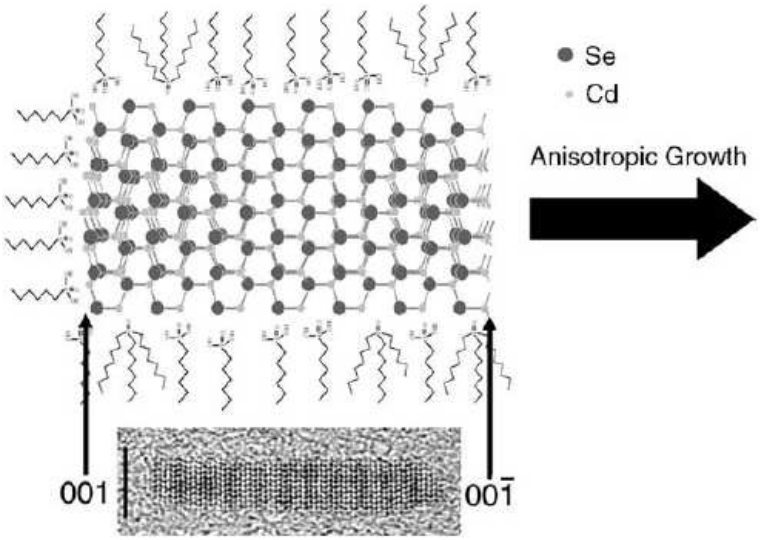

Figure 2.17: Growth mechanism in the CdSe nanorod synthesis. The different nanocrystal facets incorporate CdSe with different growth rates due to passivation conditions, taken from ref. [Man02].

al. [Man02], the nanorod synthesis looks microscopically as follows: The nanorod growth starts with a nearly spherical nanocrystal, which already determines the radius of the latter nanorod. Now, hexyl phosphonic acid (HPA) is added to the solution, which passivates the different facets of the nanocrystal in a distinct way. Figure 2.17 displays the CdSe lattice together with the crystallographic axes. On the (001) facet, one might find either a cadmium layer with one dangling bond or a selenium layer. In the former case, cadmium atoms, which are the more cationic constituents in the compound crystal, can be easily passivated by the phosphonic acid. In case of a selenium layer on top, which is not easily passivated by that acid, a subsequent growth of an additional cadmium layer would start, which finally leads to a termination of the growth in this direction. In the opposite (00-1) direction, the crystal is terminated with a layer of cadmium with three dangling bonds or a selenium layer. The three dangling bonds of cadmium can not be fully coated with the phosphonic acid molecules, so that in that direction the passivation remains always imperfect. Since the other nanocrystal faces can be completely passivated, further growth can only proceed in the (00-1) direction.

2.4.3 Nanocrystals as Dipole Emitters

The highly anisotropic shape of CdSe nanorods gives rise for significant changes in the optical properties compared to spherical nanocrystals. Most importantly in this context, as has been demonstrated by Hu *et al.* [Hu01], the nanocrystal emission is highly linearly polarized along the rod axis for sufficiently large aspect ratios (fraction of length to diameter of the nanocrystal), whereas the luminescence energy is mainly determined by the nanorod radius. The origin of the high degree of linear polarization has been investigated in various approaches. Hu *et al.* applied a pseudopotential calculation in

order to evaluate the change in the electronic states with increasing aspect ratio. The electronic states have their origin in the 4p electron orbitals of selenium and the 5s orbitals of cadmium. The energetic degeneracy of the p orbitals is removed by spin-orbit coupling and crystal field interaction. In a spherical nanocrystal, the highest electronic states have mainly $4p_x$ and $4p_y$ character, the $4p_z$-like states are lower in energy. Since the p_z level has a higher momentum projection in the nanorod axis, this state reacts most sensitively to a change of the rod length. When exceeding a certain value, the $p_x p_y$ and p_z states cross, and the p_z state becomes the highest electronic state. The major sensitivity of photoluminescence to these electronic states predicts highly linearly polarized emission. Recently, analytical calculations covered the regime of one-dimensional excitons [Sha04] and predicted a polarization degree of 0.6 for pure electronic confinement. More recently, analytical calculations including Coulomb interaction, exchange interaction and dielectric confinement in the 1D exciton picture reveal even higher degrees of linear polarization exceeding 0.8, in close agreement with experiments [LeT05a].

2.5 CdSe Nanorods as Dipole Emitters for Mode Control

The highly polarized emission from CdSe nanocrystals is evidenced in photoluminescence spectra obtained from a row of one-dimensionally aligned nanorods, as demonstrated by Dr. M. V. Artemyev [Art03a]. Here, a nanotemplate has been used for the attachment of core-shell CdSe nanorods. A one-dimensional alignment has been achieved by choosing a smaller template diameter than the rod radius. In fig. 2.18 photoluminescence images are displayed, which compare the polarization properties of the emission from elongated nanorods and almost spherical nanocrystals. In this image, photoluminescence images and spectra are taken for nanorod and nanocrystal samples with an analyzer in the detection system aligned parallel or perpendicular to the ensemble, respectively. The photoluminescence data indicate up to 70 % polarized photoluminescence. Likewise, the polarization degree of single nanocrystals can be determined from single rod measurements and detuning measurements in two-dimensional ensembles.

In the following, we will explore the utilization of the polarized CdSe nanocrystal emission for mode control in spherical microcavities. Here, we will make use of the interplay of cavity mode polarization and polarized emitters in an artificial compound system.

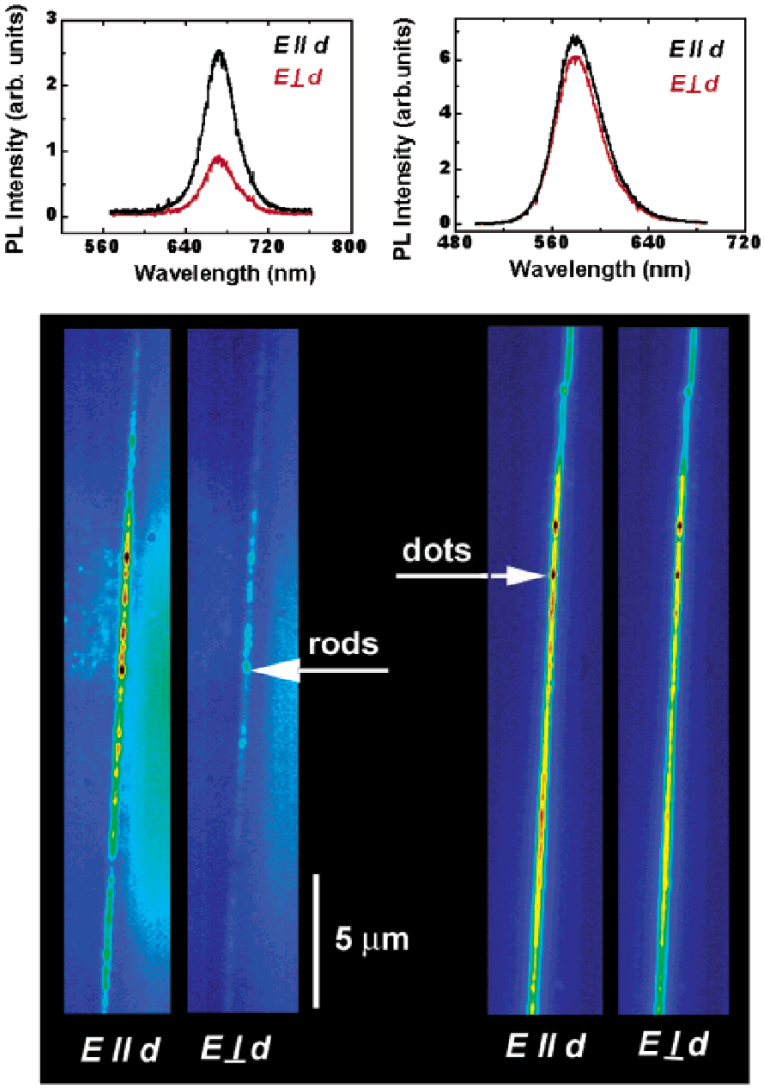

Figure 2.18: Polarized photoluminescence of CdSe nanorods in a one-dimensional ensemble compared to the nearly unpolarized nanodot emission. Both spectra and video image show the different polarization degree of CdSe nanorods, taken from ref. [Art03a].

3. Mode Control in Spherical Microcavities

In this section, we focus on the coupling of nanoengineered light emitters to dielectric microspheres*. An active control of the mode excitation will be presented, which results in a preferred excitation of modes with a specific polarization (see also subsection 2.1.1). To achieve this, we make use of both the characteristic properties of the nanoemitter emission and the light confinement in dielectric microspheres.

In spherical microcavities, the mode spectrum is composed of two mode polarizations — transverse electric modes and transverse magnetic modes, which are not energetically degenerate. As discussed previously, the nanocrystal emission can become highly linearly polarized, when nanocrystals are synthesized as elongated rod-like crystals. Both properties can now be combined to a compound system with nanorods attached to the microsphere surface. Due to the tangential orientation of the electric field vectors in transverse electric modes, an efficient excitation of TE modes is feasible, if nanorods are tangentially aligned on the microsphere surface. In other words, the transition dipole moment of nanocrystals can be engineered to realize an efficient coupling of nanoemitters to specific microcavity fields. One one hand, this interest is inspired by recent advances in preparation of strongly coupled emitter-cavity systems. Here, excitonic resonances are strongly coupled to cavity light fields [LeT05b, Rei04, Yos04, Pet05] and the exciton energy is coherently exchanged between excitonic states and the cavity light-field, which is currently investigated in the context of cavity quantum electrodynamics. Since optical microresonators doped with light-emitting semiconductor quantum dots form an unique artificial material system for the realization of microlasers as well [Wog03, Kaz04, Rak03], an optimization of the light-matter interaction and thus an orientation of the dipole moment with respect to the cavity light field is a similarly important parameter for the optimization of microlasers.

In earlier work, an engineering of position and orientation of the transition dipole moment with respect to the cavity field has been suggested in experimental work on dye-doped microdroplets [Bar96, Arn97, Hil96]. An extension to more stable systems is highly desired, since dye molecules are comparatively sensitive to laser excitation. Nanorods, on the other hand, exhibit stable photoluminescence and offer a high flexibility to tune the photoemission to desired wavelengths. Additionally, nanorods show small excitonic emission linewidths and thus represent an attractive choice as active material in microlasers

*Parts of the content in this chapter have been published previously as an article:
Appl. Phys. Lett. **83** (16), 2686-2688 (2003), ©2003 American Institute of Physics, ref. [Möl03]

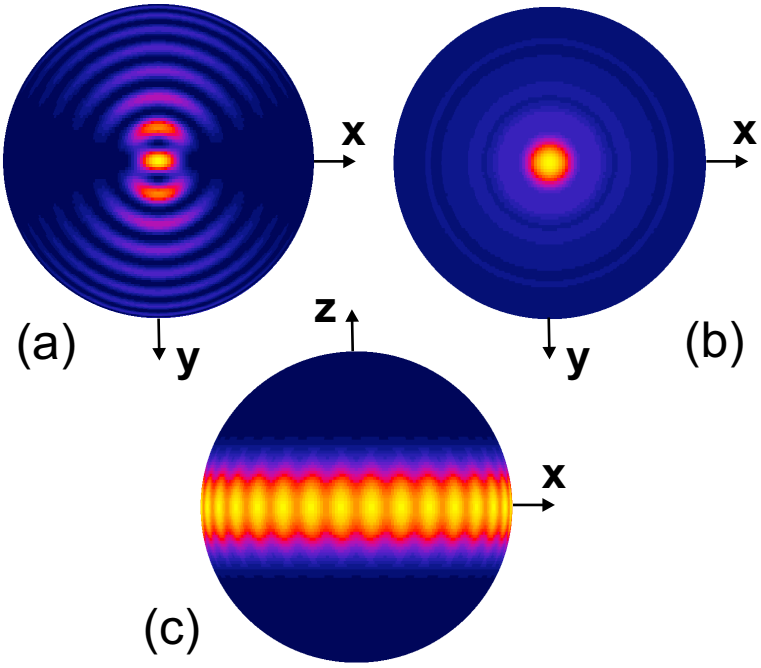

Figure 3.1: Calculated mode types for different excitation conditions in a spherical resonator with Radius $R = 1.4$ μm and refractive index $n = 1.57$. In (a) the dipole radiates tangentially to the surface in x-direction resonant to a TE^1_{16} mode ($\lambda = 688.5$ nm). In (b) a TM^1_{16} mode excited by a tangentially aligned dipole (oscillation in z direction) is shown ($\lambda = 666.9$ nm). The whispering gallery mode pattern, typically excited in plane wave excitation is given in (c). The images show the square of the electric field in the sphere surface in a linear color scale, calculated by via the multiple multipole (MMP) method (contributed by Dr. R. Wannemacher, Leipzig, taken from ref. [Möl03]).

[Art01a, Art01b, Pal03a, Fan01]. Moreover, microdroplets as host cavities continuously evaporate and do not allow for stable arrangements on substrates. Therefore, solid-state microspheres made from polystyrene are explored here as cavities (the possibility to arrange them in symmetrical ways on substrates will be discussed in the next chapters).

In fig. 3.1, numerically calculated microsphere modes are shown for surface aligned dipole emitters. In fig. 3.1 (a), the dipole is aligned tangentially to the surface of a 1.4 μm sphere with a horizontal orientation. The dipole oscillation here has been chosen to be resonant to the TE^1_{16} mode at a wavelength of $\lambda = 688.5$ nm. As apparent from the image, the emission is mainly localized at the dipole position and radiation into the mode occurs perpendicular to the dipole axis. Fig. 3.1 (b) shows a radially aligned dipole, which is in resonance with the TM^1_{16} mode. In this configuration, the light is isotropically emitted into a shell-like mode. The intensity is mainly located at the dipole position. For comparison, image (c) shows a whispering gallery mode excited with a plane wave. Here, the light is confined to a homogenously bright ring along the sphere equator. A rigorous theoretical discussion of dielectric microsphere modes excited by single incorporated dipole emitters can be found in [Che76].

Additionally, the plots shown in figs. 3.1a) and b) yield a second strong field maximum

in the mirror point of the nanorod position (see also [Möl02]). This may offer interesting applications in coupling individual nanorods located in the two mirror positions, e.g. to transport information over distances by cavity photons via Förster energy transfer, which has been discussed in [And00].

Since the proposal for a cavity mode control relies on the relative orientation of the nanocrystal axis and the electric field vectors, first a characterization of the cavity mode polarization has been performed. Polystyrene microspheres with a radius of 1.4 μm have been doped with a subsurface layer of spherical nanocrystals, whose emission can couple to both types of polarized modes. As can be shown theoretically, the mode properties are not significantly affected by incorporation of nanometer sized particles into a dielectric microsphere [Che03].

3.1 Cavity Mode Characterization

The mode identification has been achieved by applying polarization-sensitive mode mapping resonant to the different sphere resonances as discussed in subsection 2.3.5. The detected mode intensity is mainly localized close to the sphere rim. The polarization sensitivity is realized by a linear polarizer placed into the detection beam path. The cavity mode characterization is depicted in fig. 3.2 together with a microsphere photoluminescence spectrum. From the detected mode maps (shown as insets in diagram 3.2) the cavity mode polarization can be unambiguously derived: For all images, the polarizer is aligned horizontally in the mode diagrams. The intensity of each mode is concentrated in rings along the microsphere rim. The polarizer in the detection beam path projects now intensity contributions in accordance with the transverse polarization character of the microcavity field. The transverse electric mode, for which the electric field is aligned tangentially to the rim of the sphere, displays now a strong intensity maximum at those positions, at which the rim is oriented parallel to the polarizer orientation (see, e.g. the TE^1_{17} mode in the spectrum). For the transverse magnetic mode, the electric field is almost radially oriented. The resulting mode maps — with the same polarizer orientation as used for the TE mode maps — appear now rotated by 90 degrees. As can be seen in fig. 3.2, the mode polarizations can be determined for all occurring resonances and show an alternating set of TE/TM polarized modes. This mode characterization is cross-checked by a Mie scattering calculation according to eq. (2.14), which is displayed as the lower curve in diagram 3.2 together with the calculated mode polarizations and mode orders. The calculated mode polarizations are in perfect agreement with the measurement.

Since the cavity mode polarization has been unambiguously determined, a preference in the cavity mode excitation due to the nanorod alignment can be checked. In order to achieve this goal, microspheres of the same size have been doped with CdSe nanorods prepared as described in section 2.4.2. First, an electrostatic attachment method has been used, tangentially aligning a monolayer of nanorods on the microsphere surface. The alignment method is schematically depicted in fig. 3.3. The electrostatic attachment is

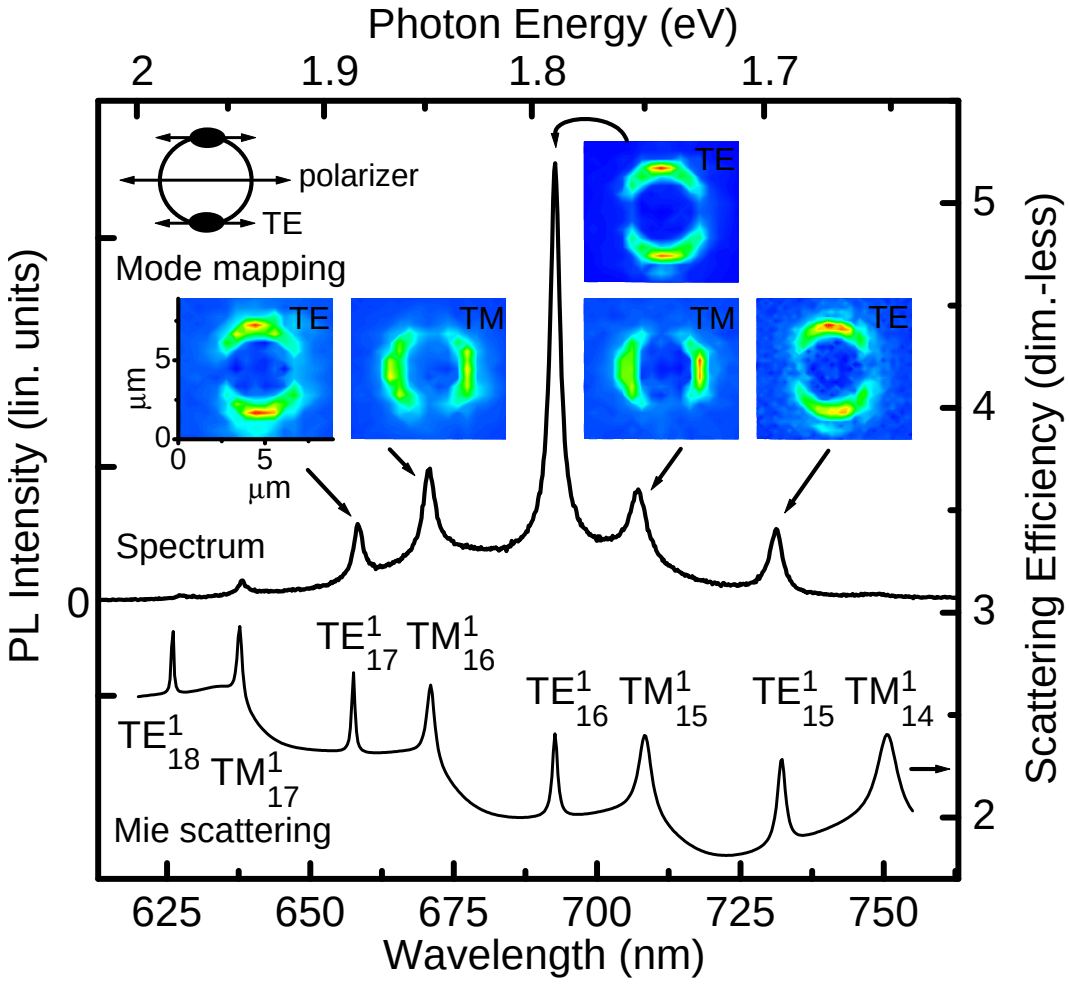

Figure 3.2: Analysis of cavity mode polarizations. The spectrum in the middle shows the photoluminescence spectrum of a nanocrystal doped polystyrene sphere. The color-coded polarization-sensitive mode maps show the experimental classification into transverse electric (TE) and transverse magnetic (TM) modes. The experimental classification is confirmed by a calculated Mie spectrum (Radius $R = 1.4$ μm and the refractive index $n = 1.5663 + 0.00785\mu\text{m}^2/\lambda^2 + 0.000334\mu\text{m}^4/\lambda^4$.)

made possible by opposite surface charges attached to the nanorods and the microspheres: Due to the fabrication process, polystyrene microspheres carry a surface layer of sulphate groups, which adds a negative surface charge to the microspheres in the suspension. Nanorods carry a positive surface charge, so that they rods are attached electrostatically to the microsphere surface leading to a tangential alignment of the nanorods. The averaged rod size derived from high-resolution transmission electron microscopy (TEM) images is 7 nm in diameter and 35 nm in length.

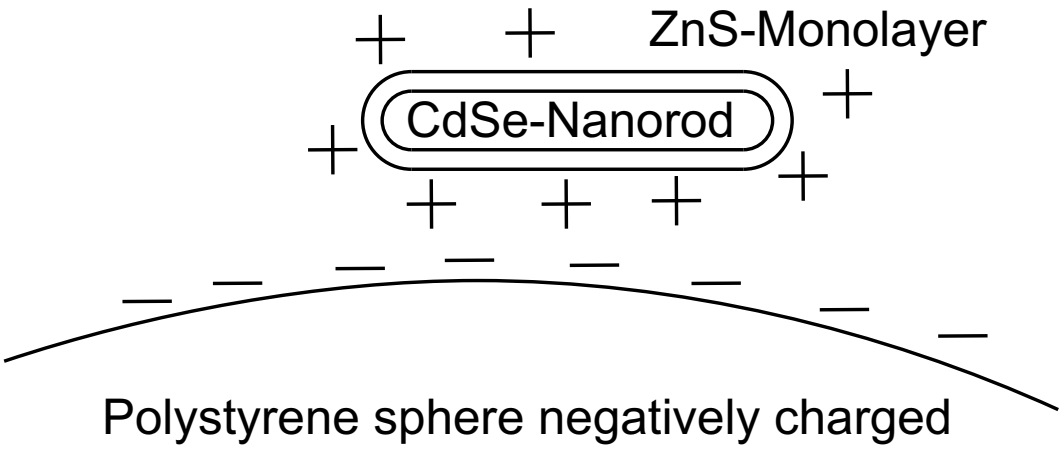

Figure 3.3: Tangential alignment of CdSe nanorods on the surface of polymeric microspheres. The nanorods are positively charged. The polystyrene microspheres contain negatively charged groups on the surface due to the fabrication process. The attractive force leads to an almost tangential alignment.

3.2 Mode Control

In order to check the preferential nanorod alignment and a preferential mode excitation of transverse electric modes, two samples with microspheres of the same size have been prepared: For one sample almost spherical nanocrystals are attached to the microspheres, for the other sample elongated nanorods have been used as dopants. The measured cavity spectra are compared in fig. 3.4.

Here, the spectra on the left hand side show the cavity spectrum excited by spherical nanocrystals. The spectrum is decomposed into TE and TM contributions with polarization-sensitive detection. Both mode polarizations are excited and the peak heights are simply weighted with the envelope of the nanocrystal emission (additionally shown as upper curve). Cavity quality factors (fraction of the mode energy and mode width) of about 1000 are observed. On the right hand side of the figure, the spectrum for tangentially aligned nanorods via the method mentioned above is shown. A sensitive comparison of the mode excitation conditions is possible for this sample, for which the nanorod emission displays a maximum for the TM mode wavelength. Now, a clear modification of the excited cavity spectra is noticed: Pronounced TE modes are observed, whereas TM modes are significantly suppressed. Hence, the spectrum is dominated by three TE modes. However, the cavity quality factors decrease to values between 200 and 600 because of the spacer molecule which results in a reduced incoupling.

Additionally, a preferential excitation of TE polarized cavity modes can also be derived from the pump power dependence of the mode emission as shown in image 3.6. Here, an alternative method of doping is applied: The nanorods are incorporated into the polystyrene microcavities beneath the surface, where the cavity mode field reaches its maximum. The incorporation of nanorods is undertaken in swelling polystyrene microspheres, as schematically depicted in fig. 3.5. Here, the microspheres develop pores, into

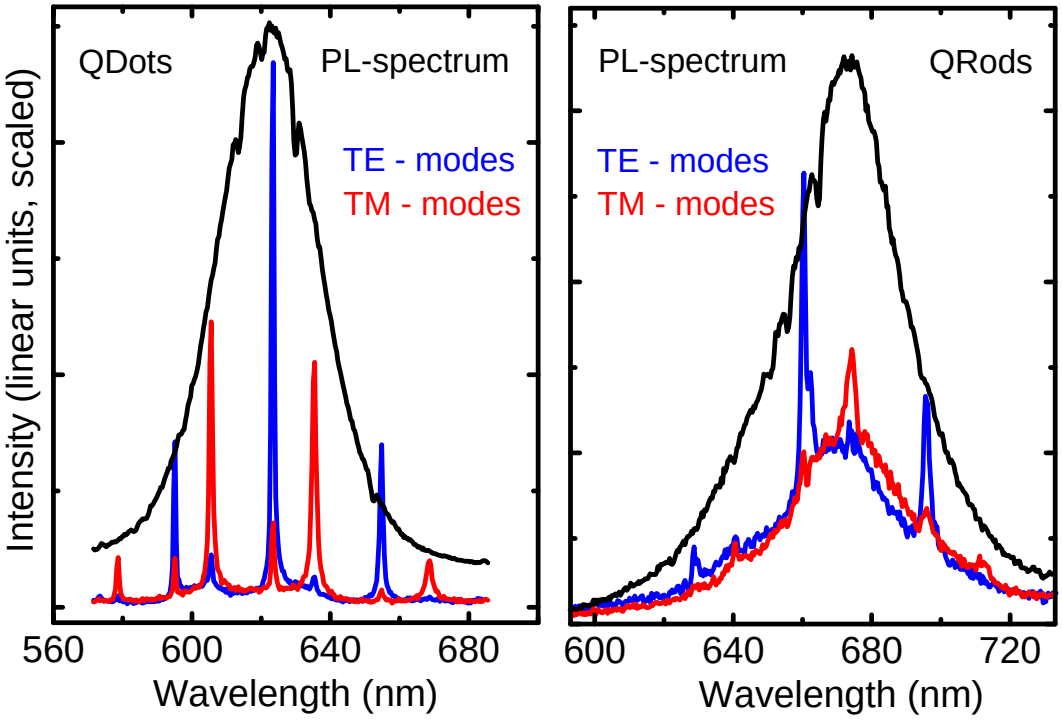

Figure 3.4: Cavity mode spectra excited by spherical and rod-shaped nanocrystals: The diagram on the left-hand side shows the microphotoluminescence spectrum in case of a polystyrene sphere doped with spherical nanocrystals. Both mode polarizations (TE and TM) are apparent in the spectra. The mode intensities are simply weighted with the nanocrystal emission envelope due to inhomogeneous broadening of the nanorystals (black line). The diagram on the right-hand side shows the mode excitation by tangentially aligned nanorods. TE-polarized modes show pronounced emission, whereas the TM polarized modes are significantly suppressed.

which nanorods can penetrate the sphere surface [Han01]. After the pores are closed, the nanorods are spatially confined in a subsurface layer close to the rim of the microsphere. Naturally, this method results in an imperfect alignment, however, the nanorod position is optimized here with respect to the mode field.

As indicated in fig. 3.6, the TE mode intensities exhibit a nonlinear increase in the pump power dependence for the TE mode at 731 nm, whereas the TM mode intensities remain almost constant (see inset of fig. 3.6). At sufficiently high pump power, the spectrum consists of two pronounced TE modes. However, a derivation of a specific threshold cannot be done, since the nanorods are subject to photo-degradation, so that the number of nanocrystals participating in the pump power dependence is still not constant.

As a summary of this chapter, the preferential excitation of transverse electric modes utilizing surface aligned CdSe nanorods has been demonstrated. The preferential excitation results in cavity emission spectra which are dominated by a subset of up to three TE polarized modes. Therefore, compound systems of nanorods aligned on a microsphere surface constitute almost completely TE polarized three-color emitters even at room tem-

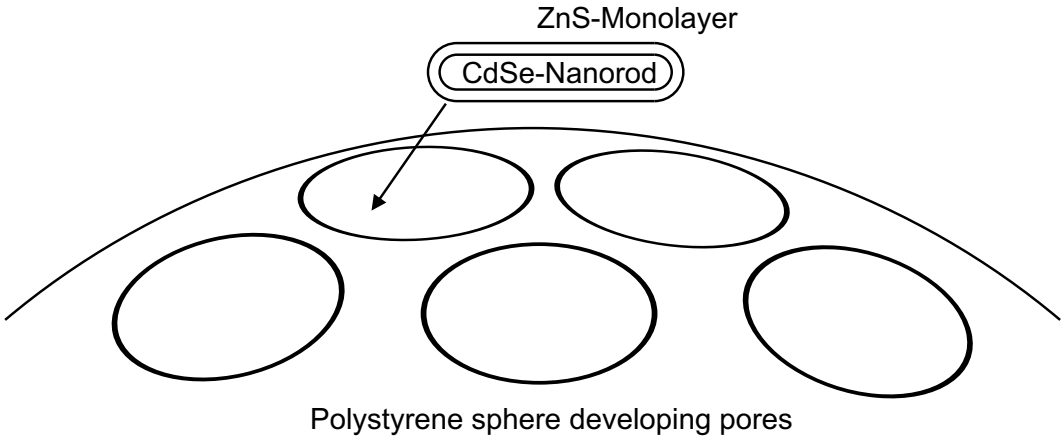

Figure 3.5: Incorporation of CdSe nanorods into polystyrene microspheres. The swelling microspheres develop pores, into which the nanorods can penetrate.

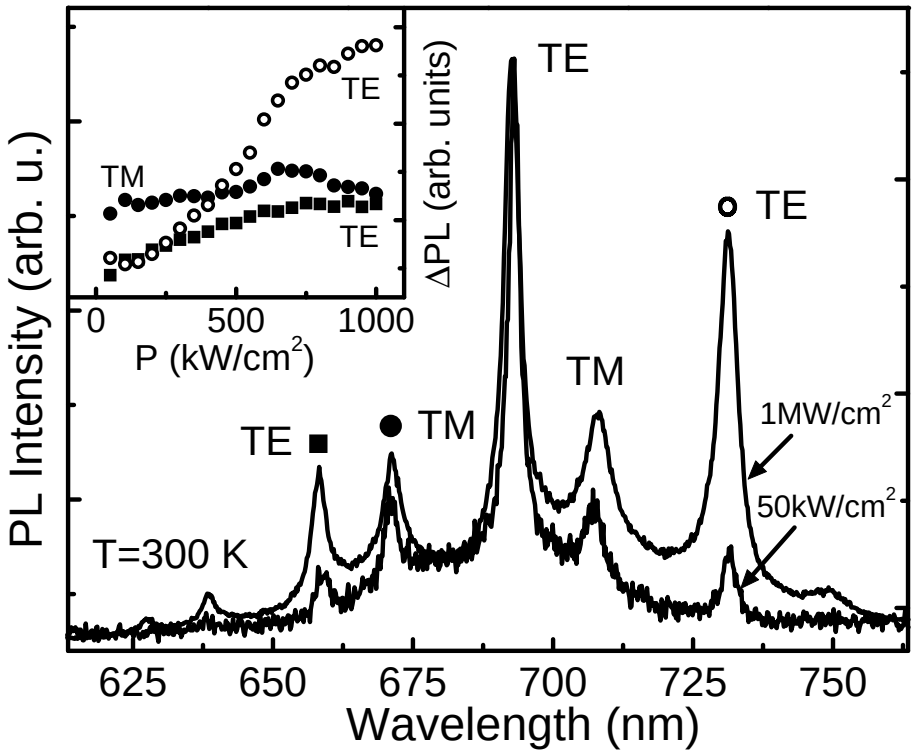

Figure 3.6: Pump power dependence of the photoluminescence emission. The emission spectra are normalized to the intensity of the most pronounced mode at 693 nm. The inset shows the intensity difference of the respective mode compared to the 693 nm mode dependent on the pump power (Taken from ref. [Möl03]).

perature.

4. Formation of Photonic Molecules

Recently, several possibilities to prepare multisphere agglomerates in a controlled and symmetric way arose. These include a variety of methods, like the use of microtemplates [Yin01, Wan04a, Xia00], applying wet chemical means for even heterogeneous structures [Réc04], symmetrical arrangements in drying droplets [Man03], and optical micromanipulation with optical tweezers [Mac01, Gri03], suggesting the possibility of three-dimensional photonic molecules and microscale optical manipulation applications.

Photonic molecule formation based on coupling of photonic dots has been reported for dye-doped polymeric bisphere systems and laterally patterned planar microresonators containing quantum wells as the optically active medium, [Muk99, Muk99, Bay98]. Lasing of a coherently coupled bisphere system is recently described [Har03]. Other applications of coupled resonators include optical filters, see e.g. [Mel02, Oka03], cascade lasers [Bor01] and coupled microlasers for memory devices [Hil04].

In this section, coherent coupling in small symmetric ensembles of polystyrene microcavities doped with nanocrystals is explored*. This study is motivated by the recent proposal of a new type of optical waveguide, the so-called coupled-resonator optical waveguide (CROW) [Yar99, Ste98]. The formation of coupled modes in small and finite linear chains and arrays of exactly size-matched spherical microcavities is characterized with polarization-sensitive mode mapping. The combination of polarization-sensitive mode mapping and spectral analysis at characteristic symmetry points of the molecule allows for the identification of weakly and strongly coupled bonding and antibonding modes and the determination of the dominant polarization type of the molecule states. Both experiment and theory show strong photon mode coupling with pronounced mode splitting as well as weak coupling with no significant loss in Q-factor depending on the emitter position and orientation. The spatial distribution and dominant polarization type of both the weakly and strongly coupled cavity resonances are studied spectrally and spatially resolved. The experimental data are compared with a calculation of field distributions and mode linewidths as a function of dipole orientation and position inside a photonic molecule. Q-factor conservation along molecule axes for weakly coupled modes is demonstrated as an important property of coupled-resonator geometries.

As will turn out in the following subsections, the localization of weakly and strongly coupled modes clearly reflects the symmetry of the multisphere configuration. Thereby, the

*Parts of the content in this chapter have been published previously as an article:
Phys. Rev. B **70** (11), 115323 (2004), , ref. [Möl04]

symmetry dependent features can be regarded as a photonic representation of *Neumann's principle* known from crystal physics, since the spatial symmetries are found in the mode diagrams as well [Bir66].

These observations provide us with insight concerning the modified light localization, strong and weak spectral mode splittings and stability in the mode polarization, which can be used to evidence coherent mode coupling in coupled-resonator chains (these criteria provide the basis for the next chapter, where results of an extended "hockey stick" geometry will be presented). A finite chain of three resonators in a linear geometry will be investigated and the stability of the coupled-mode evolution is shown. Additionally, measurements on the finite chain introduced in this chapter are used later on for a theoretical discussion of the mode evolution in truncated coupled-resonator optical waveguides. For the estimation of the dominant mode polarization, the coupled cavity structures are doped with a subsurface layer of spherical nanocrystals, which can excite both TE and TM polarized modes.

Interestingly, a symmetrical alignment of microspheres appears to be an attractive way to realize directional emission in cavity geometries with a circular cross section. Naturally, spherical microcavities exhibit spherically symmetric emission patterns, which impose constraints in their practical use, for example in microlasers. In order to realize directional emission, symmetry axes have been introduced recently into originally isotropic cavities by shape distortion for deformed microdisks [Gma98, Kim04], by constructing egg-shaped resonators [Shi01] and by slightly deforming microspheres [Lac03]. More complex coupled-resonator geometries are less studied. Confinement of light in photonic molecules composed of microspheres might open a way to optimize cavity parameters by creation of a more complex cavity structure than a single microsphere.

4.0.1 Samples and Experiment

The photonic molecules were prepared by impregnating polystyrene microspheres (Polysciences, Inc., radius $R \approx 1.4$ μm, refractive index $n \approx 1.59$) with a subsurface layer of CdSe nanocrystals of $R_{\mathrm{NC}} = 2.5$ nm according to the procedure described in chapter 3. After synthesis of CdSe nanocrystals described in subsection 2.4.1, the methanolic suspension of microspheres was cast and dried on a quartz substrate thereby forming a great variety of assemblies.

To achieve coherent photon coupling, exactly size-matched microspheres ($< 0.1\%$ size deviation) have been preselected via their Mie resonances. Due to the weak interaction required for the realization of a CROW, the dimensions of the microspheres to be utilized are generally larger than the cavities which are used to build up photonic bandgap materials (for photonic crystals made from polystyrene spheres, see e.g. [Wos03]). In order to obtain sufficiently large coupling effects, a radius of 1.4 μm has been chosen. The photonic molecule modes are studied by microphotoluminescence spectroscopy at the diffraction limit combined with polarization-sensitive mode mapping. The spectra and the spatial

intensity distribution are taken with a spatial resolution of 0.4 μm and a spectral resolution of 0.2 nm at room temperature as described in subsection 2.3.5. The emitted light intensity of NC-doped spheres is spectrally and spatially resolved by mapping the intensity across a sphere on and off resonance to molecule modes for a fixed polarization direction. Since additional modes are found in the spectra, a polarizer inserted into the detection beam path selects only signals from nanocrystals that emit components of the electromagnetic field parallel to the orientation of the polarizer. In that way the the total mode spectrum detected in small spatial regions of the structure can be decomposed into subsets of either TE- or TM-like modes for more clarity in the data analysis as described in 2.3.5. By the narrow spectral window and the chosen polarizer orientation, we introduce a size selection of nanocrystals from the inhomogeneously broadened ensemble that is exactly in resonance to the investigated cavity mode and has components of the optical transition dipole moment according to the field orientation defined by the polarizer axis.

4.0.2 Symmetrical Alignment of Microsphere Ensembles

A symmetrical alignment of below ten microspheres can be achieved by a wet chemical modification of the microsphere deposition onto the substrate [Art02] : The nanocrystal doped microspheres are dissolved in a methanolic suspension which easily evaporates at room temperature. The suspension is given onto the substrate, which results in a large droplet. During evaporation of the methanol, the droplet shrinks in size. Small defects on the substrate surface introduce inhomogeneities in the droplet boundary, which do not follow the movement into the droplet center direction. Instead, small separated droplets are formed, containing small numbers of microspheres. A careful control of the microsphere concentration in the suspension and an adjustment of the suspension amount relative to the substrate area during the deposition leads to the formation of a large number of these small droplets on the substrate. The droplets cover a spatial region on the micrometer scale and can contain small numbers of microspheres. During the evaporation of the methanolic solution, these small droplets slowly shrink, which finally moves the microspheres towards each other. Since the microspheres are randomly localized in the suspension droplet, the formation of highly anisotropic agglomerates is rather unlikely, and thus this method typically results in symmetrically ordered arrangements of touching microspheres, whereas the ensembles are distanced from each other by several microsphere diameters. Due to the self-assembly mechanism behind this method, large scale substrates can be covered with highly ordered ensembles, which allows for a preselection of ensembles with matching sizes that permit coherent coupling of the microsphere light fields. An interesting variant of this method has been published by Manoharan *et al.* on the formation of microsphere agglomerates using toluene droplets [Man03]. A scheme showing the assembly principle is given in diagram (4.0.2). A collection of selected microscope images of self-assembled symmetrical microsphere ensembles is shown in figure 4.2.

The demonstration of coherent coupling of sequentially attached microspheres will be performed by exploring the modification of the emission spectra and its dependence on

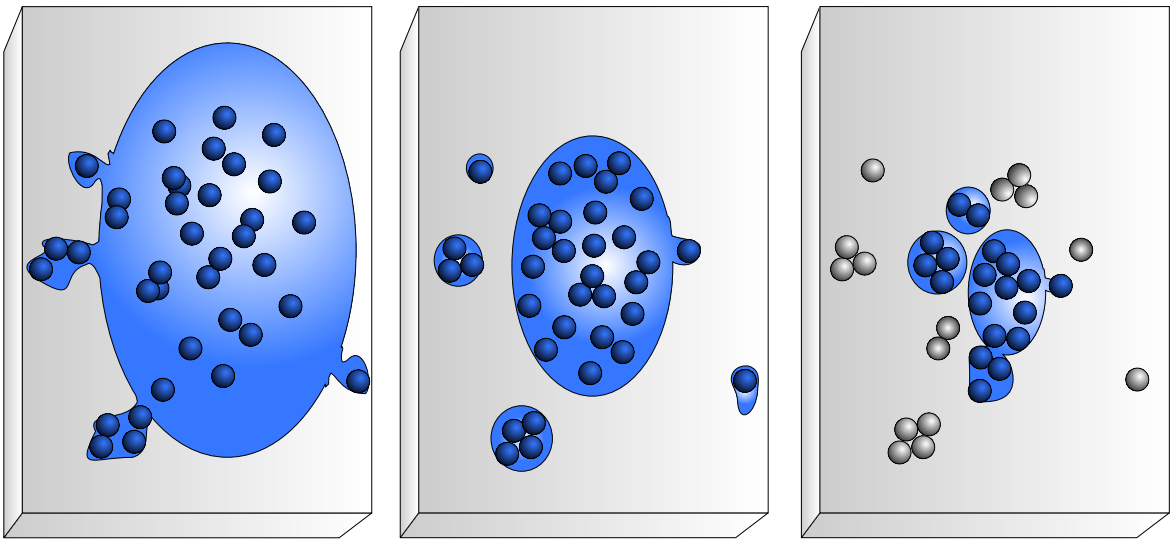

Figure 4.1: Schematic representation of the preparation of symmetrical microsphere ensembles: First, the solution containing doped microspheres is given onto the quartz substrate. During evaporation of the solution, the droplet shrinks. Due to inhomogeneities of the substrate surface, some parts of the solution do not follow the inwards moving droplet boundary (left image). Thus, smaller droplets are formed, from which many contain a small amount of microspheres (middle image). Further evaporation of the solution leads to a high number of small symmetrical microsphere agglomerates covering the substrate.

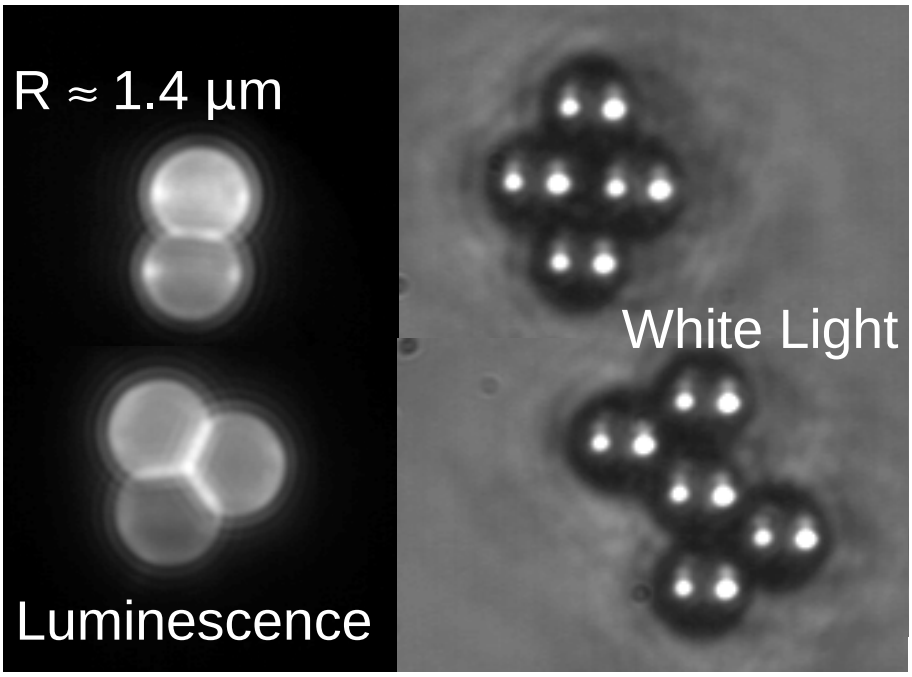

Figure 4.2: Collection of selected microscope images of self-assembled microsphere agglomerates. The images on the left hand side show photoluminescence images of nanocrystal doped sphere ensembles. On the right hand side, sample structures illuminated with white light are displayed.

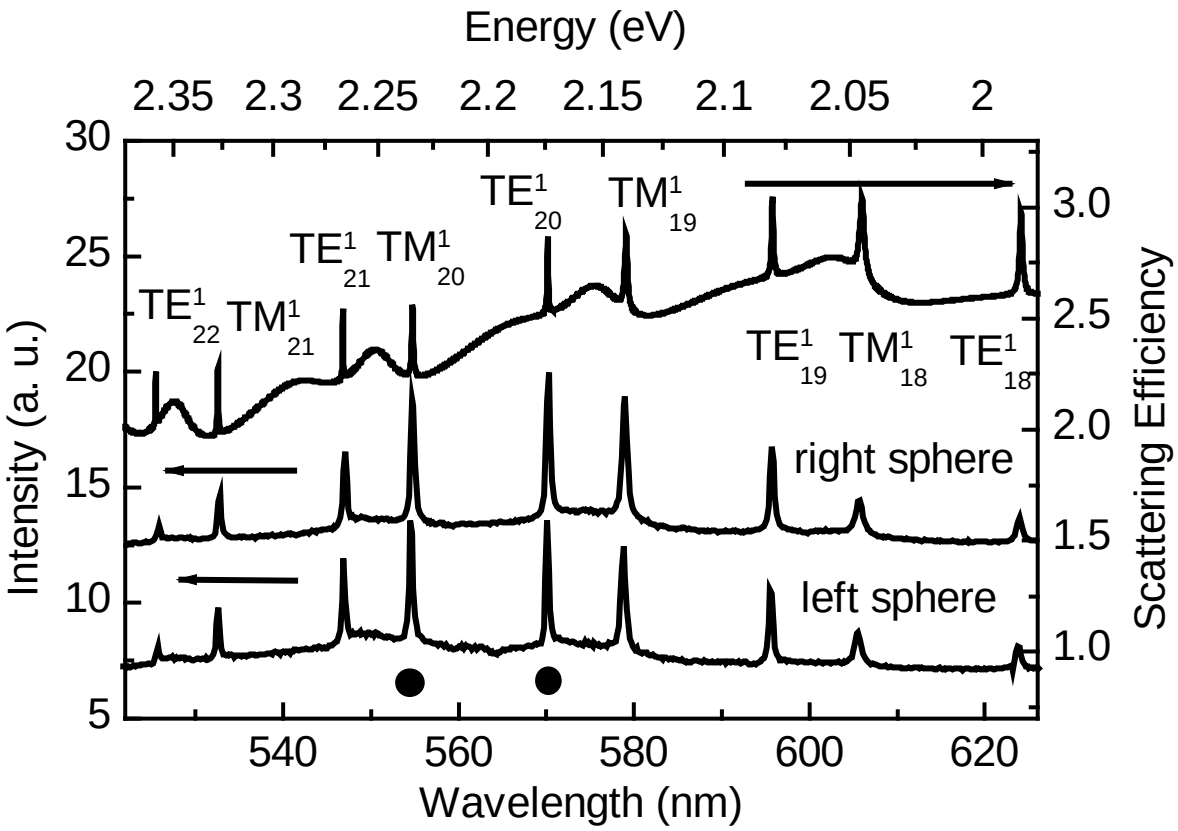

Figure 4.3: Photoluminescence spectrum of a two-sphere system with large intercavity distance. The lower curves display the experimentally observed photoluminescence spectra for each sphere (labeled with left and right according to the mode maps). No mode splittings or mode shifts are observed. The upper curve shows a calculation of the single sphere scattering efficiency according to equation (2.14). For the narrow resonances with radial mode number 1 the polarization type and angular quantum numbers are labeled. The emission wavelengths for later mode maps are indicated with filled dots.

the spatial symmetry of the multisphere arrangement in section 4.0.3. In order to check the dependence of the observed effects on the intercavity distance and hence the coupling strength for the observation of coherent coupling in a two-sphere system, we perform measurements on system of two distanced microspheres, where the intercavity separation is approximately one sphere radius. This will give a suitable comparison for the exploration of coherently coupled bispheres made of touching constituents.

Since the occurrence of coherent coupling in a two-sphere system does not only require a sufficient spatial overlap of the evanescent cavity field tails, but also a sufficient spectral overlap of the mode resonances, a pair of spheres has been preselected, for which the individual microsphere modes are exactly overlapping within the experimental error. Thereby, the intercavity distance is the only parameter, which can determine the coupling degree.

The mode resonances for the individual microspheres are detected at the boundary of each sphere and plotted in fig. 4.3. The microsphere modes are fitted with a Mie theory

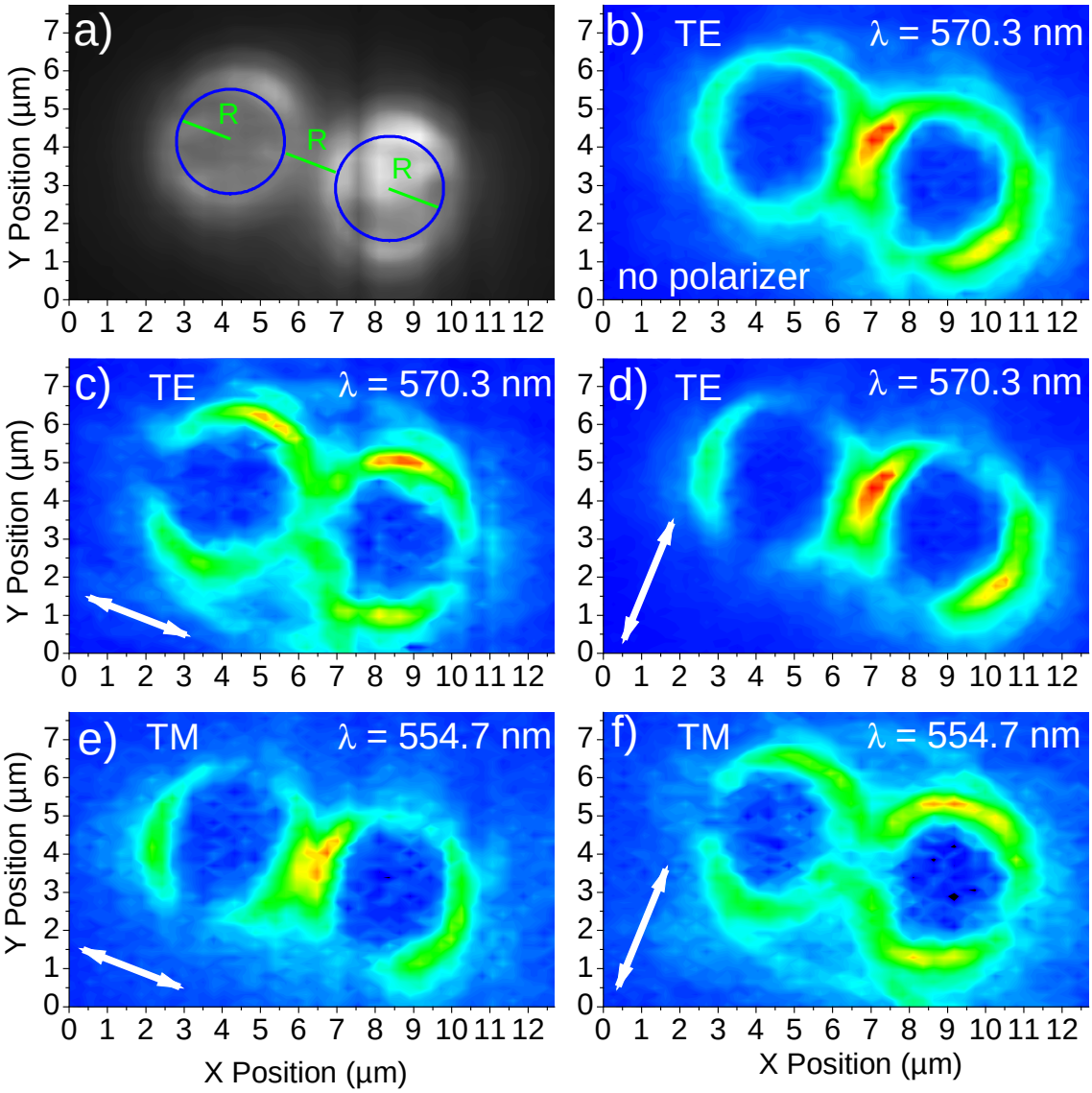

Figure 4.4: Polarization-sensitive mode maps of a double-sphere system with large inter-cavity distance. Diagram (a) shows the spectrally integrated emission of the two-sphere system. Diagram (b) shows an intensity map resonant to the TE^1_{20} mode at 570.3 nm without polarization decomposition. The diagrams (c) and (d) show polarization-sensitive mode maps of the same mode with polarizer orientations as marked by arrows. Diagrams (e) and (f) show the polarization-sensitive mode images for a TM^1_{20} mode at 554.7 nm.

calculation, which is given below the experimental spectra. From the comparison, no modification compared to single microsphere spectra can be attributed to the presence of the second microsphere. We perform now the polarization-sensitive mode mapping introduced in subsection 2.3.5, and map the mode intensity across the whole two sphere geometry and compare the results with the single sphere case. The polarizer in the detection beam path has been chosen to decompose the nanocrystal emission into two polarizations relative to the spatial two-sphere arrangement: One orientation is directed parallel to the connection line of the two sphere centers, the other being aligned orthogonally.

The polarization dependent mode maps are given in fig. 4.4 for two consecutive modes with TE and TM character, respectively. For comparison, the upper left diagram illustrates the spectrally integrated intensity of the two-sphere configuration (the geometry of the configuration has been highlighted with a cartoon). The unpolarized intensity distribution of a TE_{20}^{1} mode at 570.3 nm is displayed on the right hand side. In the second row, the polarization-sensitive mode map for the same TE_{20}^{1} mode for both orthogonal polarization directions are given (see arrows in the diagrams). The bottom row shows the mode maps of a TM_{20}^{1} mode at 554.7 nm with the same polarizer orientations (see arrows). For both modes, the emission intensity is concentrated at the rim of the individual spheres. For the TE modes, the intensity reaches the maximum at positions, where the rim of the sphere is oriented parallel to the polarizer direction, whereas the TM modes show the orthogonal behavior. By turning the polarizer to the orthogonal orientation, the intensity stemming from each sphere simply turns around individually by the same degree. This leads to the conclusion, that neither spectrally nor with respect to the intensity localization the distanced two-sphere system behaves differently compared to two isolated microspheres. Thus, for this configuration a distance of the order of one microsphere radius leads to almost vanishing signatures of coherent coupling. With this cross-check at hand, the coherent coupling in systems of touching bispheres can be explored.

4.0.3 Photonic Molecules Formed by two Coupled Microsphere Cavities

The simplest photonic molecule is a coherently coupled bisphere system which implements a preferred symmetry axis along the molecule axis. We therefore start with the analysis of bisphere emission spectra and field intensity distributions, which are excited here by the emission of CdSe nanocrystals near the surface of the microspheres. Figure 4.5 shows the emission spectra taken at characteristic detection points of a bisphere molecule, i.e., on- and off-axis with respect to the bisphere axis. The lower panel shows, for comparison, the scattering efficiency for a single sphere calculated via Mie theory. The labels TE_l^n or TM_l^n denote the polarization character (TE or TM) and the angular (n) and radial (l) quantum numbers, respectively[†]. For the analysis of the spectra we select in the following only one subset of either TE- or TM-type modes by polarization-sensitive detection. For example, the data in fig. 4.5 are detected as TE-sensitive by orienting the polarizer parallel to the bisphere axis for *off-axis* detection at the equator and perpendicular for *on-axis* detection at the pole.

For detection points off-axis near the equator (middle panel), the single-sphere TE resonance energies, e.g., the TE modes with $n = 1$ and $l = 17$, 18, 19, are well reproduced in the spectrum of the bisphere system. Because of the negligible spectral shift compared to the single-sphere TE-resonances, the mode type excited by nanocrystals at off-axis posi-

[†]For the size parameters used throughout this thesis, the larger quantum number always refers to the angular quantum number.

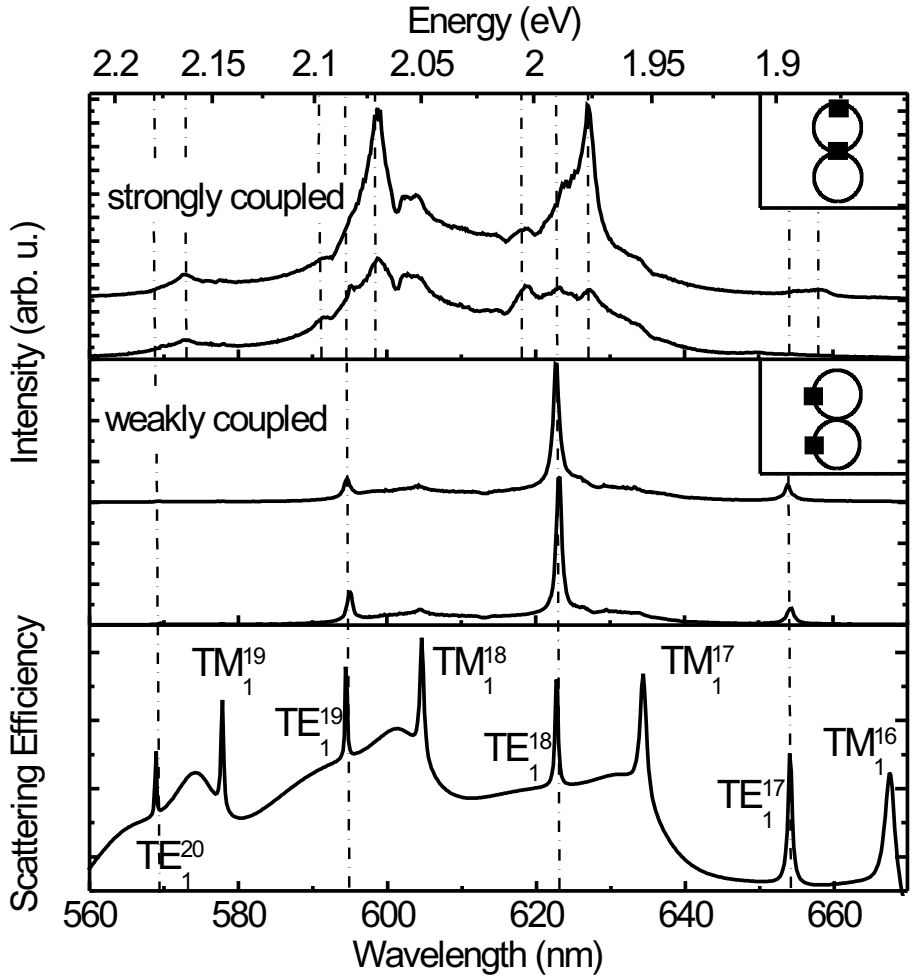

Figure 4.5: Emission spectra taken at characteristic bisphere points in TE-sensitive detection (linear polarizer aligned parallel to the sphere rim in the detection region); upper panel: red-shifted, bonding resonances measured at the intersection point (uppermost curve) and weaker, anti-bonding modes taken at the edge position; middle panel: spectra of the spectrally unshifted bisphere modes, taken at detection points apart from the bisphere axis; bottom panel: Mie-scattering spectrum for a single polystyrene sphere.

tions is called *weakly coupled* throughout what follows without further classification into bonding and antibonding modes. Spectra taken at the on-axis detection points (upper panel) show the characteristic mode splitting caused by coherent mode coupling, as has been demonstrated in ref. [Muk99].

While the weakly coupled modes show no significant spectral shift compared to the single-sphere resonances, they cannot be regarded as entirely uncoupled, as will be examined in the following section. In order to explore the differences with the uncoupled two-sphere system discussed before, the polarization-sensitive mode mapping is applied to the weakly coupled modes emerging from the TE_1^{19} single sphere modes at 596 nm. In order to unambiguously check the polarization behavior for the weakly coupled modes, the polarizer in the detection beam path has been turned in steps of 10 degrees starting form the bi-

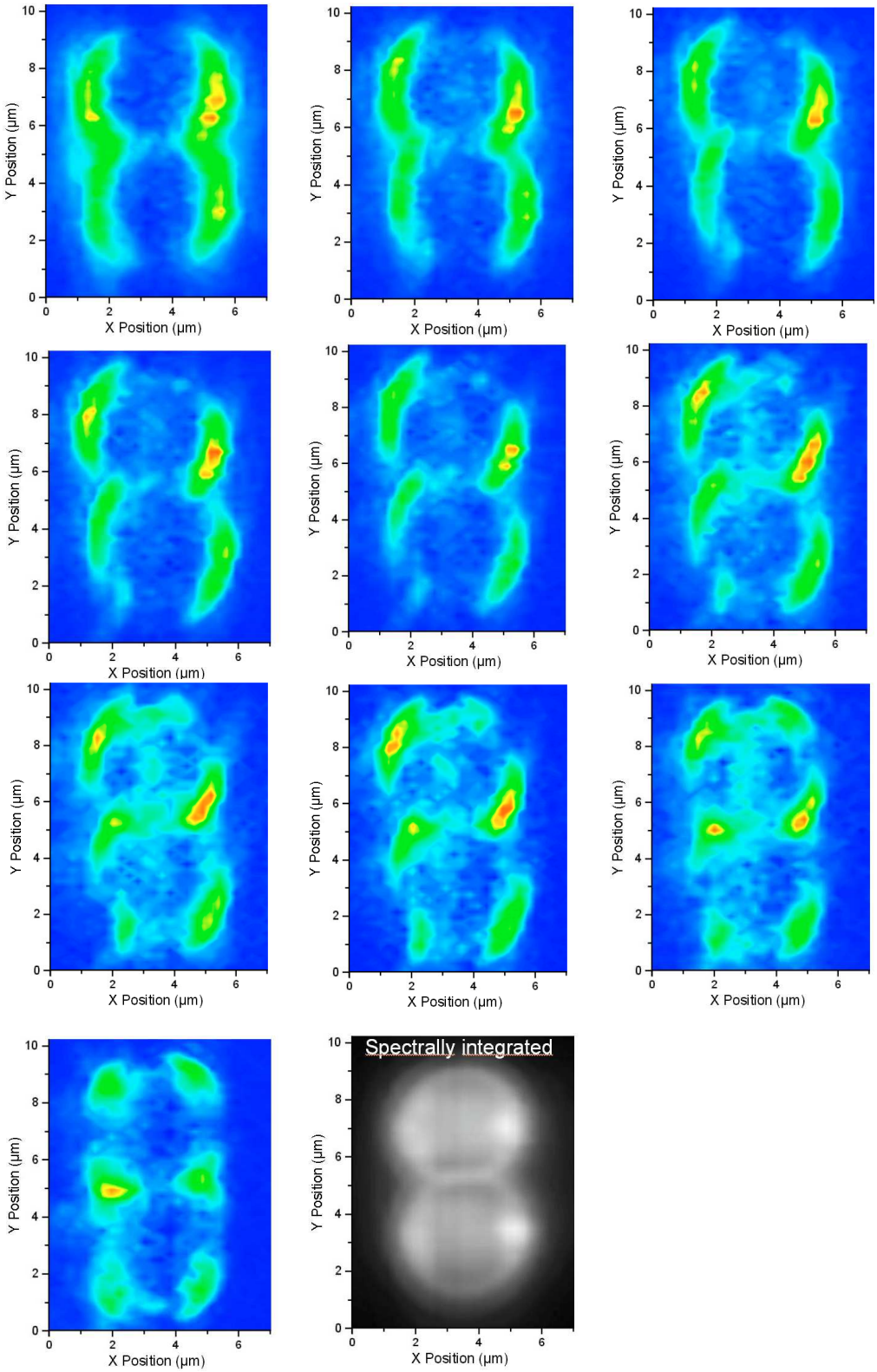

Figure 4.6: Polarization-sensitive mode maps of a double-sphere system with touching constituents. The detected TE_1^{19} mode intensity is shown for different orientations of the polarizer in the detection beam path. The polarizer is rotated from parallel to orthogonal orientation with respect to the bisphere axis. The last diagram gives the integrated photoluminescence for comparison.

sphere axis orientation towards the perpendicular direction. For each polarizer position, a two-dimensional mode map has been performed for the weakly coupled modes. The results are displayed in fig. 4.6 (here the detuning angles are arranged with increasing angle in rows from right to left and subsequently from top to bottom). For comparison, the spectrally integrated photoluminescence is given in the last diagram in fig. 4.6 to allow for the connection of the mode maps with the spatial configuration of the photonic molecule. As depicted in the first image at 0 degrees detuning, the map of the detected photoluminescence reveals at first glance no significant deviation compared to the case of a pair of uncoupled spheres: The intensity stems mainly from the rim regions of the individual microspheres, and the polarizer in the parallel configuration selects photoluminescence components with field vectors parallel to the polarizer, so that the intensity reaches its maximum at positions where the tangents of the sphere rims are parallel to the main axis. When the polarizer is further detuned from the molecule axis, the bright intensity spots initially follow the polarizer rotation as expected from the uncoupled sphere system. This behavior drastically changes at about 50 degrees detuning: Here, the mode intensity avoids the main axis of the configuration and bends over to the side regions of the photonic molecule. This behavior is preserved in all subsequent mode maps and reaches its maximum contrast for the 90 degree case, in which the polarizer is aligned perpendicular to the molecule's main axis. Here, the intensity displays additional *minima* along the axis, thus exactly at those spatial positions, which would exhibit intensity *maxima* for the case of uncoupled spheres. This behavior perfectly reflects the spatial symmetry of the bisphere configuration and can therefore be regarded as an unambiguous detection tool to decide about the occurrence of coherent coupling of the microresonator fields. Furthermore, it does not necessarily rely on a pronounced splitting of modes, which — in principle — could originate from various mechanisms, even in the single sphere case, like deviations from the spherical symmetry of the constituents; instead, it can readily be performed for spectral regions, where single sphere modes are expected. Because of the deviations from single mode intensity localization, the modes are labeled weakly coupled, opposed to simply uncoupled modes. On the other hand, the polarization character of the weakly coupled modes is not faced with complications due to interresonator coupling, as shown in fig. 4.6.

Since the interresonator coupling introduces significant changes of the spectrum at the bisphere axis, we follow here, as an example, the mode evolution at the bisphere intersection region. In fig. 4.7, the evolution of the weakly coupled modes into strongly coupled modes is displayed in TE-sensitive detection. Here, the evolution of the TE_1^{18} mode is shown for different detection spots shifted perpendicularly to the bisphere axis (see the horizontal stripe in the inset of figure 4.7). Apart from the main axis, the weakly coupled modes dominate the spectrum. The closer we approach the intersection region, the more are the modes shifted towards longer wavelengths, evolving into strongly coupled modes at the intersection region. Since microspheres, due to their spherical symmetry, confine a great collection of modes including varying angles with the bisphere axis, several modes contribute to the transition of weakly and strongly coupled modes. These modes exhibit

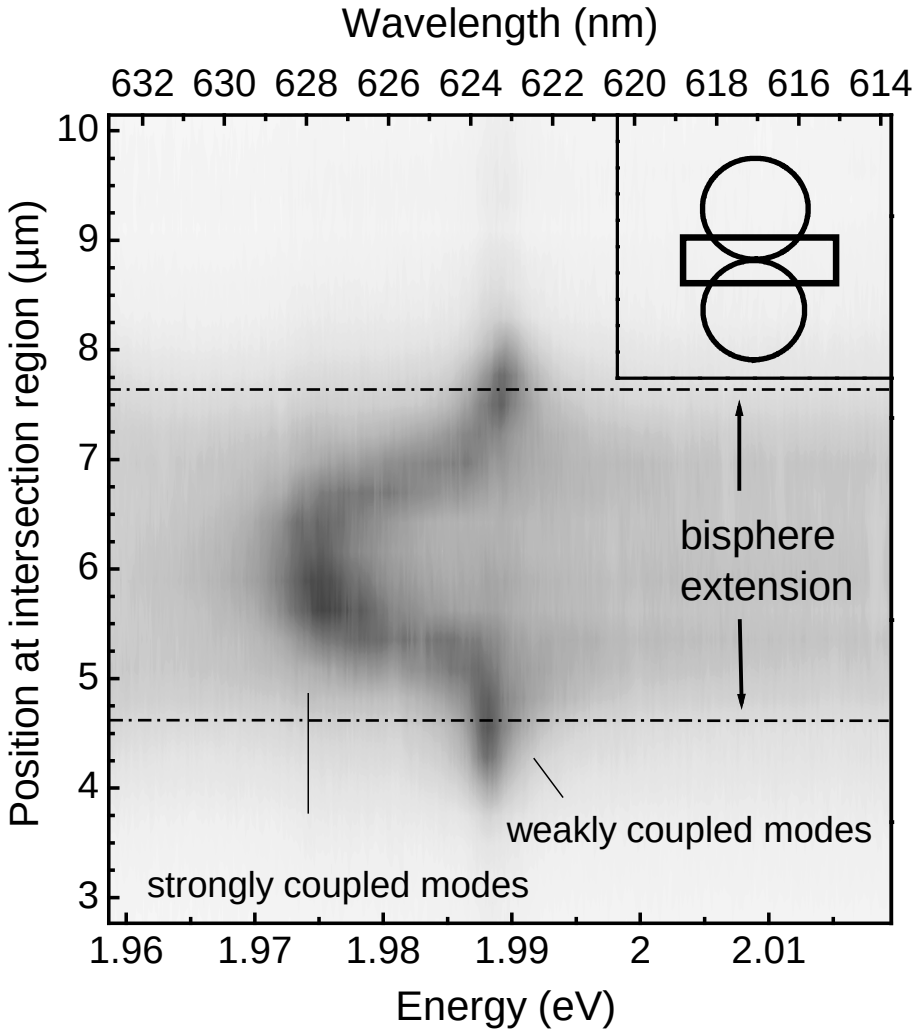

Figure 4.7: Transition from weakly to strongly coupled TE modes at varying distance from the bisphere axis. A strong splitting is observed at the touching point.

a different degree of field overlap, so that apparently there is a smooth transition of the weakly coupled modes towards the strongly split modes, as is illustrated in fig. 4.7.

Analogous effects are observed for the coupling of TM modes as we will discuss later for a linear three-sphere geometry.

These strongly coupled resonances can be classified into bonding or antibonding modes with the help of the intensity maps and by comparing the absolute intensity at the intersection region of the bisphere with the intensity at its end positions (see fig. 4.8). The redshifted mode at 627 nm (uppermost curve in fig. 4.5) represents a pronounced bonding character because of its high intensity signal at the intersection point compared to the upper and lower on-axis detection points and is referred to as a strongly bonding mode in what follows.

The polarization-sensitive and spectrally resolved intensity maps of both the spectrally unshifted, weakly coupled modes are shown in fig. 4.8. To extract the dominant polarization of the respective mode type, the intensity maps are again decomposed in TE and TM

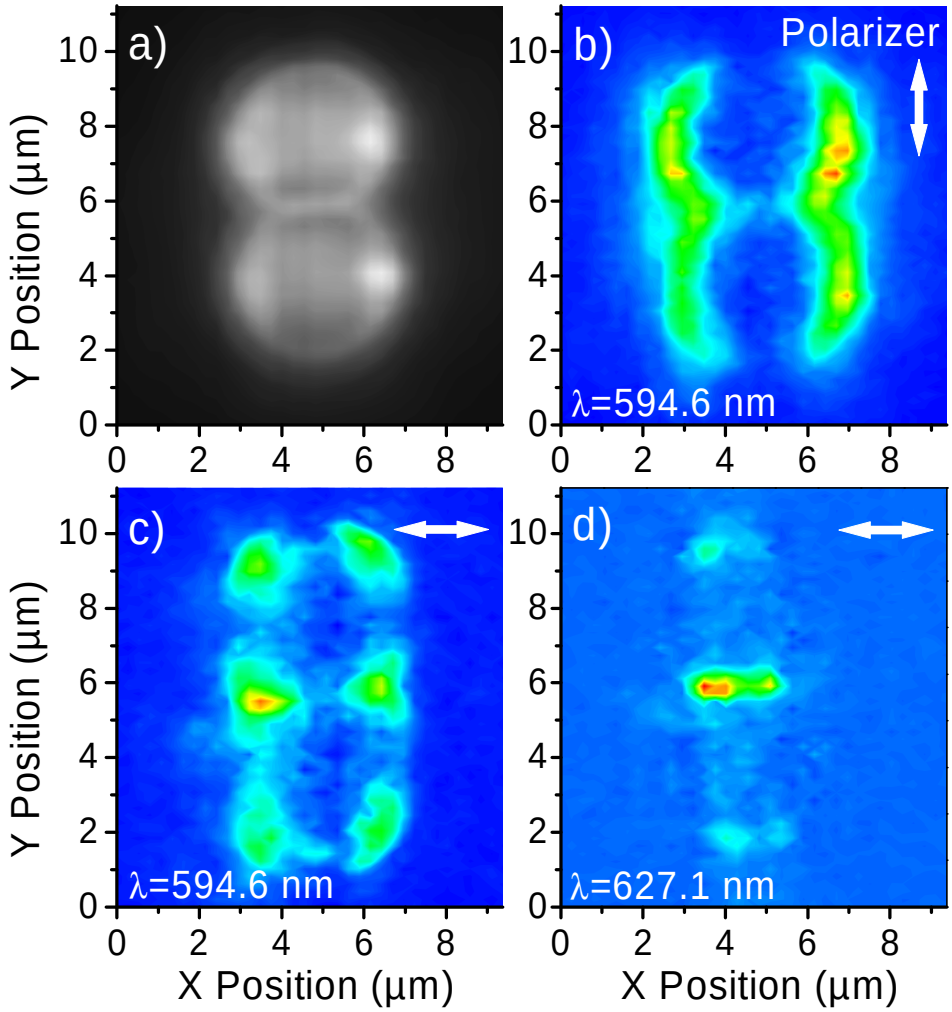

Figure 4.8: Polarization-sensitive intensity maps of a bisphere photonic molecule with touching constituents. Diagram (a) shows the spectrally integrated intensity distribution for comparison. In (b) the intensity map resonant to a weakly coupled TE^{19} resonance is plotted. The polarizer is aligned along the main axis (see arrow). The corresponding mode map for the perpendicular orientation is shown in image (c). In (c), the intensity pattern of a strongly coupled TE_{18}-resonance is shown for the polarizer orientation like in (d) (s. arrows).

contributions by changing the orientation of the linear polarizer in the detection beam path. We find that in a linearly aligned sphere geometry the single-sphere polarization character of the discrete photon modes survives to a major extent. The color-coded maps show the polarization-sensitively detected spatial intensity distributions in resonance to a weakly coupled [fig. 4.8 (b) and 4.8 (c)] and a strongly coupled, bonding TE-like mode mode [fig. 4.8 (d)]. In case of the weakly coupled modes, the detected signal is almost vanishing along the bisphere axis, indicating a weak cavity field at these regions originating from intersphere coupling. The intensity map for the strongly coupled mode, on the other hand, (here spectrally shifted by 5 nm, see fig. 4.5) exhibits the inverse intensity distribution compared to fig. 4.8 (c), showing a signal only at those positions where the

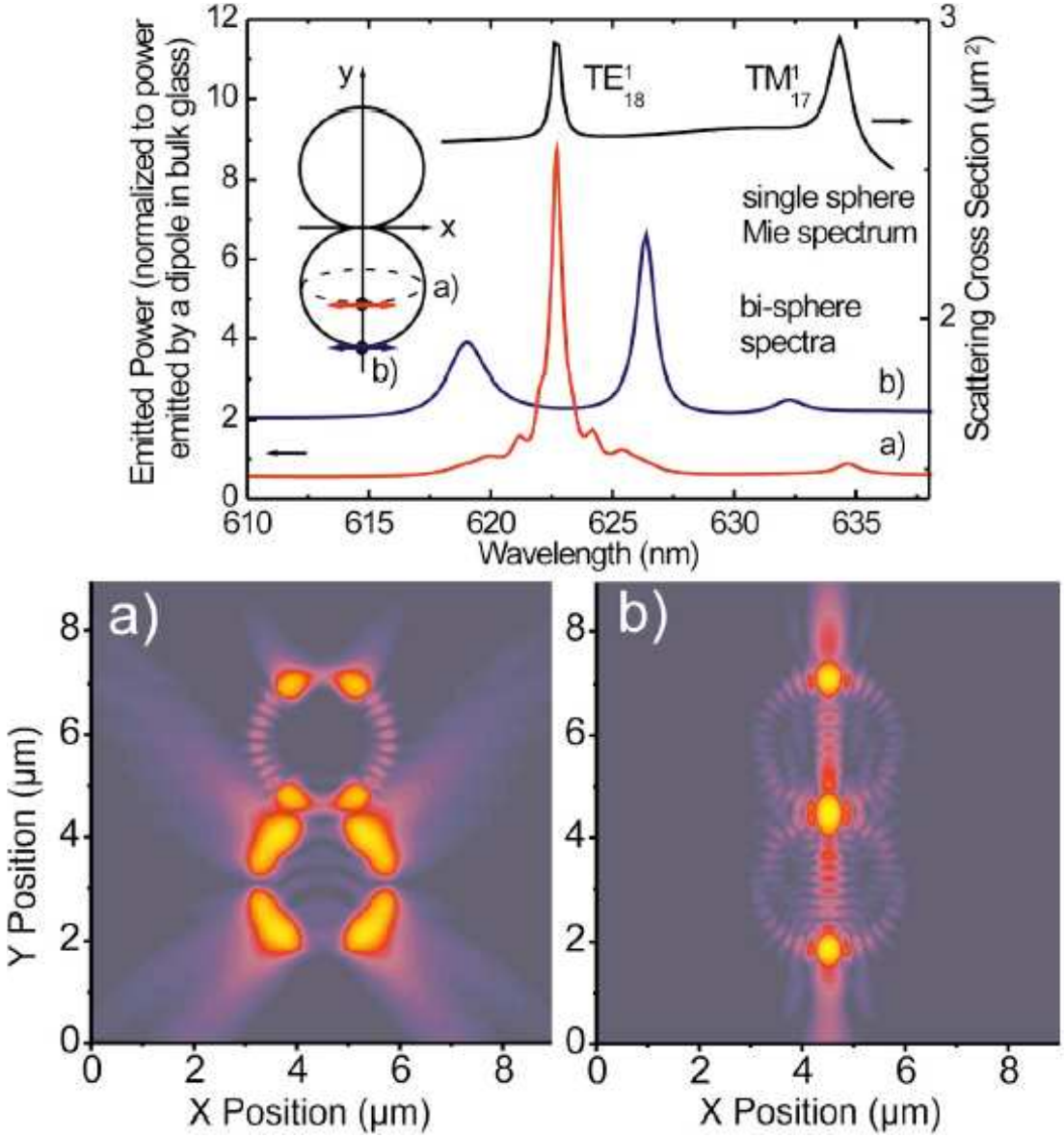

Figure 4.9: Emission spectra (offset) and electric field distributions in a photonic molecule calculated with the multiple multipole method (MMP) for horizontally aligned dipoles in a distance of 1.2 μm from the sphere center, located (a) on the equator position (see inset), and (b) on the bisphere axis. The field distributions show $|E|^2$ in a logarithmic scale covering 40 dB, taken from ref. [Möl04].

weakly coupled modes have no intensity. By comparing to fig. 4.5 we see that the corresponding spectra show no significant broadening in case of the weakly coupled modes of figs. 4.8 (b) and 4.8 (c) and significantly split-off, spectrally broader peaks for the strongly coupled mode of fig. 4.8 (d).

In order to understand the influence of coherent photon coupling on the cavity field distribution and mode line shape, a comparative calculation of a bisphere system has been performed using the semianalytical multiple multipole (MMP) technique with systematic variation of dipole position, frequency, and orientation by Priv.-Doz. R. Wannemacher

(Leipzig) [Wan04b]. The field distribution and spectra are displayed in fig. 4.9 for bisphere parameters of $R = 1.3895$ μm radius and refractive index $n = 1.58876$. Here, a *single* dipole emitter is modeled, aligned in x-direction and located (a) at $r = 1.2$ μm from the center of the lower microsphere at the equator and (b) on the bisphere axis (see scheme in the inset of fig. 4.9). The calculation for the bisphere system identifies the measured vanishing field intensity along the bisphere axis as a real, spatial, single-mode modification in a weakly coupled bisphere system without a significant spectral mode shift and broadening [fig. 4.9, case (a), marked in red] compared to the single-sphere spectrum. Likewise, also theory shows for the strongly bonding modes a significant increase in linewidth due to the additional loss mechanism caused by the strong intersphere coupling and a concentration of the electric field intensity along the bisphere axis [fig. 4.9, case (b), marked in blue]. As can be seen from figs. 4.5, 4.8 and 4.9, the experimental mode mapping for weakly coupled (off-axis points) and strongly coupled (on-axis points) mode pictures reveal identical characteristics with the calculated electromagnetic field intensity $|E|^2$ for tangential dipole orientation. The calculated spectra confirm the observation of coherent cavity coupling for resonant modes in exactly size-matched microcavities. Hence, the Q-factor conservation for weakly coupled modes, strong mode splitting for the strongly coupled modes, and complementary modifications of the field intensity along the bisphere axis for both mode types are a clear signature for coherent cavity coupling, reflecting the spatial symmetry of the configuration.

Furthermore, the coherent coupling of microresonators might be utilized in the frame of quantum computing, as will be discussed more detailed in section 6.6. Currently, the possibility of using coupled microcavities for quantum information processing is met with growing interest [Bos04, Li04]. To illustrate this, let us consider a coupled mode extended over two microspheres. While entangled states are often discussed for two-particle systems, they can be realized with single quantum systems, e.g. a photon, only (see, for example, [Lee00]). In our case, a single photon in a coherently coupled mode among two cavities can be regarded as a superposition state [Bar03]:

$$\frac{1}{\sqrt{2}} \left(|1>_{\text{Cavity 1}} |0>_{\text{Cavity 2}} + |0>_{\text{Cavity 1}} |1>_{\text{Cavity 2}} \right) \ . \tag{4.1}$$

As will be discussed later, such a superposition state could also be impregnated into a chain of coupled microcavities, where the superposition states can be subsequently transferred to the other end, which will lead us to the proposal of coupled cavities as an entanglement transfer line.

4.0.4 Linear Chain Geometries of Coupled Microsphere Cavities

The study of linear structures with more than two coupled cavities is motivated by the interest in waveguiding through weak coupling between high-Q optical cavities (the so-called CROW structure: coupled-resonator optical waveguide) [Yar99]. This type of waveguiding might replace waveguiding by total internal reflection and waveguiding through Bragg

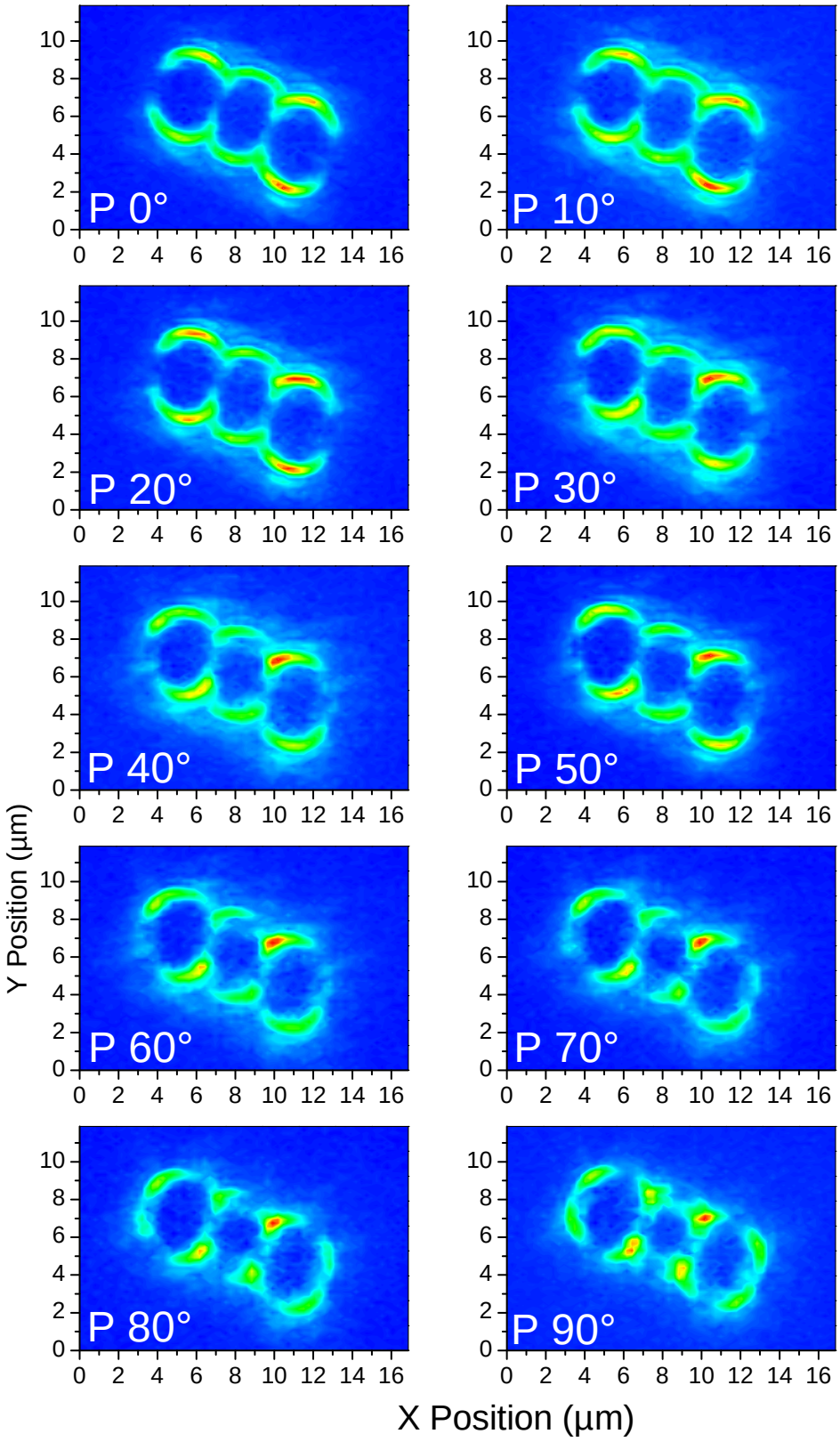

Figure 4.10: Polarization-sensitive mode maps of a linear three-sphere structure with touching constituents. The TE^{1}_{19} mode intensity at $\lambda = 591.8$ nm is shown, while the analyzer in the detection beam path is rotated stepwise from parallel to perpendicular direction with respect to the three-sphere axis.

reflection from a periodic structure. A particularly appealing feature of the CROW is the possibility of lossless and reflectionless bends. The experimental realization has been proposed using polar geometries, such as microdisks or microspheres. Hence, we discuss in the following the coherent coupling in a linear three-resonator configuration without significant Q-factor degrading.

A class of polarization-sensitively detected spectra taken at characteristic detection points in a linear three-sphere geometry is shown in fig. 4.11. At positions at the individual microsphere rims far off the three-sphere axis (indicated in the lower image of fig. 4.11), the mode energies agree closely with the theoretically predicted mode resonances of a single sphere. For the detection of the cavity modes at the axis points, the spectra show — similarly to the bisphere system — a splitting of the modes into red- and blue-shifted modes. Since the number of strongly split modes does not obviously increase, we are faced with the question, whether all cavities participate in a coherent mode evolution or only pairwise coupling between two neighboring spheres occurs.

In order to clarify a coherent mode evolution along the three-sphere line, we first perform a similar analysis of the mode intensity of the weakly coupled TE modes in the three-sphere geometry. The results are displayed in fig. 4.10, where the polarizer orientation has been varied in steps of 10 degrees, starting with a polarizer orientation parallel to the dimension of the sphere alignment towards the perpendicular orientation. As can bee seen in fig. 4.10, a similar turn of the detected intensity is found, in particular, the weakly coupled modes display an almost vanishing mode intensity at all on-axis points of the three-sphere axis. This behavior we already identified as a characteristic feature for bisphere systems. Thereby, we conclude, that the condition of coherent three-sphere coupling holds as well for this geometry. In order to complete the picture, we compare in the following the obtained intensity images with those of the strongly coupled modes in this geometry. As can be observed in fig. 4.12, the mode images of the strongly coupled modes show even in the case of three coupled microresonators a complementary behavior: The strongly coupled red-shifted bonding modes display their maximum intensity at the boundary locations matching the three-sphere axis. Thus, this trend of the different light localization of strongly coupled modes and weakly coupled modes with respect to the axis in one-dimensional systems can be introduced as a suitable criterion for coherent intersphere coupling. We already note here, that a third criterion concerning the number of split modes and variation of oscillator strengths in adjacent resonators will be established in the later sections, in which we develop a theoretical approach for the weakly coupled modes. As will turn out, in finite structures a mode splitting with even less peaks per sphere than the number of resonators in a chain is observed, although all resonators participate in the coherent mode evolution. The more intuitive expectation of n peaks per sphere in a chain of n coupled resonators is demonstrated to be invalid, since the finiteness of a free CROW (e.g., no periodic boundary conditions can be applied) breaks the translational symmetry of the Bloch modes, leading to varying oscillator strengths in adjacent resonators.

As we note from fig. 4.12, a linear chain consisting of three touching spheres shows exactly the characteristics found before in the bisphere system: Weakly coupled TE-type modes have vanishing intensity along the trisphere axis while strongly coupled TE bonding modes exhibit strongest emission at touching points and split in red- and blueshifted modes (spectra not shown here). For the weakly coupled modes (off-axis positions), no significant change in the Q-factor ($Q \approx 1000$) is measured for either the bisphere or the linear three-sphere configuration, which is a promising result with respect to future application in weakly coupled, high-Q CROW-structures.

4.0.5 Two-dimensional Geometries of Coupled Microsphere Cavities

Next, we study the effect of next-neighbor and long-distance coupling by analyzing several two-dimensional sphere geometries. We focus on the stability of the photonic molecule formation while continuously including further constituents. This procedure can be considered as a bottom-up approach to a two-dimensional photonic structure and results in symmetrical three- and four-sphere geometries. Fig. 4.13 shows the spatially resolved emission intensity of a molecule state for two 2D-sphere configurations. As the main difference with respect to one-dimensional, linear chain geometries, a redistribution of field intensity within the array towards the air gaps is observed. As shown in fig. 4.13, the strongest emission is detected close to the air-gap positions and not at the intersection points — in contrast to the strongly coupled resonances in linear three-sphere geometries discussed in the preceding subsections. This strong intensity localization at positions apart from the intersection points is only observed for geometries which deviate from the linear chain. An explanation of the pronounced intensity patterns at the air-gap positions in the multisphere configurations of fig. 4.13 requires the assumption of coherent three-sphere coupling: An argument for a complete coherent three-sphere coupling is the fact, that an incoherent intensity sum would never vanish at the intersection points. The addition of a fourth sphere does not significantly modify the spatial confinement at the center of the molecule. These findings strongly support the term tight-binding coupling in which next-neighbor species have necessarily to be all included in the molecule formation, but distant objects have negligible effects. This fact, combined with the spectral features, highlights the feasibility of this *photonic chemistry* approach for new cavity designs.

The strong field intensity modification for molecules is evaluated more quantitatively by integrating the mapped intensity patterns in agglomerates and comparing it with the single-sphere case. We discuss now the interesting case of weak coupling because the spatial modification of the emission intensity here is not accompanied with a large spectral broadening. The measured intensity distribution is integrated for maps of such weakly coupled modes taken at identical excitation and detection conditions for the same TE-type resonance. For off-axis positions Q-values of 1200, 920, and 1000 are measured for the single-sphere, bisphere and 2D trisphere geometry, respectively. For the latter

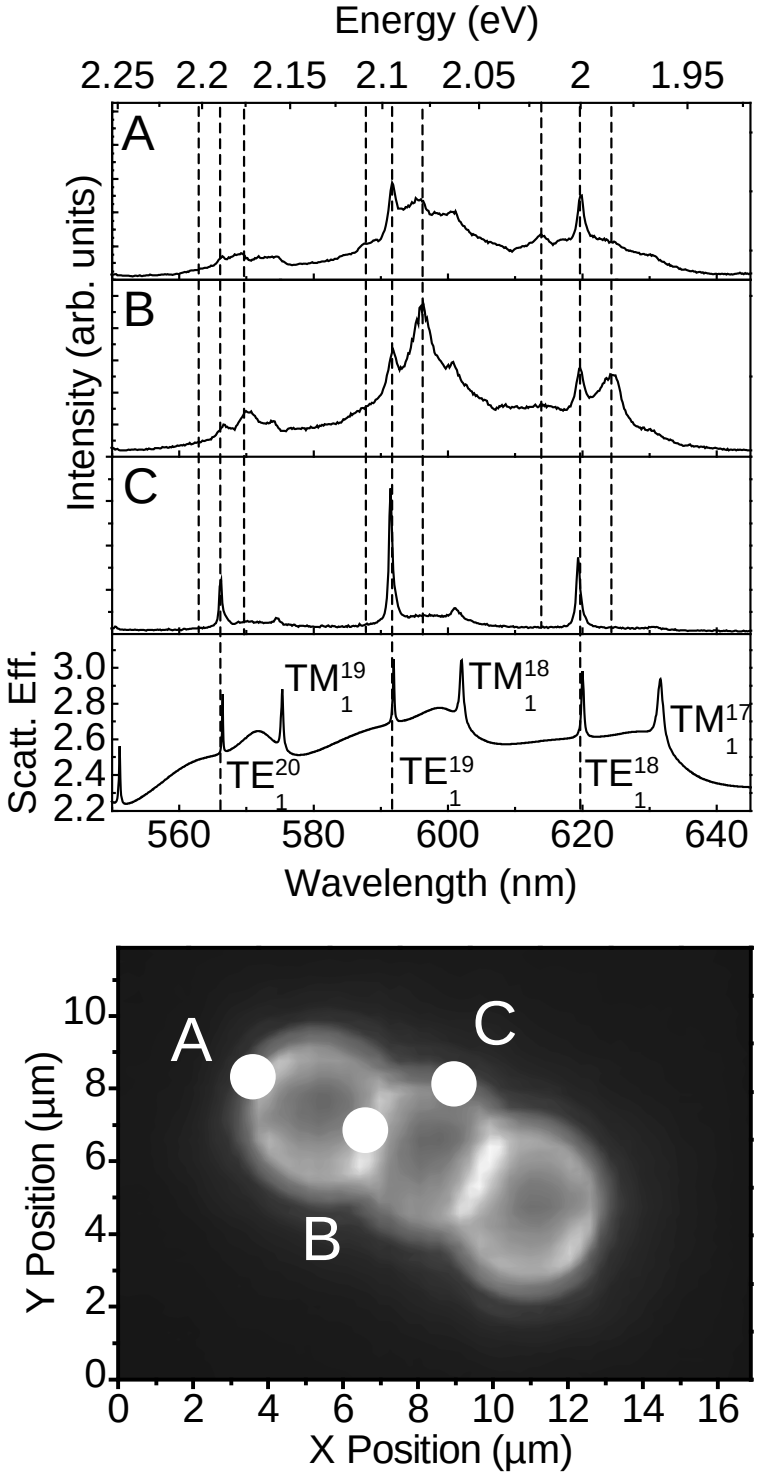

Figure 4.11: Three-sphere emission spectra taken at characteristic detection points (see image). The spectra show the features of weakly and strongly coupled modes in a similar manner as observed for the bisphere configuration. All spectra are taken in TE-sensitive detection. For comparison and determination of the corresponding mode numbers, a calculation of the single-sphere scattering efficiency is plotted in the bottom curve.

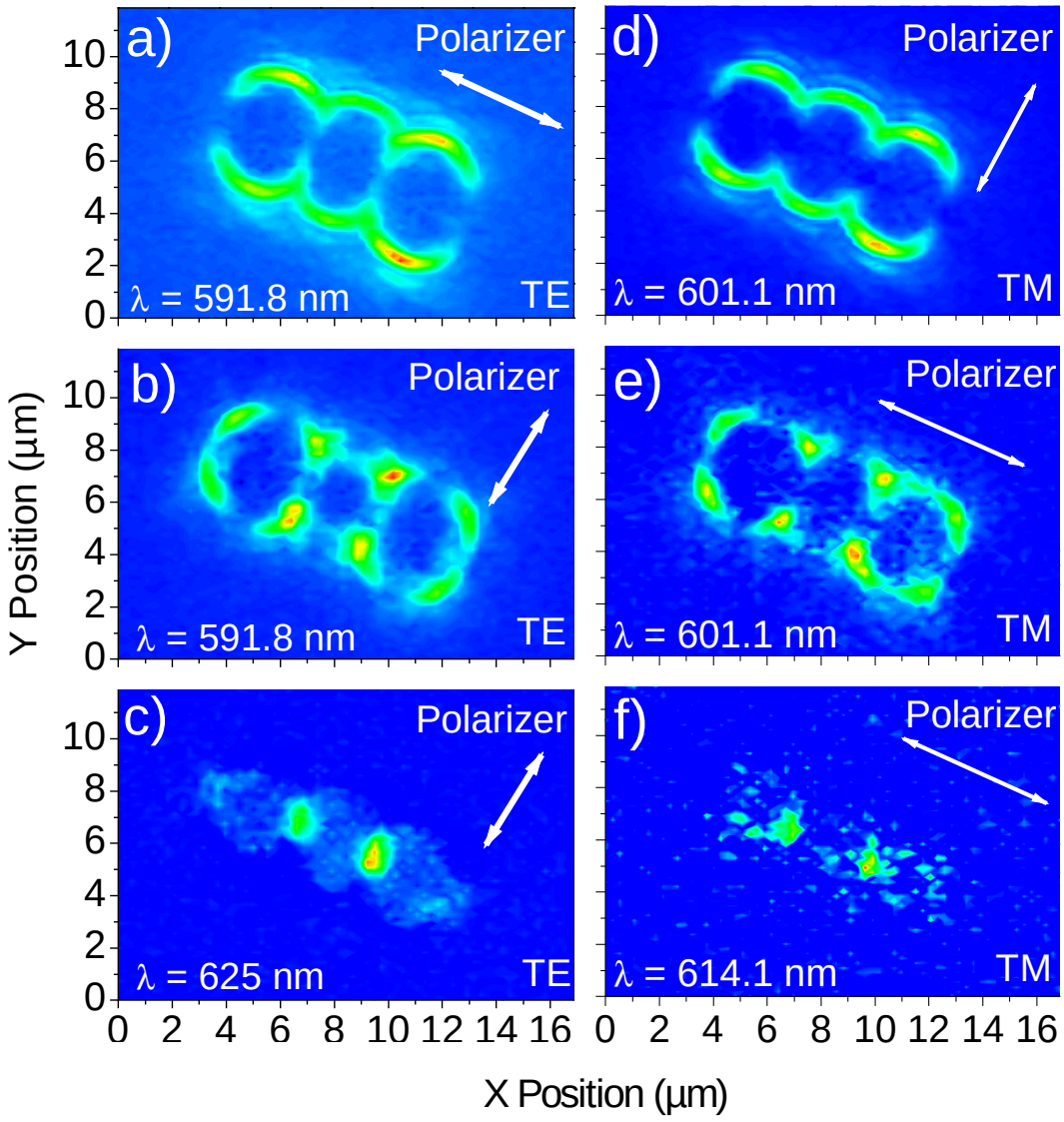

Figure 4.12: Polarization-sensitive mode maps of weakly and strongly coupled TE modes (a-c) and TM modes (d-f). The wavelengths are given in the diagrams and the polarizer orientations are marked by arrows.

configuration, the spectra at three symmetry-relevant positions are shown in fig. 4.14, with the sharpest mode observed at the detection point C. The experimentally determined integrated mapped intensities normalized to the single-sphere case are V_{integr} from 1 (single sphere) to 1.42 (bisphere) and 1.66 (2D trisphere).

4.0.6 Summary

In conclusion, the photonic molecule formation in one- and two-dimensionally coupled exactly size-matched microspheres is demonstrated and the spatial dependence and polarization type of both the weakly coupled and strongly coupled resonances have been studied. The comparison of different molecule geometries clearly shows a tight-binding

coupling signature of the bonding photon states. The interference effects of the weakly coupled modes might be used to build a new type of structured cavity with easily modified light concentration in highly tunable systems. Both experiment and theory show that weak coupling, e.g., of three coupled resonators, with no significant loss in the Q-factor can be achieved as well as strong coupling with strong field concentration along the molecule axes. Since the dominating polarization type survives to a large extent, an additional control of photons via alignment of nanorods, as demonstrated for single microspheres in chapter 3, might be feasible.

The similarity of the spectral and spatial features apparent in the linear two- and three-sphere geometries, although apparently giving a compact description of linear coupled cavity structures, will be investigated in more details in the next sections. First, we address the issue, whether additional coupled resonances are apparent in the spectra for a coherently coupled three-sphere system compared to a bisphere system. Additionally, differences in the individual oscillator strengths in systems with more than two coupled resonators will be explored. This provides us with additional experimental criteria for the formation of extended multiresonator photon states and an comprehensive understanding of the mode formation via an harmonic oscillator analogy.

However, for strongly coupled modes in linear geometries detected at the resonator intersection points, additional intermixing of modes with higher radial order is likely to occur due to the changes in the boundary conditions compared to single microspheres. Thereby, these broadened coupled modes prevent us from the direct observation of a possible band structure formation, for which additional splittings might be hidden, and do not exhibit ideal parameters for waveguiding mechanisms. Here, low loss modes are favored and the splitting due to interresonator coupling is desired to be kept as small as possible. Hence, the weakly coupled modes are most promising for these approaches. As we will see in the next section, modifications of the group velocity of light is one inspiring property, which obeys a reciprocal relation with the coupling constant.

4.1 Periodic Structures — Coupled-Resonator Optical Waveguides (CROWs)

Since we will deal in the following with the CROW mode evolution both experimentally and theoretically, a brief description of the formalism is given below.

In 1999, the possibility to construct optical waveguides built from resonators exhibiting whispering-gallery like mode structures was noticed by Amnon Yariv [Yar99]. This proposal suggests a way to transfer energy via weakly coupled resonator fields and thus to bend light around angles on the micrometer scale according to the whispering-gallery mode symmetries. Furthermore, it might be feasible to modify the dispersion relation of the coherently coupled light-fields involved. This proposal is inspired by the tight-binding

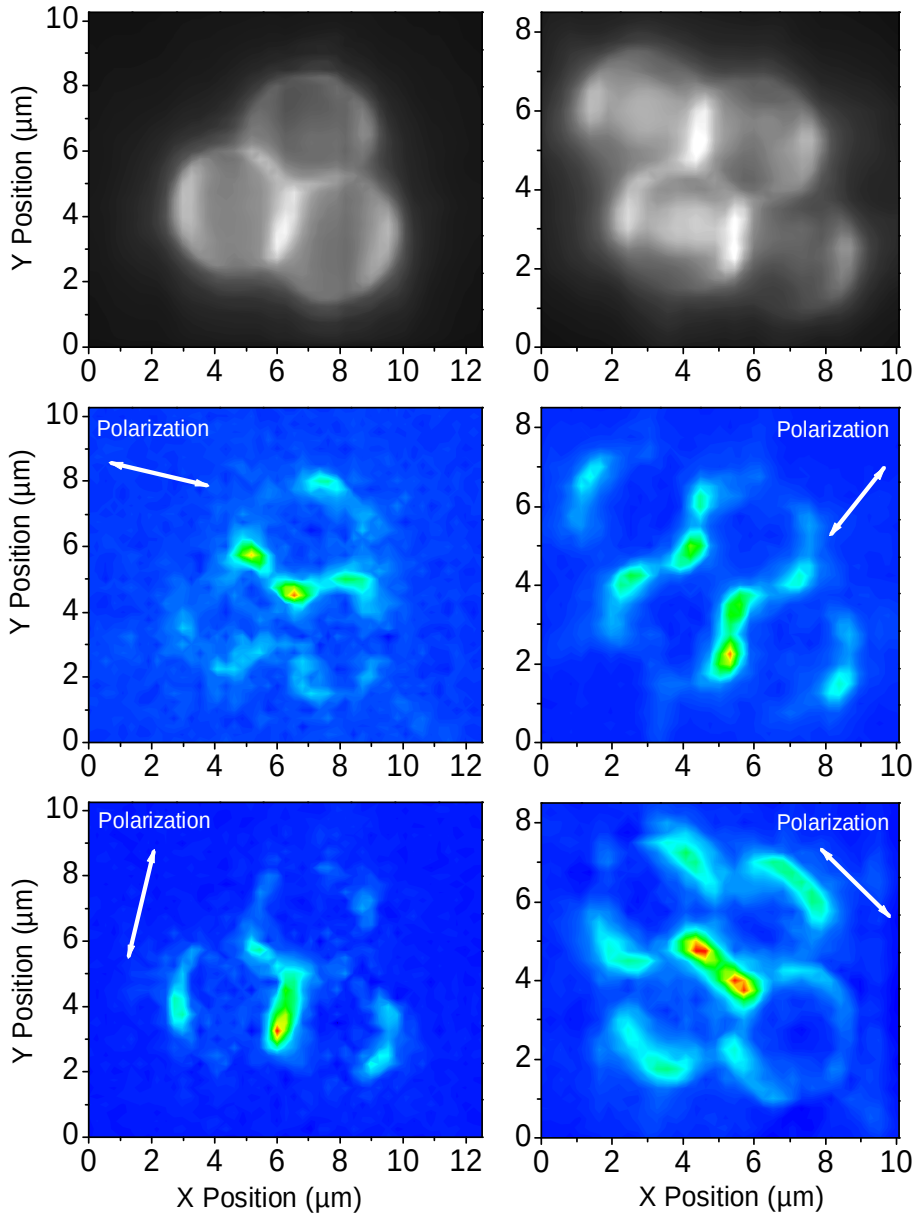

Figure 4.13: Polarization-sensitive intensity characteristics of strongly coupled bonding resonances of TE character in two-dimensional triple (left) and quadruple (right) sphere configurations. The geometry of the structures is shown in the first row, which displays the spectrally integrated intensity distribution. The other images show the intensity distributions for different orthogonal polarizer orientations as indicated by arrows.

approach commonly used in solid state physics and gained a lot of interest especially from the side of theory and simulation, covering ways to slow down the group velocity of light by orders of magnitude [Khu05], and to even time-reverse optical signals [Yan04a] which could lead to enhanced performance of possible devices for all-optical networks and highly sensitive biosensors [Alt05b].

This structure is commonly referred to as a coupled-resonator optical waveguide (CROW) and a brief derivation following Yariv's proposal of the dispersion relation will be given

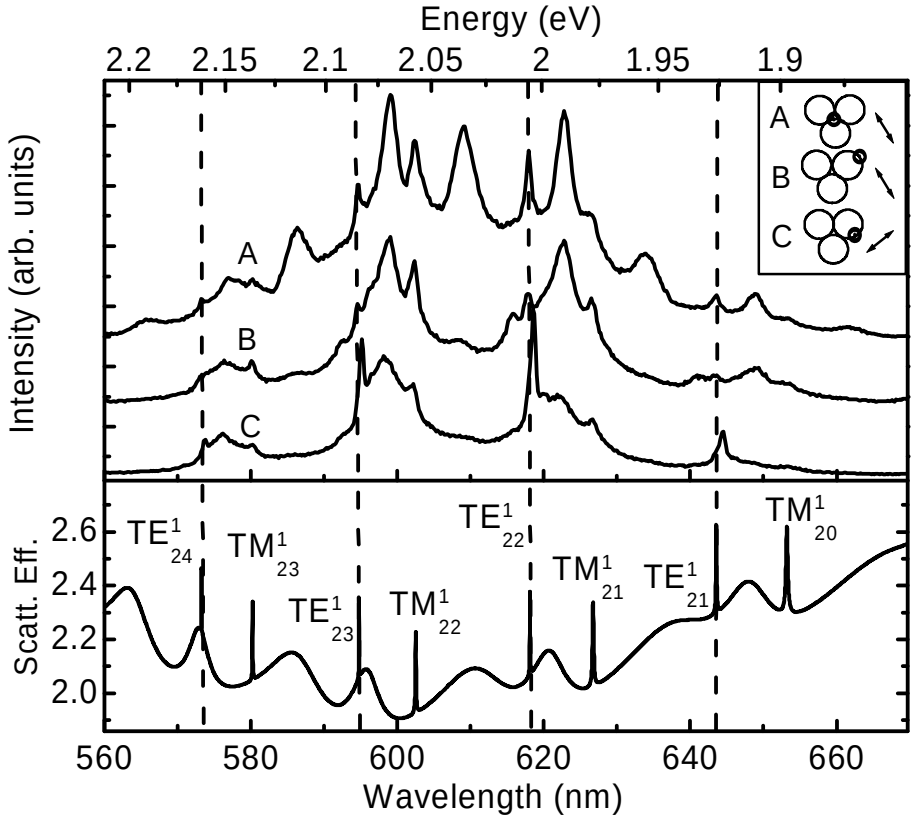

Figure 4.14: Emission spectra taken at different symmetry relevant detection points in a two-dimensional three-sphere system for adjusted polarizer orientations (see inset). Like in the linear bisphere and three-sphere case, the evolution of the single microsphere modes into collective bonding and antibonding modes is apparent. Both TM and TE modes are visible in the spectra, because of the threefold symmetry of the structure.

below. Let me point out here already, that the proposed structure leads to relations which are mathematically identical to a simple model of coupled oscillators, as I will demonstrate later on in this section. Via this analogy, we can estimate the important properties of more complicated structures even for cases, in which exact numerical field calculations would become overwhelmingly difficult.

We consider a row of whispering-gallery mode resonators with the field modes $\mathbf{E}_\Omega(\mathbf{r})$ and an individual eigenfrequency Ω linearly aligned at positions $z = n \cdot R$. A scheme of a coupled-resonator optical waveguide is depicted in fig. 4.15. The CROW mode is then considered to be a linear superposition of the single resonator modes

$$\mathbf{E}_K^{\mathrm{CROW}}(\mathbf{r}, t) = E_0 \exp(i\omega_K t) \sum_n \exp(-inKR) \cdot \mathbf{E}_\Omega^{\mathrm{CROW}}(\mathbf{r} - nR\mathbf{e}_z) \tag{4.2}$$

and represents a photonic Bloch function with the wave vector $K \in \left[-\frac{\pi}{R} \ldots \frac{\pi}{R}\right[$. The field modes of the entire structure must solve Maxwell's equations

$$\nabla \times (\nabla \times \mathbf{E}_K^{\mathrm{CROW}}) = \epsilon(\mathbf{r}) \frac{\omega_K^2}{c^2} \mathbf{E}_K^{\mathrm{CROW}} \tag{4.3}$$

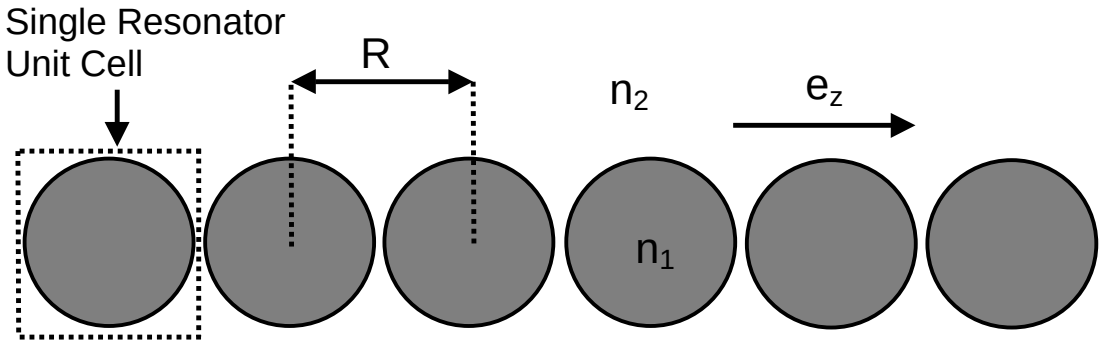

Figure 4.15: Schematic representation of a coupled-resonator optical waveguide (CROW). The individual resonators are assumed to be degenerate in their individual eigenfrequencies. The optical fields of the resonators are coupled through their evanescent field components and constitute Bloch wave functions (after [Yar99]).

for the eigenfrequency ω_K, $\epsilon(\mathbf{r})$ being the dielectric constant for the whole CROW structure.

An expression for the frequency can be obtained via multiplication of the wave equation from the left with the single resonator field E_Ω and subsequent integration over the whole space. This integration can be greatly simplified by assuming the limit of tight-binding coupling, so that the overlap integrals of resonators can be neglected for all but next neighbors, i.e.

$$\alpha_n = \int \mathrm{d}^3\mathbf{r}\epsilon(\mathbf{r})\mathbf{E}_\Omega(\mathbf{r}) \cdot \mathbf{E}_\Omega(\mathbf{r} - nR\mathbf{e}_z), \qquad n \neq 0, \tag{4.4}$$

$$\beta_n = \int \mathrm{d}^3\mathbf{r}\epsilon_0(\mathbf{r} - nR\mathbf{e}_z)\mathbf{E}_\Omega(\mathbf{r}) \cdot \mathbf{E}_\Omega(\mathbf{r} - nR\mathbf{e}_z), \qquad n \neq 0, \tag{4.5}$$

can be treated as zero for $n \neq 0, \pm 1$. Additionally, the coupling of next neighbors expressed in the coupling constant κ_1 can be treated as comparatively weak, i.e.

$$\kappa_1 = \beta_1 - \alpha_1 = \int \mathrm{d}^3\mathbf{r}\left[\epsilon_0(\mathbf{r} - R\mathbf{e}_z) - \epsilon(\mathbf{r} - R\mathbf{e}_z)\right] \times \mathbf{E}_\Omega(\mathbf{r}) \cdot \mathbf{E}_\Omega(\mathbf{r} - R\mathbf{e}_z) \tag{4.6}$$

is a small quantity $\kappa_1 \ll 1$. If we additionally take the resonator field to be concentrated to a large extend inside the resonators, e.g.

$$\Delta\alpha = \int \mathrm{d}^3\mathbf{r}\left[\epsilon(\mathbf{r}) - \epsilon_0(\mathbf{r})\right]\mathbf{E}_\Omega(\mathbf{r}) \tag{4.7}$$

with $\Delta\alpha \ll 1$ as well, the frequency dispersion reads

$$\omega_K = \Omega\left[1 - \frac{\Delta\alpha}{2} + \kappa_1 \cos(KR)\right] \tag{4.8}$$

and the group velocity dispersion is readily obtained

$$v_g(K) = \frac{\partial\omega_K}{\partial K} = -\Omega R\kappa_1 \sin(KR)\ . \tag{4.9}$$

Thus, dependent on the choice of frequency, one ends up with a huge variation of the group velocity, which could be used for buffering of optical signals by delaying the propagation of a signal track.

Hereby, we can formulate the essential key features for any successful realization of CROW structures: First, the one-dimensional waveguide-like structures must consist of sufficiently equal-sized microresonators. Second, the light fields of the microcavities must be shown to exhibit coherent intercavity coupling and third, additional modes should be observed, corresponding to the formation of extended modes due to multisphere coupling in accordance to Bloch's theorem. The aim of the next section is to demonstrate these key features for microspheres aligned in one-dimensional rows.

5. Extended Photonic Molecule Chains

In this chapter, linearly assembled microsphere resonators doped with semiconductor quantum dots are explored as building blocks for *coupled-resonator optical waveguides**. The evolution of single cavity modes into collective waveguide modes is studied using polarization-sensitive microphotoluminescence spectroscopy. The formation of coupled-resonator waveguide modes is demonstrated, using vertex-shaped resonator arrays for the experimental proof of coherently coupled multisphere photon states as an experimental method.

As an introduction to the samples under consideration, a white-light microscope image of the bent coupled-resonator structure is given in fig. 5.1, for comparison, a spectrally integrated photoluminescence image is given below.

Since microresonators with circular geometrical cross sections of a few optical wavelengths such as microdisks or microspheres (which we deal with here) confine the light in whispering-gallery-like modes, these cavities have been proposed as flexible building blocks for CROWs [Yar99, Ste98, Smi04a, Ast04].

As already mentioned previously, waveguiding in CROW structures is realized by *weak* coupling of single cavity photon fields, analogous to the tight-binding description of electronic states in solids. Possible applications of CROW structures are currently discussed concerning almost loss-less propagation and reflectionless bending of light, slowing down its group velocity, as model systems for all-optical phenomena such as *coupled-resonator induced transparency* (CRIT) [Smi04a], and time reversal of light [Yan04a]. Currently, many theoretical efforts are devoted to the design of CROW structures [Poo04b]. An experimental realization utilizing circular microcavities, however, has been less studied. Thus, polymeric microspheres doped with semiconductor nanocrystals are studied here as building blocks for CROW structures. Microspheres appear to be a flexible choice, since their isotropic shape intrinsically opens the way towards even three-dimensional waveguide applications.

Polystyrene microspheres with radii of about $R \approx 2.25$ μm and a refractive index 1.59 are subsurface impregnated with CdSe nanocrystals of Radius $R_{\mathrm{NC}} = 2.5$ nm according to the method described in chapter 3. After synthesis of CdSe nanocrystals following subsection 2.4.1, the methanolic suspension of microspheres was cast and dried on a quartz substrate in the vicinity of a removable microtemplate, leading to linear and vertex-shaped chains

*Parts of the content in this chapter have been published previously as an article:
Opt. Lett. **30** (16), 2116 (2005), ©2005 Optical Society of America, ref. [Möl05b]

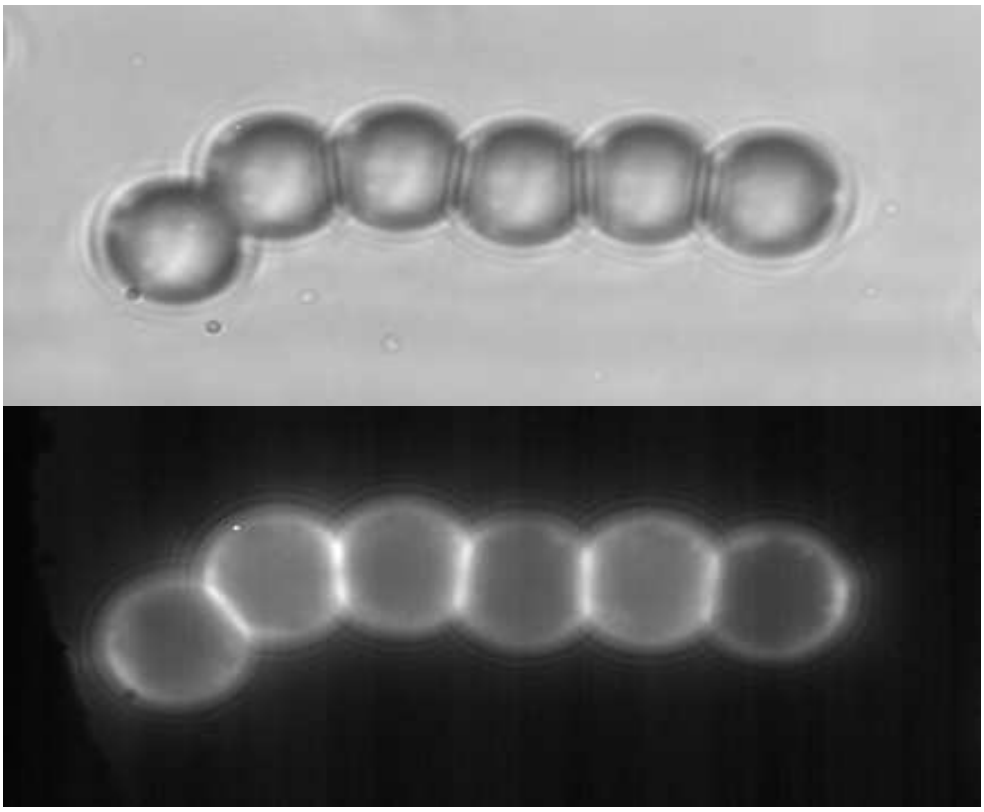

Figure 5.1: White-light microscope image of a nanocrystal doped bent CROW structure forming a vertex of about 30 degrees (the individual spheres 2.25 μm in radius). The upper image shows the structure illuminated with white light, the lower diagram displays the dopant luminescence excited via laser excitation (filtered).

of touching microspheres. The slightly larger size of the microspheres utilized here allows for a reproducible alignment route as described below.

5.0.1 Preparation of Linear Microsphere Chains

The preparation of linear chains of microspheres requires an anisotropic modification of the synthesis described in subsection 4.0.2. This can be achieved by attaching a removable linear microtemplate onto the substrate before adding the methanolic microsphere suspension [Art03b]: The microtemplate used here is realized by a small glass rod with an outer diameter of 100 μm, that can be easily attached to the substrate without additional microfabrication techniques. The microsphere suspension is added around the template and forms a meniscus between the glass rod and substrate surfaces. During the drying process, the droplet shrinks and moves towards the meniscus due to capillary forces. With a suitable concentration of microspheres in the solution enough microspheres are carried within the shrinking droplet area. At a certain time, the liquid is nearly completely confined in the meniscus angle and not enough liquid is available at the outer rim to tow the microsphere ensemble further towards the touching point between the glass rod and

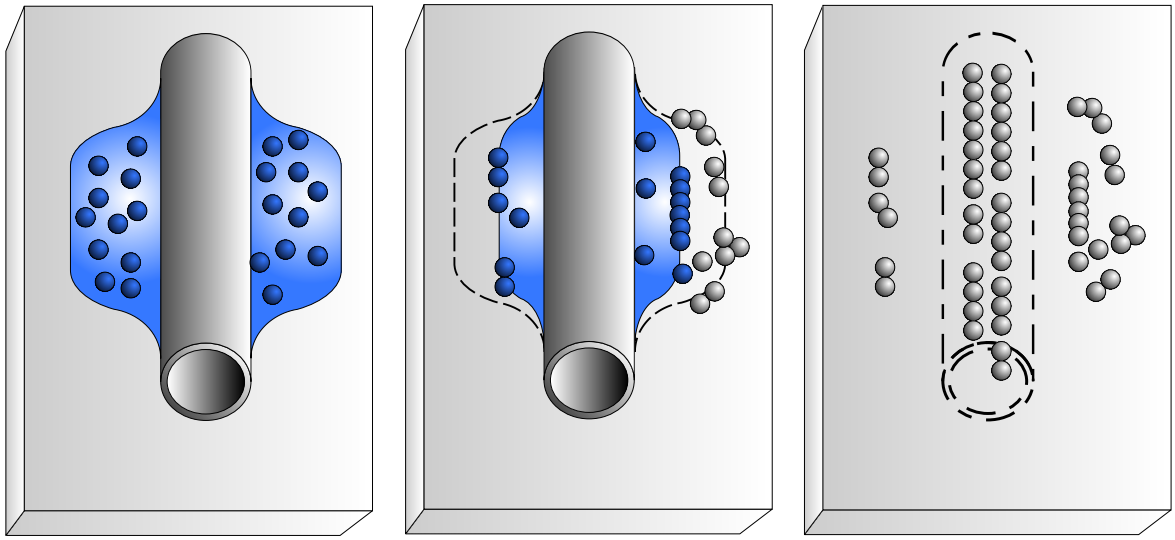

Figure 5.2: Schematic illustration of the preparation of linear microsphere arrays: First, a microcapillary is placed onto the quartz substrate. Subsequently, a droplet of the solution containing nanocrystal doped microspheres is applied onto the configuration (left image). During the evaporation of the solution, the droplet boundary moves towards the capillary (middle image). In the vicinity of the capillary, the droplet forms a meniscus between the capillary and the substrate. Further evaporation of the solution tows the microspheres towards the touching point of the capillary with the substrate. When the solution is almost dried, the microspheres can not be carried further towards the capillary and remain in highly ordered lines of about ten microspheres (right image).

the substrate. Thereby, the microspheres are left behind, ideally forming linear chains of touching microspheres. This way of preparation is illustrated in the cartoon 5.2.

Again, exactly size-matched microspheres with smallest variations of radii (< 0.1 %) have been preselected by their Mie resonances to guarantee efficient coherent resonator coupling. The study of coupled resonators, arranged in extended one-dimensional chains and arrays, covers resonators with radii around $R \approx 4\lambda$.

5.1 Coherent Coupling in Bent Microsphere Chains

We examine the following key features that inevitably are desired for any realization of CROWs: i) the coherent coupling (see chapter 4) of the individual resonator light fields, which requires exactly mode matched cavities and ii) the signature of *extended* photon states that evolves over more than two cavities opposed to an incoherent superposition of simply pairwisely coupled cavity fields. The coherence is shown by the modification of the nanocrystal emission at the intersection points of a CROW consisting of six microspheres. The extended multicavity coupling will be demonstrated both by the occurrence of additional splitting of the weakly coupled modes and by analyzing the spatial distribution of the mode intensities across a CROW which exhibits a vertex-like geometry. With this

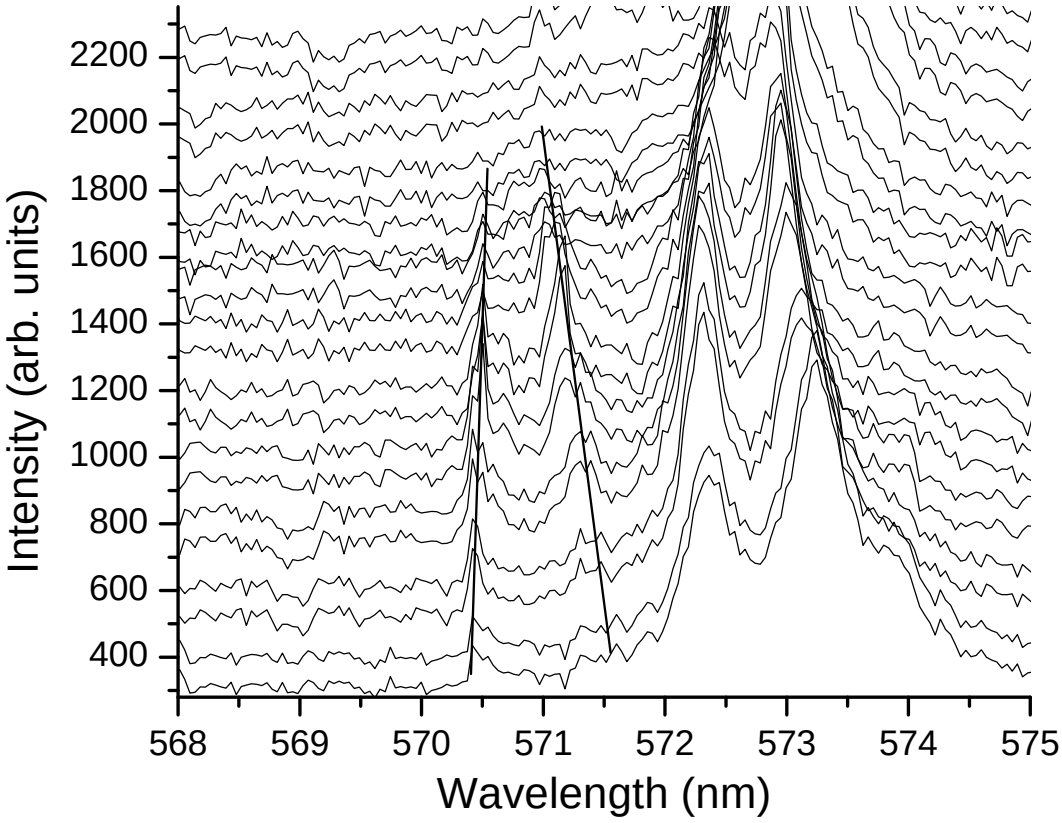

Figure 5.3: First order modes in the coupled-resonator chain with varying splits across the main axis. The intensity is significantly weaker compared to the pronounced mode emission of the second order modes.

experimental method, one can compare the results with the superposition of the vertex arms.

As in the case of photonic molecules, the evolution of single cavity modes into coherently coupled CROW modes is studied via microphotoluminescence spectroscopy at the diffraction limit combined with polarization-sensitive mode mapping (see section 4 and subsection 2.3.5). The spatial distribution and dominant polarization type of weakly and strongly coupled waveguide modes are studied spectrally resolved.

As apparent in the resulting spectra, not only modes with radial quantum number 1, but also modes with a radial number 2 display a locally varying mode splitting in the spectra. For demonstration, a spectral window with varying spectra along the CROW structure extension is shown in diagrams 5.3 and 5.4 for both radial mode types. Since both modes display a different light confinement condition for a single sphere, the occurrence of modes with differing radial quantum number could be utilized for realizing a set of different coupling constants for each mode type in one and the same coupled-resonator geometry. This could lead to a spectral tuning method in a single CROW structure. For this, larger spheres might be utilized, for which more pronounced modes enter the spectrum (see also section 2.1.1.)

In the discussion of the coupled modes in this section, we will focus on the modes with

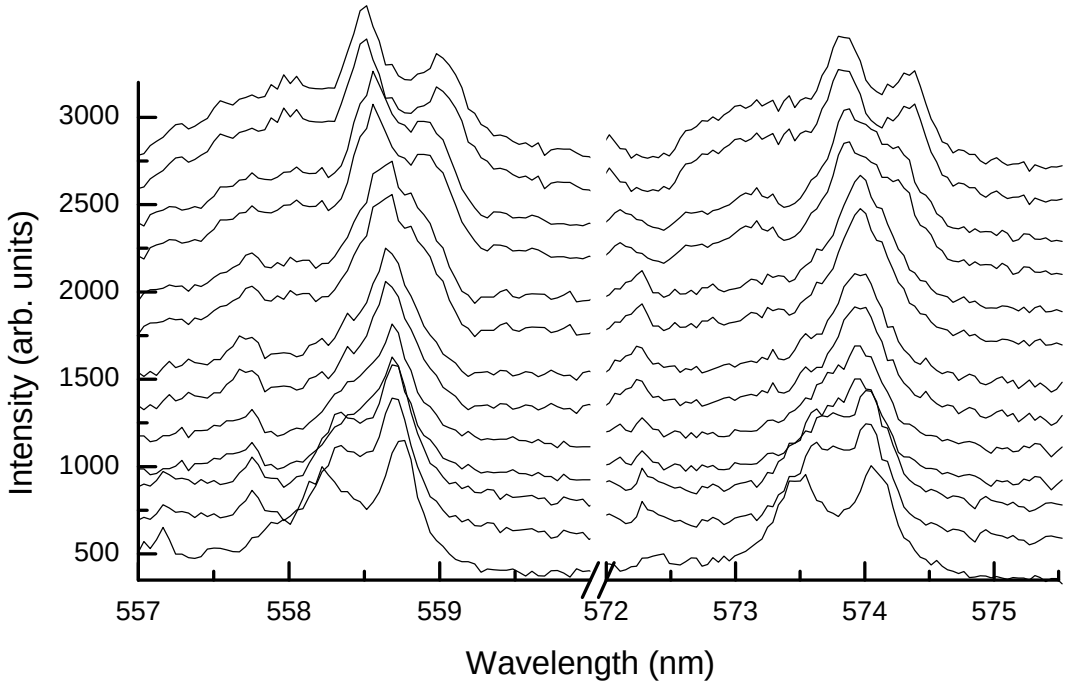

Figure 5.4: The most pronounced photoluminescence intensity is given by the second order modes with pronounced splits across the main axis. These modes are further analyzed by polarization-sensitive mode mapping.

radial number 2 due to their larger spectral width leading to more pronounced intensity patterns in the mode maps.

In fig. 5.5 we show characteristic spectra taken at specific detection points of a CROW structure forming an 30 degree vertex. For comparison, the calculated scattering spectrum for a single polymer sphere of radius 2.25 μm is displayed, too, giving the respective single sphere quantum numbers. In order to correctly identify the modes in the experimental spectra, only TE polarized modes are shown in the first two diagrams by applying the sensitive polarized detection scheme. Thus we can reduce the total mode spectrum into groups of either TE- or TM-like modes (see chapter 4). The curve in fig. 5.5 (a) displays a typical spectrum taken at an off-axis position on the left hand side of the chain (the used detection geometry is shown in the scheme in the insets). Here, the observed TE peaks are not accomplished with any spectral shift compared to the theoretical single sphere spectrum. Therefore, these modes are called *weakly* coupled CROW modes, which are of interest for possible CROW applications. In contrast, the spectrum 5.5 (b)), which is detected exactly at the on-axis points, shows a pronounced mode splitting into redshifted bonding and blueshifted antibonding modes, which are referred to as strongly coupled CROW modes here. A third set of spectra resulting from a narrow region slightly shifted apart from the on-axis points (see inset) are shown in fig. 5.5 (c)): These spectra show an additional and significantly smaller splitting of the modes, which is not apparent in coupled two-sphere systems and can therefore not be explained by a simple superposition of pairwisely coupled spheres. Of interest for the extended multisphere coupling are the

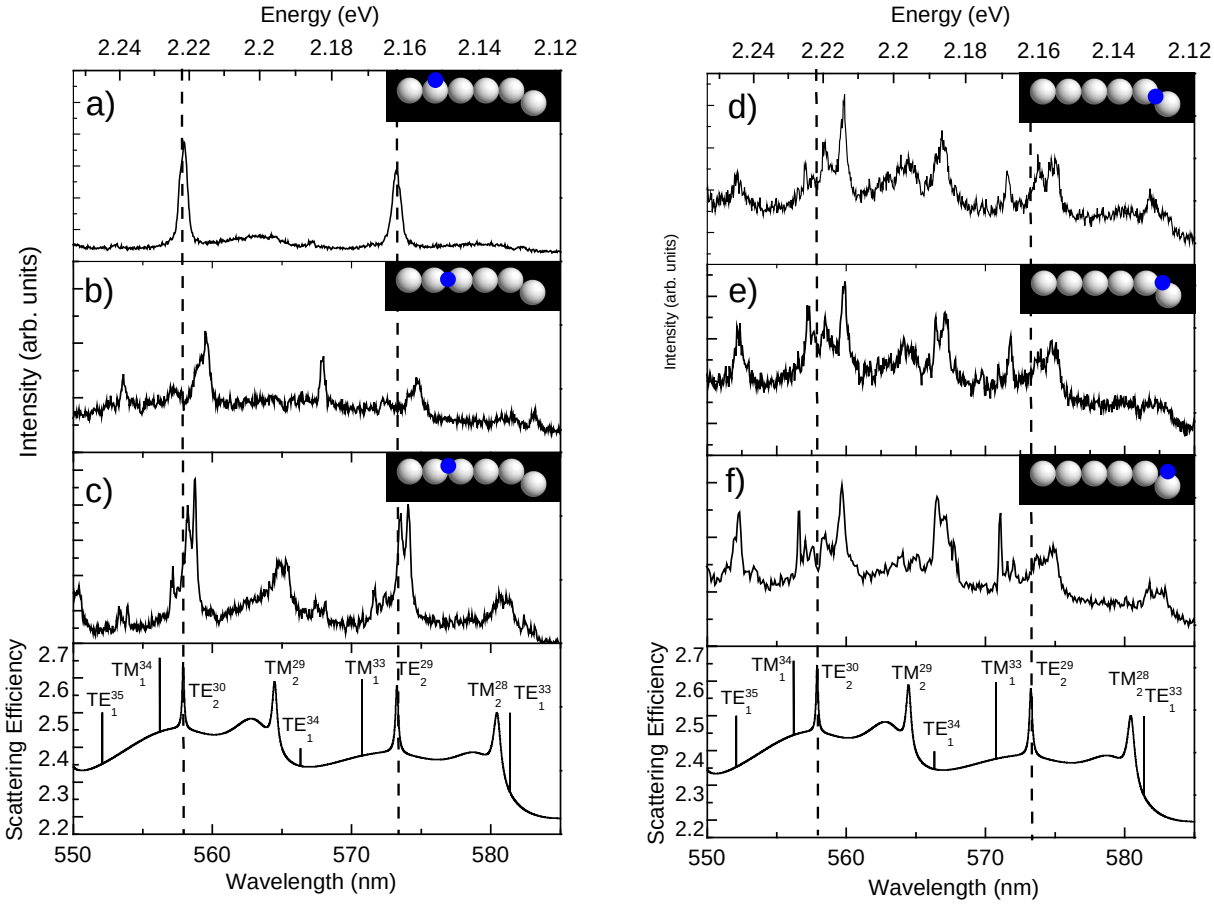

Figure 5.5: Spectra of a six-resonator CROW structure detected at selected spatial regions (see exemplary drawing in the insets): (a) Weakly coupled TE-polarized CROW modes detected at off-axis positions. (b) Strongly coupled CROW modes detected at on-axis positions, showing a pronounced mode splitting. (c) Fine splitting of modes detected slightly apart from the on-axis positions. (d),(e) Modes split in more than two peaks for detection on or close to the axis. (f) Spectra detected at an off-axis position like in (a). The bottom diagrams show the calculated scattering efficiency after eq. (2.14) of a single sphere. The mode polarization is determined via polarization-sensitive detection.

spectra at the bent-off sphere region at the right-hand side of the structure. The spectrum in 5.5 (d)) gives the corresponding spectrum with a pronounced weight of the strongly coupled mode at the intersection point.

A smaller splitting of the coupled modes can be observed also in the surrounding area of the intersection points of the bent-off sphere attached to the vertex (see fig. 5.5 (e)) Therefore, one can deduce an extended multisphere coupling even at the vertex position. This explanation of an extended coupling will be further supported by the mode intensity maps discussed below. Fig. 5.6 shows spectrally and spatially resolved intensity maps of both weakly and strongly coupled modes. These diagrams reveal clear modifications of the emission characteristics of uncoupled spheres after arranging them to CROWs: Individual spheres show bright emission located isotropically at the individual sphere boundary (see

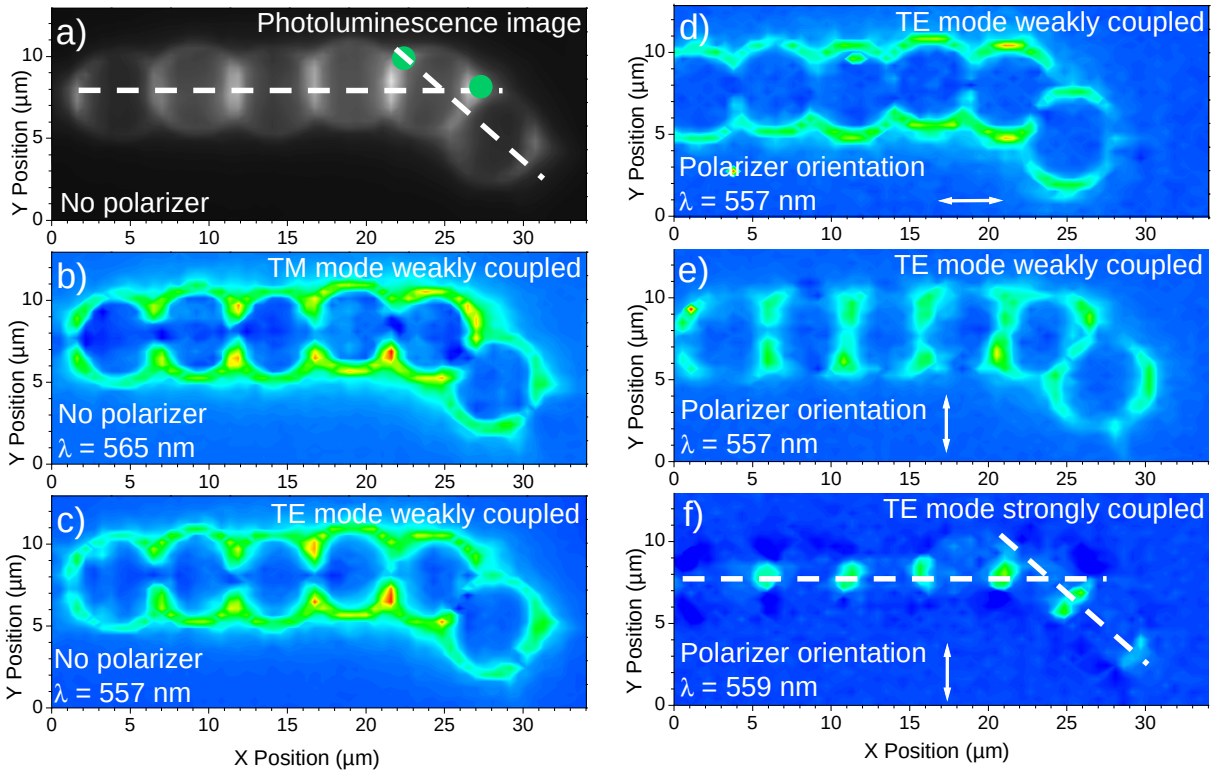

Figure 5.6: Polarization-sensitive mode maps of a six-sphere CROW structure. forming an angle of 30 degrees: (a) Spectrally integrated photoluminescence. (b) Mode map for a weakly coupled TM mode at 565 nm detected without polarization sensitivity: The vanishing mode intensities along the chain axis indicates coherent coupling. (c) Unpolarized mode map of a weakly coupled TE mode at 557 nm. (d),(e) Polarization-sensitive decomposition of the weakly coupled TE mode shown in (c) into two polarization directions. Polarizer orientations are displayed in the inset. (f) Strongly coupled TE mode detected at 559 nm with vertical polarizer orientation. The intensity spots follow the geometry with two spots in the apex sphere, indicating extended multisphere coupling.

chapter 4). In the case of CROWs, in contrast, the corresponding spectrally resolved intensity maps resonant to a single resonator mode demonstrate the modification due to CROW formation: The collective weakly coupled modes in CROWs appear now with the signature of vanishing field intensity along the CROW axis, as plotted for a TM mode in fig. 5.6 b) and a TE mode in 5.6 c)

Naturally, since even pairwisely coupled spheres would exhibit vanishing mode intensities for the weakly coupled modes at the intersection points, the distinction between pairwise coupling and extended multisphere states is not clear beforehand.

Thus, the explanation via extended multisphere coupling as given above is here further more supported by the intensity map of the sphere in the CROW vertex. As depicted in the maps, both the weakly and strongly coupled modes show the signature of vanishing intensity only at the bent intersection points, which can be only explained by means of an extended intersphere coupling. For the TE mode at 557 nm, this feature is displayed in the

diagram 5.6 d) and e) for the decomposition into two orthogonal detection polarizations. The polarizer axis is given in the inset. For a simple superpositon of pairwisely coupled spheres, the lack of mode intensity in the vertex sphere would occur at both prolonged arms of the angle, leading to four minima in the intensity distribution.

For the demonstration of extended photon states, also the strongly coupled CROW modes can be utilized as a probe, which, in contrast to the weakly coupled modes, exhibit pronounced mode emission concentrated along the CROW axis (the polarization-sensitive detection scheme ensures a correctly determined mode polarization). Here, the pronounced mode intensity would in case of a superposition of two-sphere states occur at four spatial positions in the vertex sphere lying on the prolonged arms of the angle. As can be seen in the map 5.6 f), the enhanced emission intensity occurs only at the two intersection points of the sphere chain. Therefore, the mode structure of the CROW needs to be interpreted in terms of extended intersphere coupling.

Summarizing the results, we have realized and investigated the formation of CROW structures built from nanocrystal doped polymeric microspheres. We observed the coherent coupling of the cavity fields in a row consisting of six microspheres. The extended multisphere coupling has been shown by the occurrence of additional splitting and the analysis of the spatial and spectral distribution of the mode intensity in a vertex-shaped configuration. The spatial distribution and polarization nature are explored.

6. Simplified Model for arbitrary CROW Structures

... there are basically two ways to solve problems in physics.
One is to reduce the problem to harmonic oscillators, and the other is to formulate the problem in terms of two-by-two matrices.
If two oscillators are coupled, the problem combines both two-by-two matrices and harmonic oscillators ...

Y. S. Kim and M. E. Noz (taken from abstract of ref. [Kim04])

6.1 CROWs and Coupled Harmonic Oscillators

After having experimentally examined the formation of coherently coupled photon states, we have now a closer look on the theoretical description of realistic coupled-resonator systems. In this chapter, the tight-binding model for infinite structures will be extended to finite and perturbed systems*.

The dispersion relation given in (4.8) reminds us of the dispersion of coupled harmonic oscillators. The aim of this section is to make this similarity more transparent, which allows us to extract important properties, like varying oscillator strengths in coherently coupled-resonator systems as a general feature without the expense of exact numerical field computation. For this goal, we will first reformulate the problem in a more intuitive description using the dispersion relation and the Bloch wave amplitudes from the description of the infinite structure.

Therefore, we start from the dispersion relation (4.8) given by Yariv's proposal. Let us now introduce a vector $\mathbf{\Psi}$ as follows:

$$\mathbf{\Psi} = \begin{pmatrix} \vdots \\ \Psi_{-2} \\ \Psi_{-1} \\ \Psi_0 \\ \Psi_1 \\ \Psi_2 \\ \vdots \end{pmatrix} = \begin{pmatrix} \vdots \\ e^{2iKR} \cdot \psi_t \\ e^{1iKR} \cdot \psi_t \\ e^{0} \cdot \psi_t \\ e^{-1iKR} \cdot \psi_t \\ e^{-2iKR} \cdot \psi_t \\ \vdots \end{pmatrix} . \tag{6.1}$$

*Parts of the content in this chapter have been previously submitted for publication and are meanwhile published as an article:
J. Opt. A: Pure Appl. Opt. **8** (2006), S113-S121, ©2006 Institute of Physics

This vector $\mathbf{\Psi}$ now contains the Bloch amplitudes of a given resonator and the time harmonic modulation ψ_t as its components. We multiply now the squared dispersion relation from both sides with $\mathbf{\Psi}$ and omit the contribution quadratic in κ:

$$\omega_K^2 \mathbf{\Psi} = \left[\Omega\left(1+\kappa_1\cos(KR)\right)\right]^2 \cdot \mathbf{\Psi} \approx \left(\Omega^2 + 2\kappa_1\Omega^2\cos(KR)\right)\cdot\mathbf{\Psi}\ . \tag{6.2}$$

Thanks to the structure of the chosen Ψ, which is inspired by the solution of coupled harmonic oscillators, we can now simply rewrite the cosine term to a term which couples entries Ψ_n with the next precedent and subsequent entries Ψ_{n-1} and Ψ_{n+1}:

$$2\kappa_1\Omega^2\cos(KR)\mathbf{\Psi} = \kappa_1\Omega^2 \cdot \begin{pmatrix} \vdots \\ e^{iKR}\Psi_{-1} + e^{-iKR}\Psi_{-1} \\ e^{iKR}\Psi_0 \ + \ e^{-iKR}\Psi_0 \\ e^{iKR}\Psi_1 \ + \ e^{-iKR}\Psi_1 \\ \vdots \end{pmatrix} = \kappa_1\Omega^2 \cdot \begin{pmatrix} \vdots \\ \Psi_{-2} + \Psi_0 \\ \Psi_{-1} + \Psi_1 \\ \Psi_0 \ + \Psi_2 \\ \vdots \end{pmatrix}\ . \tag{6.3}$$

Replacing the cosine expression and letting ψ_t be a time-harmonic function, eq. (6.2) reads now in component form

$$-\left(1-\frac{\omega^2}{\Omega^2}+2\kappa\right)\Psi_n = \kappa\left(\Psi_{n+1}-\Psi_n\right) - \kappa\left(\Psi_n - \Psi_{n-1}\right)\ . \tag{6.4}$$

As we can see from eq (6.4), we end up with the well-known relationships for a system of coupled linear harmonic oscillators, when we treat the single resonator eigenfrequencies as shifted frequencies of the harmonic oscillators and use a coupling constant of $\kappa_1\Omega^2$. This model is helpful for the estimation of the effects of perturbation in the system, especially for extended structures with deviations of the frequency of a single resonator, where the solution of the full set of Maxwell's equations turns out to be fragile and time-consuming and the impact on the ideal dispersion relation is not obvious. An application follows in section (6.4), when we investigate the formation of Bloch modes and introduce shorthand modeling.

From the expression of the coupling term in eq. (6.4), we note that the extension of this equivalency to differently sized cavities exhibiting slightly detuned resonance frequencies is not clear beforehand. We expect the coupling term involving neighboring cavities to be symmetric in the frequencies, but the concrete expression still has do be deduced. Therefore, the goal to the final expression is to find this equivalency explicitly involving the desired coupling terms also for detuned cavities.

6.2 Finite Coupled-Resonator Optical Waveguides

In this section, we will investigate, how the CROW relationships change, when we move over from the infinite to finite systems, whose we will always be faced with in reality. Although the Bloch formalism cannot be immediately applied in finite systems, it will be

6 Simplified Model for arbitrary CROW Structures

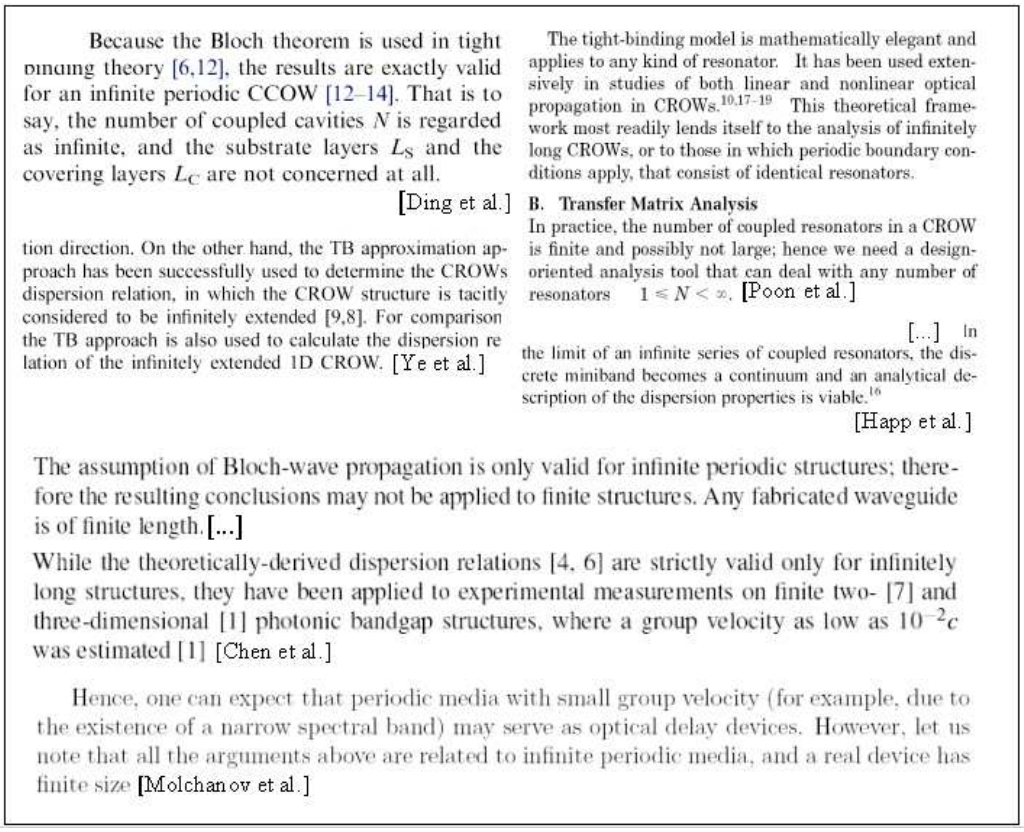

Because the Bloch theorem is used in tight binding theory [6,12], the results are exactly valid for an infinite periodic CCOW [12–14]. That is to say, the number of coupled cavities N is regarded as infinite, and the substrate layers L_S and the covering layers L_C are not concerned at all.

[Ding et al.]

tion direction. On the other hand, the TB approximation approach has been successfully used to determine the CROWs dispersion relation, in which the CROW structure is tacitly considered to be infinitely extended [9,8]. For comparison the TB approach is also used to calculate the dispersion relation of the infinitely extended 1D CROW. [Ye et al.]

The tight-binding model is mathematically elegant and applies to any kind of resonator. It has been used extensively in studies of both linear and nonlinear optical propagation in CROWs.[10,17–19] This theoretical framework most readily lends itself to the analysis of infinitely long CROWs, or to those in which periodic boundary conditions apply, that consist of identical resonators.

B. Transfer Matrix Analysis

In practice, the number of coupled resonators in a CROW is finite and possibly not large; hence we need a design-oriented analysis tool that can deal with any number of resonators $1 \leq N < \infty$. [Poon et al.]

[...] In the limit of an infinite series of coupled resonators, the discrete miniband becomes a continuum and an analytical description of the dispersion properties is viable.[16]

[Happ et al.]

The assumption of Bloch-wave propagation is only valid for infinite periodic structures; therefore the resulting conclusions may not be applied to finite structures. Any fabricated waveguide is of finite length. [...]

While the theoretically-derived dispersion relations [4, 6] are strictly valid only for infinitely long structures, they have been applied to experimental measurements on finite two- [7] and three-dimensional [1] photonic bandgap structures, where a group velocity as low as $10^{-2}c$ was estimated [1] [Chen et al.]

Hence, one can expect that periodic media with small group velocity (for example, due to the existence of a narrow spectral band) may serve as optical delay devices. However, let us note that all the arguments above are related to infinite periodic media, and a real device has finite size [Molchanov et al.]

Figure 6.1: In current literature published in the years 2003 to 2005, we face the conventional wisdom, which states, that Yariv's tight-binding model would give less insight for finite and disordered structures [Din04, Ye04, Poo04c, Che04, Hap03, Mol05a]. This topic will be thoroughly discussed here in the frame of a simplified reformulation of the tight-binding model. We will show in this section, how the key properties of finite and disordered structures *can instead be fully deduced from that model.*

discovered in the following, that the formalism can be kept in close analogy to that of the preceding section. Offering a quite general treatment, the findings might be useful as an overall framework for discovering more complicated CROW geometries. For instance, questions arose [Che04], whether Yariv's treatment can be applied for CROW structures consisting of three cavities in the microwave regime [Bay00]. This is especially important, as the topic of finite CROWs is increasingly debated in current literature of the last two years. Here, a conventional wisdom has been established, that Yariv's treatment is useful for a general motivation of coupled-resonator systems and the hypothetical case of degenerate and infinite structures, namely, less applicable for realistic systems [Din04, Ye04, Poo04c, Che04, Hap03, Mol05a]. A collection of current statements in literature is given in figure 6.1. A common way out is often seen in dealing with more specific geometries, where the coupling conditions are well known, e.g. the treatment of microrings and Fabry-Perot-like resonators. To overcome these limitations, the treatment should involve now finite CROWs in a general frame, where no immediate dependence on the resonator type is incorporated. As will turn out, the objections which have been suggested

against early work, do not hold in this case. Furthermore, this classification allows a complete picture with respect to slightly different work on coupled resonators, e.g. the type proposed by R. W. Boyd. We will see, that this field of coupled-resonator phenomena can be ordered into a quite compact picture.

6.3 Finite CROW Structures

The most important difference in the matrix formalism for finite systems of coupled resonators lies in the change of the boundary conditions, i.e., in a CROW consisting of N cavities, the first and the N-th resonators are coupled to one single neighbor only. As a consequence, the system is governed by a finite $N \times N$ matrix with the first normalized single resonator frequency located in the upper left and the N-th single resonator frequency in the lower right position, if the eigenstate vector $\mathbf{\Psi}$ contains the Bloch amplitude of the n-th resonator in the component Ψ_n. For simplicity, we keep the single resonator resonances degenerate in this discussion, which provides us with the possibility to exactly diagonalize the system matrix without further matrix computation for arbitrary N. In what follows, the time harmonic dependence is omitted for compactness. We arrive at the following eigenvalue equation

$$\begin{pmatrix} 1 & \kappa & 0 & \cdots & 0 \\ \kappa & 1 & \kappa & 0 & \cdots & 0 \\ 0 & \kappa & 1 & \kappa & \ddots & \vdots \\ \vdots & \ddots & \ddots & \ddots & \ddots & \ddots & \vdots \\ \vdots & & \ddots & \ddots & \ddots & \ddots & 0 \\ 0 & \cdots & 0 & \kappa & 1 & \kappa \\ 0 & \cdots & & 0 & \kappa & 1 \end{pmatrix} \begin{pmatrix} \Psi_1 \\ \vdots \\ \vdots \\ \Psi_n \\ \vdots \\ \vdots \\ \Psi_N \end{pmatrix} = \frac{\omega_K^2}{\Omega^2} \begin{pmatrix} \Psi_1 \\ \vdots \\ \vdots \\ \Psi_n \\ \vdots \\ \vdots \\ \Psi_N \end{pmatrix} . \tag{6.5}$$

The system matrix in (6.5), has a symmetric and tridiagonal structure, however, the first and last elements are apparently breaking the symmetry in the component equations. In other words, we are dealing with a special type of boundary conditions, which affects the usual Bloch formalism. The solution of the eigenvalue equation relies on two assumptions:

First, we seek for solutions with a wave-like behavior, which keeps the connection to the Bloch formalism as close as possible. For the eigenvector components, we accordingly decide for an ansatz for $\mathbf{\Psi}$ in dependence on a specific k_i

$$\mathbf{\Psi} \text{ with components } \Psi_n = \cos(nk_iR + \phi) , \tag{6.6}$$

in which we allow for initially unfixed parameters k_i analogous to the Bloch wave vector in infinite systems and a phase ϕ. Both quantities will be fixed due to the requirement that ansatz (6.6) indeed solves our problem (6.5).

Second, let us assume as an *educated guess*, that the preceding expression of the eigenvalues (4.8) for the infinite case will still hold in the finite case, so that the finiteness of the

problem results in a modification and discretization of the allowed Bloch vectors and the eigenfrequencies can be derived from the modified Bloch vectors in a forminvariant way:

$$\frac{\omega_K^2}{\Omega^2} = 1 + 2\kappa\cos(k_i R) \ . \tag{6.7}$$

It will turn out in the following, that this initial assumption is indeed justified. For the internal values, i.e. the n-th component equations with $1 \neq n \neq N$, we have now the condition

$$\begin{aligned}
&\Psi_n + \kappa\Psi_{n+1} + \kappa\Psi_{n-1} \\
&\quad = \cos(nkR+\phi) + \kappa\cos((n+1)kR+\phi) + \kappa\cos((n-1)kR+\phi) \\
&\quad = [1+2\kappa\cos(kR)]\cos(nkR+\phi) \\
&\quad = [1+2\kappa\cos(kR)]\,\Psi_n \ ,
\end{aligned}$$

which is obviously satisfied for any choice of parameters k_i and ϕ. More restrictions on the general solution (6.15) are imposed by the two boundary conditions for the first and N-th resonator: For the first case, we require the first component equation to be satisfied,which can be rewritten using relations for sums in the argument of the cosine function:

$$\begin{aligned}
\Psi_1 + \kappa\Psi_2 &= \cos(kR+\phi) + \kappa\cos(2kR+\phi) \\
&= \cos(kR+\phi) + \kappa\cos(kR)\cos(kR+\phi) - \kappa\sin(kR)\sin(kR+\phi) \\
&\stackrel{!}{=} 2\kappa\cos(kR)\cos(kR+\phi) + \cos(kR+\phi) \\
&= (1+2\kappa\cos(kR))\,\Psi_1 \ .
\end{aligned} \tag{6.8}$$

Thus, this condition leads to

$$\Leftrightarrow \quad -\sin(kR)\sin(kR+\phi) = \cos(kR)\cos(kR+\phi) \ . \tag{6.9}$$

This condition fixes the phase in eq. (6.6) to

$$\Rightarrow \phi = \pm\frac{\pi}{2} \ . \tag{6.10}$$

Thus, the boundary condition can only be fulfilled for a sine-like function. We choose

$$\phi = -\frac{\pi}{2} \tag{6.11}$$

for the Bloch phase, since its sign only determines the sign of the sine-function and does not provide an independent solution to the eigenvalue equation. The boundary condition for the N-th resonator leads to the remaining component equation:

$$\begin{aligned}
&\kappa\Psi_{N-1} + \Psi_N = \kappa\sin((N-1)kR) + \sin(NKR) \\
&\quad \stackrel{!}{=} (2\kappa\cos(kR)+1)\sin(NkR) = (1+2\kappa\cos(kR))\,\Psi_N \ .
\end{aligned} \tag{6.12}$$

With addition theorems for the arguments, we achieve with straightforward manipulation

$$\begin{aligned}
&\Rightarrow \kappa \sin(NkR)\cos(kR) - \kappa\cos(NkR)\sin(kR) \\
&\quad \stackrel{!}{=} 2\kappa\cos(kR)\sin(NkR) \\
&\quad \Leftrightarrow -\cos\left[(N+1)kR - kR\right]\sin(kR) \stackrel{!}{=} \cos(kR)\sin\left[(N+1)kR - kR\right] \\
&\quad \Rightarrow \sin((N+1)kR)\left(\cos^2(kR) + \sin^2(kR)\right) = 0 \\
&\quad \Rightarrow (N+1)kR = i\cdot\pi \\
&\quad \Rightarrow k = \frac{i\cdot\pi}{(N+1)\cdot R} = k_i \ . \qquad (6.13)
\end{aligned}$$

Thereby, the component equation for the n-th resonator fixes the absolute value of the wave vector.

From (6.13) and (6.11) it follows, that the $N \times N$ matrix equation (6.5) is solved with N different eigenvalues and N related eigenvectors. From the theory of matrix diagonalization it follows, that the complete solution for the finite CROW structure is found, given below in a concise manner:

$$\begin{pmatrix} 1 & \kappa & 0 & \cdots & \\ \kappa & 1 & \kappa & \ddots & \\ & \ddots & \ddots & \ddots & \\ & \ddots & \kappa & 1 & \kappa \\ & \cdots & 0 & \kappa & 1 \end{pmatrix} \cdot \begin{pmatrix} \sin(1k_iR) \\ \vdots \\ \sin(nk_iR) \\ \vdots \\ \sin(Nk_iR) \end{pmatrix} = (1 + 2\kappa\cos(k_iR)) \cdot \begin{pmatrix} \sin(1k_iR) \\ \vdots \\ \sin(nk_iR) \\ \vdots \\ \sin(Nk_iR) \end{pmatrix} \ , \quad (6.14)$$

with the dispersion relation

$$(1 + 2\kappa\cos(k_iR)) = \frac{\omega_K^2}{\Omega^2} \text{ and} \qquad (6.15)$$

and the wave vector k_i

$$k_i = \frac{i\cdot\pi}{(N+1)R} \text{ , with } i = 1, \ldots, N \ . \qquad (6.16)$$

In the case of small coupling constants κ, the dispersion relation 6.15 can be simplified as

$$\frac{\omega_{k_i}}{\Omega} = \sqrt{1 + 2\kappa\cos(k_iR)} \approx 1 + \kappa\cos(k_iR) \ . \qquad (6.17)$$

From the Bloch phases, the intensity distribution patterns can be easily evaluated. Since we get the relative intensity as the square of the Bloch amplitude for a given resonator, we end up with a mirror symmetry of the intensity patterns around the single resonator frequency:

$$\sin^2\left(\frac{i\pi}{N+1}\right) = \sin^2\left(\frac{(N-i+1)}{N+1}\right) \ . \qquad (6.18)$$

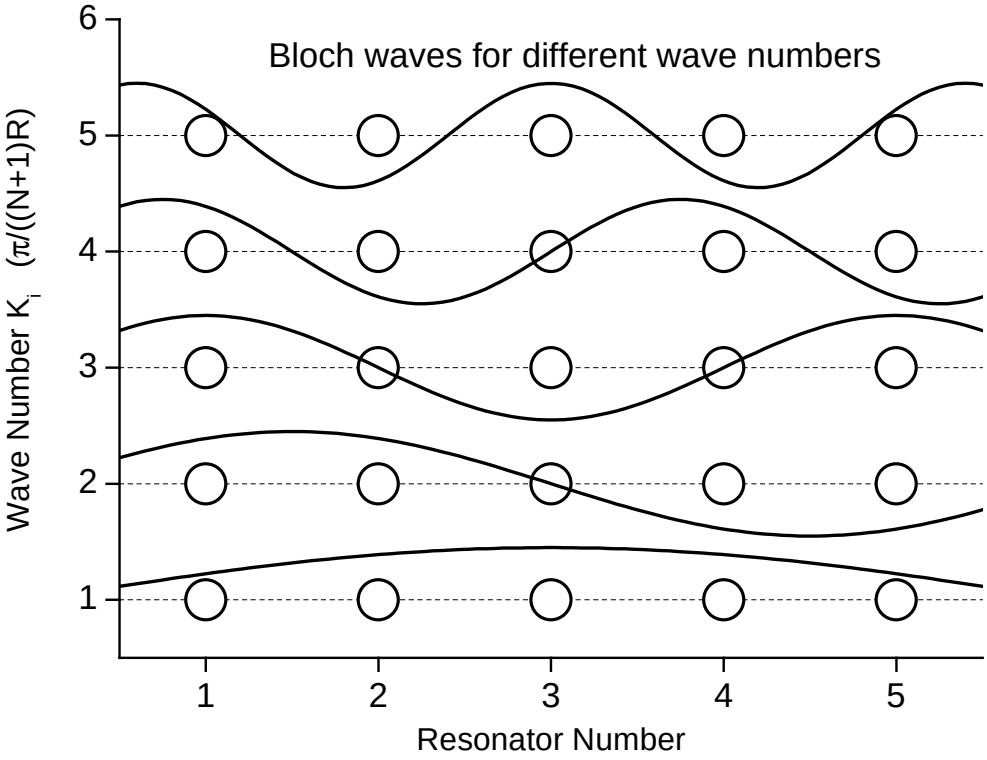

Figure 6.2: Schematic representation of the CROW Bloch envelopes in a finite resonator chain. The finiteness results in boundary conditions allowing standing wave patterns.

For a CROW with odd resonator number, one finds a Bloch-mode at the single resonator frequency, while for even resonator CROW no Bloch-mode is found. Thus, one gets a manifold of $\frac{N+1}{2}$ different intensity patterns for uneven N and $\frac{N}{2}$ different intensity patterns for the even case. This result is in close agreement with more specific field computations in coupled microrings, e.g. [Che04].

As we see from above relations, the eigenmodes of a finite CROW can be described as *standing Bloch waves*, each exhibiting a sine-like envelope. Accordingly, a finite CROW can be regarded as a single cavity for the envelope waves, whose node points approach the position of the first and last resonators the better, the larger the number of resonators involved.

An illustration of this relation is given in fig. 6.2. Here, for comparison, standing Bloch waves in finite structures consisting of five resonators are plotted for the allowed wave numbers in dependence of the individual resonator position. The amplitude of the Bloch wave gives the strength of the electric field at an individual resonator position (plotted in vertical direction). The wave numbers are arranged in ascending order on the vertical axis, which corresponds to smaller energies for positive coupling parameters according to eq. (6.18). As illustrated in the Bloch amplitudes, the Bloch waves can be classified into symmetric and antisymmetric modes, alternating with ascending wave numbers. For uneven structures, a CROW generally obeys antisymmetric modes at specific CROW frequencies. Hence in the case of uneven CROWs we can find nodes of the Bloch waves at

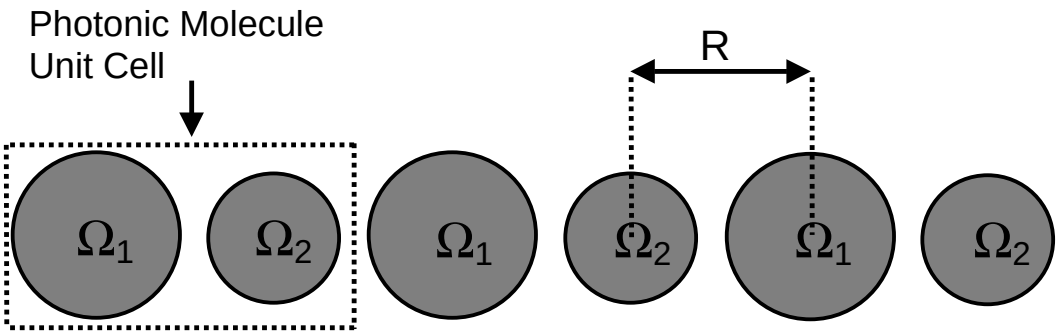

Figure 6.3: Scheme of a perturbed coupled-resonator optical waveguide. In order to explore the modified coupling conditions, the perturbation is assumed to be periodical, so that the Bloch-ansatz can still be applied.

the center position, or at resonator positions, which are symmetrically arranged around the center resonator and thus display a vanishing oscillator strength. In the case of an even number of resonators, the nodes never match with a resonator position, and vanishing oscillator strengths do not occur.

It should be noted, that the *strength* of the coupling parameter is only contained explicitly in the eigenfrequencies. The Bloch vectors, responsible for the intensity response of the system, are independent on the coupling parameter, as long as it deviates from zero. This might play an important role for a CROW classification, since the intensity distribution can be treated as an independent quantity and a general property of a CROW candidate. Therefore, we can use this feature for the discussion of the fine structure of the weakly coupled modes, whose mode maps have been demonstrated in subsection 4.0.4. The individual Bloch intensities can thus serve as an independent additional check for coherent interresonator coupling. While the discussion of the mode maps in the previous chapter mainly focussed on the apex sphere in a hockey stick geometry, including both neighboring resonators (and thus explaining the mode maps by at least a full three-sphere coupling in a bent geometry) the formation of Bloch states are strictly connected to *all* resonators in a CROW structure and represent the remaining proof for interresonator coupling across a whole CROW.

6.4 Simplified Model for Detuning in CROW Structures

In order to achieve a simplified model for detuning in a crow structure, we extend Yariv's model which is formulated for a periodic arrangement of single resonators to an periodic arrangement of next-neighbor coupled photonic molecules, each consisting of two different cavities with resonance frequencies Ω_1 and Ω_2. This model is depicted in diagram 6.3. This appears to be a proper choice, because in the spirit of tight-binding coupling, all coupling terms contained in this system exhibit a mixture of the same two resonance

frequencies. Thus the validity of Yariv's model requiring the solution to be expressed in a Bloch-mode formulation is preserved, since still the periodicity, now for photonic molecules, is kept in this problem.

This different arrangement suggest now a modified Bloch-ansatz with the periodicity of a photonic molecule, whose electric field can be expressed as

$$\begin{aligned}\mathbf{E}_K &= E_0 e^{i\omega_K t} \cdot \Big(\sum_n e^{-i\cdot 2n\cdot KR} A_1 \mathbf{E}_{\Omega_1}(\mathbf{r} - 2n\cdot R\mathbf{e}_z) \\ &\quad + \sum_n e^{-i\cdot(2n+1)\cdot KR} A_2 \mathbf{E}_{\Omega_2}(\mathbf{r} - (2n+1)\cdot R\mathbf{e}_z)\Big) \ . \end{aligned} \tag{6.19}$$

To evaluate the impact of different eigenfrequencies we perform an analogous calculation like in the single resonator case. Both terms appearing in Maxwell's equations (4.3) are now multiplied with either the field $\mathbf{E}_{\Omega_1}$ or $\mathbf{E}_{\Omega_2}$, and subsequent spatial integration leads to the expression

$$\omega_K^2 = \frac{\Omega_1^2 A_1 + 2\Omega_2^2 A_2 \cos(KR)\cdot\beta_1}{A_1 + 2A_2\cos(KR)\cdot\alpha_1} \ , \tag{6.20}$$

where the indices above apply for the choice of multiplication with field $\mathbf{E}_{\Omega_1}$. The same expression holds for multiplication with the field $\mathbf{E}_{\Omega_2}$ if the indices 1 and 2 are exchanged for the quantities Ω and A. We keep the constants α_1 and β_1 unchanged for the case of small detunings. For nanometer sized size deviations the spatial mode profile, naturally on the micrometer scale, and accordingly the overlap integral is not much affected, but might be accompanied with a shift of eigenresonances well exceeding the resonance linewidth. While in general the coupling constant is decreasing exponentially, e.g, with the intercavity distance [Guv05], the coupling constant is quite insensitive to size variations or gap developments in the nanometer range. For whispering gallery modes in microcylinders, the stability of the coupling constants for small parameter deviations has been demonstrated, e.g., in [Den05]. Assuming again, that the quantities α_1 are small compared to unity, we end up with

$$\omega_K^2 = \Omega_1^2 + 2\frac{A_2}{A_1}\left(\Omega_2^2\cos KR\beta_1 - \Omega_1^2\cos KR\alpha_1\right) \ . \tag{6.21}$$

Since we expect to end with coupling terms symmetric in the frequencies Ω_1 and Ω_2, we rewrite the terms multiplied with $\cos(KR)$ in a symmetric manner:

$$\Omega_2^2\beta_1 - \Omega_1^2\alpha_1 = \frac{\Omega_1^2+\Omega_2^2}{2}(\beta_1-\alpha_1) - \frac{\Omega_2^2-\Omega_1^2}{2}(\beta_1+\alpha_1) \ . \tag{6.22}$$

For small frequency detuning of the resonator eigenfrequencies and small quantities α_1, β_1, the contribution of the last term on the right-hand side of eq. (6.22) can be omitted.

Thus, we get now the coupled equations for the frequency of the whole system ω_K

$$\omega_K^2 = \Omega_1^2 + 2\frac{A_2}{A_1}\left(\Omega_2^2\cos KR\beta_1 - \Omega_1^2\cos KR\alpha_1\right) \tag{6.23}$$

$$\approx \Omega_1^2 + 2\frac{A_2}{A_1}\frac{\Omega_1^2+\Omega_2^2}{2}\kappa_1 \text{ for the } (2n)\text{-th resonator and} \tag{6.24}$$

$$\omega_K^2 \approx \Omega_2^2 + 2\frac{A_1}{A_2}\frac{\Omega_1^2+\Omega_2^2}{2}\kappa_1 \text{ for the } (2n+1)\text{-th resonator.} \tag{6.25}$$

To map the CROW problem onto the harmonic oscillator problem, we multiply the above system of equations with a vector

$$\Psi = \begin{pmatrix} \vdots \\ A_1 e^{i\cdot 2n\cdot KR} \\ A_2 e^{i\cdot(2n+1)\cdot KR} \\ \vdots \end{pmatrix}, \tag{6.26}$$

with alternating prefactors A_1 and A_2. The replacement of the cosine terms — as we did already in the case of identical resonators — leads us to the following system of equations:

$$\omega_K^2\Psi_{2n} = \left(\Omega_1^2 + 2\left(\Omega_1^2+\Omega_2^2\right)\kappa_1\right)\Psi_{2n} + 2\frac{\Omega_1^2+\Omega_2^2}{2}\kappa_1\left(\Psi_{2n+1}+\Psi_{2n-1}-2\Psi_{2n}\right) \tag{6.27}$$

$$\omega_K^2\Psi_{2n+1} = \left(\Omega_2^2 + 2\left(\Omega_1^2+\Omega_2^2\right)\kappa_1\right)\Psi_{2n+1} + 2\frac{\Omega_1^2+\Omega_2^2}{2}\kappa_1\left(\Psi_{2n+2}+\Psi_{2n}-2\Psi_{2n+1}\right)\ . \tag{6.28}$$

This system of equations describes a system of coupled harmonic oscillators with alternating single oscillator frequencies and coupling constants scaling symmetrically with the frequencies of neighboring oscillators. Since systems of coupled harmonic oscillators are commonly solved by applying matrix diagonalization techniques, we have all necessary relations at hand to formulate a matrix model to describe an arbitrary CROW structure. The related eigenvectors, which we introduced to map the problem on that of coupled harmonic oscillators, we may interpret as a *brightness vector*, since it would coincide with the CROW solution, if we assume, that the field intensity related to the n-th single resonator is mostly determined by the contribution $E_{\Omega_i}(r - nR\mathbf{e}_z)$.

We note here one important difference between quantum confined semiconductor quantum dots and periodic arrangements of photonic dots: In electronic crystals, the confinement in nanostructured semiconductors occurs for the envelope function of the electrons and the Bloch part of the electronic wave acts as a perturbation on a smaller subscale. In coupled-resonator optical waveguides, however, the confinement in photonic dots is realized on the smaller single resonator subscale, whereas the Bloch part of the photonic wave can be considered as a new envelope. Thus, a more exact comparison to a crystalline solid state material would be a semiconductor hetero-structure, used e.g. in quantum cascade lasers.

In the case of small disorder, the limit of slightly different single-resonator frequencies, the governing eigenvalue problem is formulated as

$$\begin{pmatrix} \Omega_1^2 & \frac{\Omega_1^2+\Omega_2^2}{2}\kappa & 0 & \cdots & \\ \frac{\Omega_1^2+\Omega_2^2}{2}\kappa & \Omega_2^2 & \kappa\cdot\frac{\Omega_2^2+\Omega_3^2}{2} & \ddots & \\ & \ddots & \ddots & \ddots & \\ & \ddots & \frac{\Omega_{N-2}^2+\Omega_{N-1}^2}{2}\kappa & \Omega_{N-1}^2 & \frac{\Omega_{N-1}^2+\Omega_N^2}{2}\kappa \\ & \cdots & 0 & \frac{\Omega_{N-1}^2+\Omega_N^2}{2}\kappa & \Omega_N^2 \end{pmatrix} \cdot \mathbf{\Psi} = \omega_i^2\mathbf{\Psi}\ . \tag{6.29}$$

In this equation, the modified eigenfrequencies and the related Bloch vectors can be solved for numerically.

The modified system matrix of detuned CROWs can be described as a perturbation of the system matrix of an ideal CROW, if the squared single resonator frequencies are incorporated as the diagonal of a perturbation matrix $\hat{P}$:

$$\hat{P} = \begin{pmatrix} \Omega_1^2 & 0 & \ldots\ldots & 0 \\ 0 & \Omega_2^2 & 0 & \ldots & 0 \\ \vdots & \ddots & \ddots & \ddots & \vdots \\ \vdots & \ddots & \ddots & \ddots & 0 \\ 0 & \ldots\ldots & 0 & \Omega_N^2 \end{pmatrix} . \tag{6.30}$$

Labelling the system matrix for the fully degenerate finite CROW system according to section 6.2 as $\hat{T}$

$$\hat{T} = \begin{pmatrix} 1 & \kappa & \ldots\ldots & 0 \\ \kappa & 1 & \kappa & \ldots & 0 \\ \vdots & \ddots & \ddots & \ddots & \vdots \\ \vdots & \ddots & \kappa & 1 & \kappa \\ 0 & \ldots\ldots & \kappa & 1 \end{pmatrix} , \tag{6.31}$$

the perturbed system matrix $\hat{S}$ reads in a more compact formulation

$$\hat{S} = \frac{1}{2}\left(\hat{T}\cdot\hat{P} + \hat{P}\cdot\hat{T}\right) . \tag{6.32}$$

From this formulation, we can readily estimate the asymptotic limits of vanishing and large detuning, respectively:

For the case of vanishing detuning of the single resonator frequencies, the perturbation matrix becomes simply the square of the single resonator frequency times a unity matrix and the model is described as discussed in section 6.2. For large detunings, an estimation of the detuning dependence of the coupling constant becomes more difficult and involves detailed computations of the cavity mode overlaps. However, in general, the coupling constant becomes smaller with increasingly large detunings (see e.g., [Ast04]). In parallel it is obvious, that for large detunings the actual value of the coupling constant becomes less important. From the asymptotic behavior of large detunings it is understood, that the modes can be described as uncoupled isolated systems. In this case, we can neglect the coupling constant in eq. (6.31) by setting it to zero without introducing a significant error to the resulting eigenfrequencies. Thus, the matrix $\hat{T}$ becomes the unity matrix. Accordingly, the system matrix can be described as a diagonal matrix with the individual squared cavity resonances as entries, which represents an entirely uncoupled system. An overview of the different perturbation regimes is summarized in the following tabular 6.1:

Table 6.1: Overview of the different perturbation regimes in a coupled-resonator optical waveguide:

Perturbation Regime	System Equation
No Perturbation	$\Omega^2_{\text{Resonator}}\hat{T}\cdot\mathbf{\Psi}_{\text{Bloch}} = \omega^2_{\text{CROW}}\cdot\mathbf{\Psi}_{\text{Bloch}}$
Small Perturbation	$\frac{1}{2}\left(\hat{T}\hat{P}+\hat{P}\hat{T}\right)\cdot\mathbf{\Psi}_{\text{Bloch}} = \omega^2_{\text{CROW}}\cdot\mathbf{\Psi}_{\text{Bloch}}$
Large Perturbation	$\hat{P}\cdot\mathbf{\Psi}_{\text{Bloch}} = \omega^2_{\text{CROW}}\cdot\mathbf{\Psi}_{\text{Bloch}}$

Thus, all important limits in the discussion of finite coupled-resonator optical waveguides can be described in a very general manner in the frame of the tight-binding approach.

This again motivates the evaluation of disordered CROWs, theoretically developed in the preceding subsection, since in an extended CROW with fully degenerate single resonator frequencies the boundary conditions imply, that the first and last resonator in a CROW only contain a small fraction of the Bloch wave energy. Thus, incoupling of light would result in a difficult task. Since the CROW mechanism itself may be subject to disorder, one way might be to introduce defects intentionally.

6.5 Standing Bloch Waves in Coupled Microspheres

In order to check the splitting of the weakly coupled modes, we turn now to the three-sphere system already discussed in section 4.0.4 with respect to the localization of weakly and strongly coupled modes.

For illustration, the corresponding Bloch waves in a three-sphere structure are displayed in fig. 6.4. In this case, two different intensity patterns occur due to the discussions of eq. (6.18). The central mode degenerate with the single sphere resonance displays a node at the center resonator, thus the light is localized only at the edge resonators. The up- and downwards split Bloch modes display intensity maxima at the center resonator position.

Next, we examine the Bloch-mode formation in a three-resonator system. Since the spectral shift of weakly coupled modes is comparatively small, a mode mapping is now performed with a significantly reduced spectral window. As we expect from the discussion in section 6.1, a three-resonator CROW mode should consist of a pronounced splitting of modes at the center resonator, whereas the end resonator should be dominated by the frequency of an isolated resonator. The detected intensity variation for a three-sphere chain is displayed in fig. 6.5.

The obtained intensity maps have been measured with a significantly reduced spectral detection window in order to resolve different Bloch states separately. As given in fig. 6.5, for the weakly coupled mode centered around 591.7 nm the emission is mainly confined in the center sphere. For a slightly different detection wavelength at 592.15 nm, the emission stems mainly from the edge resonators. Thus, the weakly coupled modes can — detected with a fine resolution — be decomposed into modes with alternating oscillator strengths,

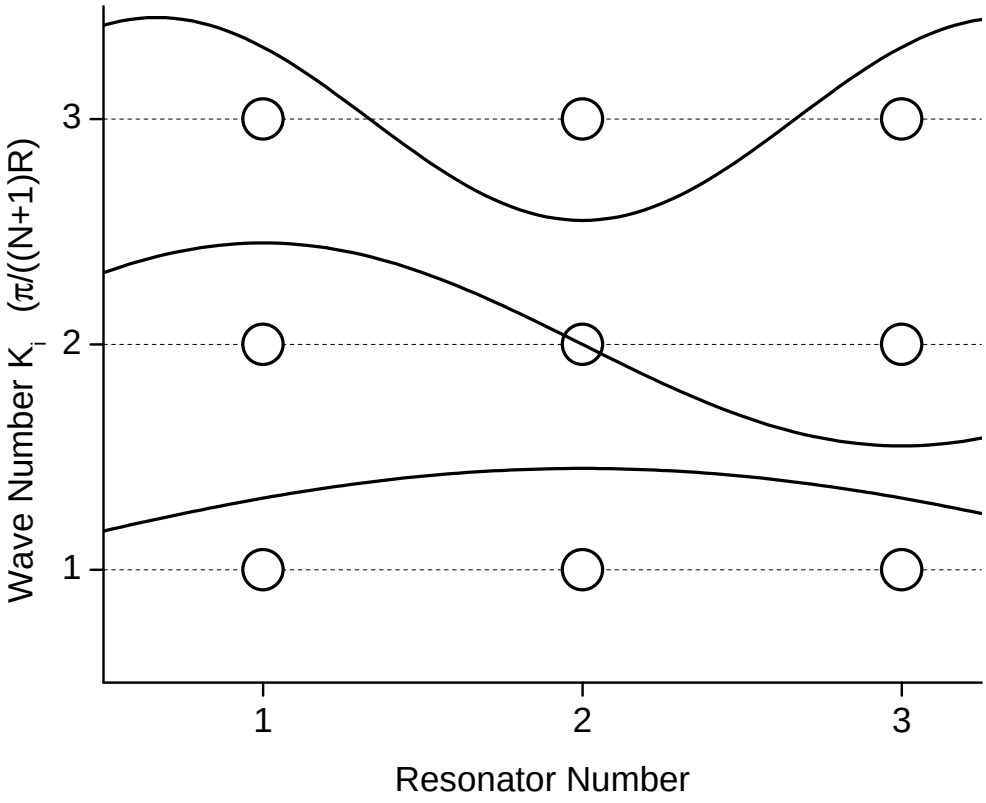

Figure 6.4: Standing Bloch waves for a triple resonator chain.

which establishes an additional criterion for coherent mode evolution in finite coupled resonator systems. Combing the criteria for coherent mode coupling in coupled-resonator optical waveguides, we can summarize: (i) the evolution of a fine structure consisting of n peaks in a chain of n coupled resonators (ii) the redistribution of the light emitted into a CROW into modes resembling the symmetry of the linear alignment with respect to the chain axis. (iii) the variation in the oscillator strength in adjacent resonators in a CROW.

The evolution of CROW modes in a resonator chain of six resonators is displayed in diagram 6.6. Here, the sixth resonator is initially uncoupled to the remaining five resonator chain (uppermost diagram). In the subsequent diagram, the coupling constant is varied from zero coupling to full coupling in linear steps. That way, we can follow the evolution of CROW modes from a degenerate five resonator chain towards a six resonator chain. Here, the square of the Bloch-amplitude is plotted as gray-scale coded stripes centered around the resonator positions for all CROW frequencies in the horizontal axis. The vertical axis displays the associated CROW frequency, which has been normalized to the eigenfrequency of an isolated resonator. For the case of an initially uncoupled sixth resonator, diagram a) displays the Bloch-mode pattern for an uneven number of resonators. As apparent in the diagram, only a subset of modes dominates the CROW spectra at a chosen resonator position, varying along the CROW. The square of the Bloch modes, which can be regarded as a measure of the mode intensity, display a mirror symmetry centered around the middle resonator. If the coupling strength of the sixth resonator is increased, a new mode is formed by a splitting of the CROW mode at the center frequency, whereas

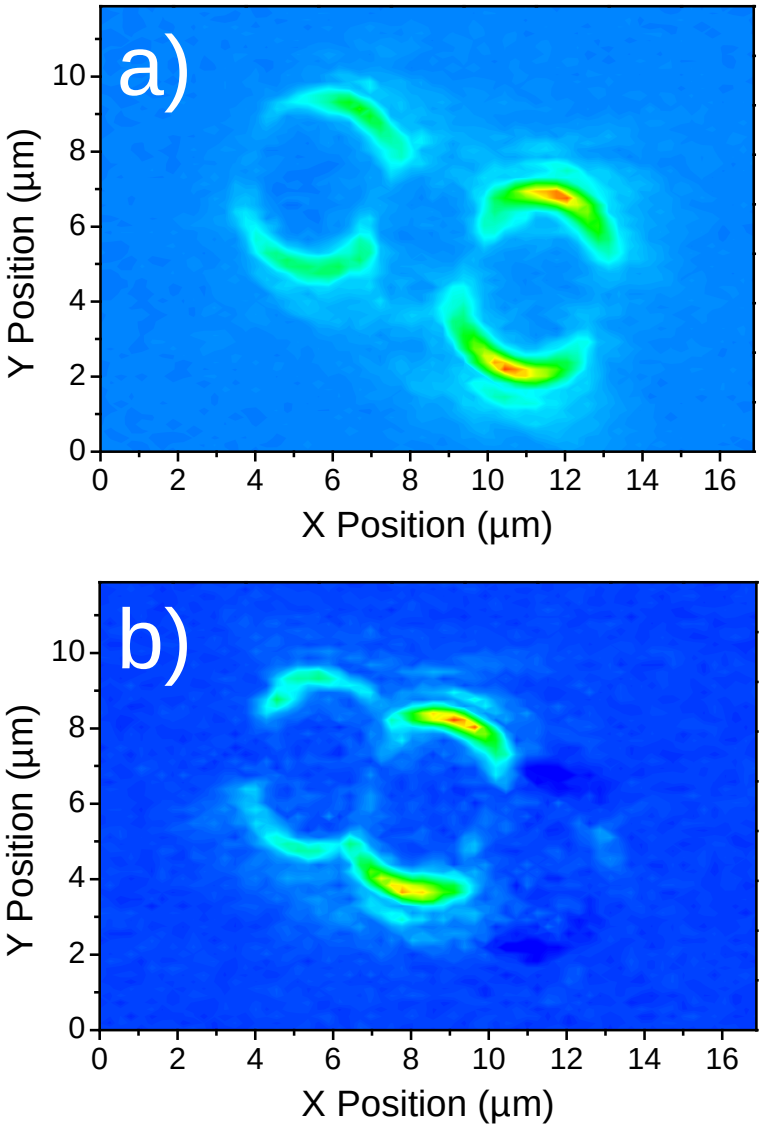

Figure 6.5: Polarization-sensitive mode maps resonant to the three-sphere fine structure. At the center resonance (592.15 nm), the intensity stems from the edge spheres. At a slightly smaller wavelength (591.7 nm) compared to the map above, the luminescence is detected at the center position only. The map is detected TE-sensitively.

the outer frequency modes are slightly shifted away from the center frequency. The field intensity from the sixth resonator is transferred to the other resonators in a symmetry breaking manner: CROW modes, which initially have spatially symmetric Bloch-nodes at certain resonator numbers, gain now in mode intensity, but with different growth. The node resonators next to the additionally coupled sixth resonator are significantly preferred in the additional oscillator strength. When the coupling constant is further increased, the pattern acquires the spatial symmetry of an even number CROW. Here, the the mirror plane is located at half distance between the two center resonators. Here again, the vast contrast in the CROW modes for a given resonator leads to a subset of modes, which dominates the corresponding spectrum. Of particular interest is now the case of an al-

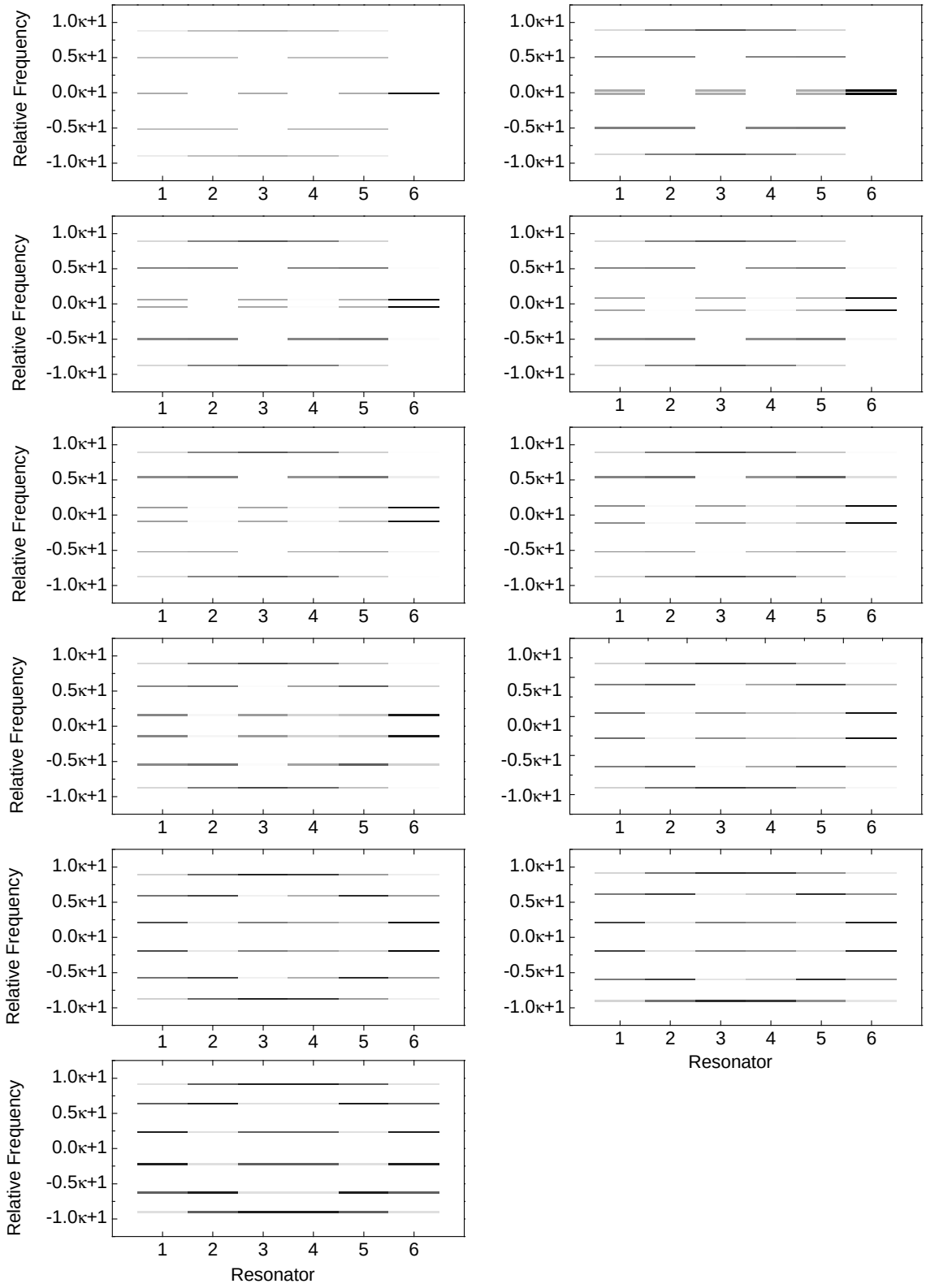

Figure 6.6: Scheme of alternating oscillator strengths in a 5 resonator chain. The subsequent diagrams show the modifications, when a sixth resonator is added. The coupling constant is varied in equal steps from zero coupling to full coupling (from left to right and from top to bottom).

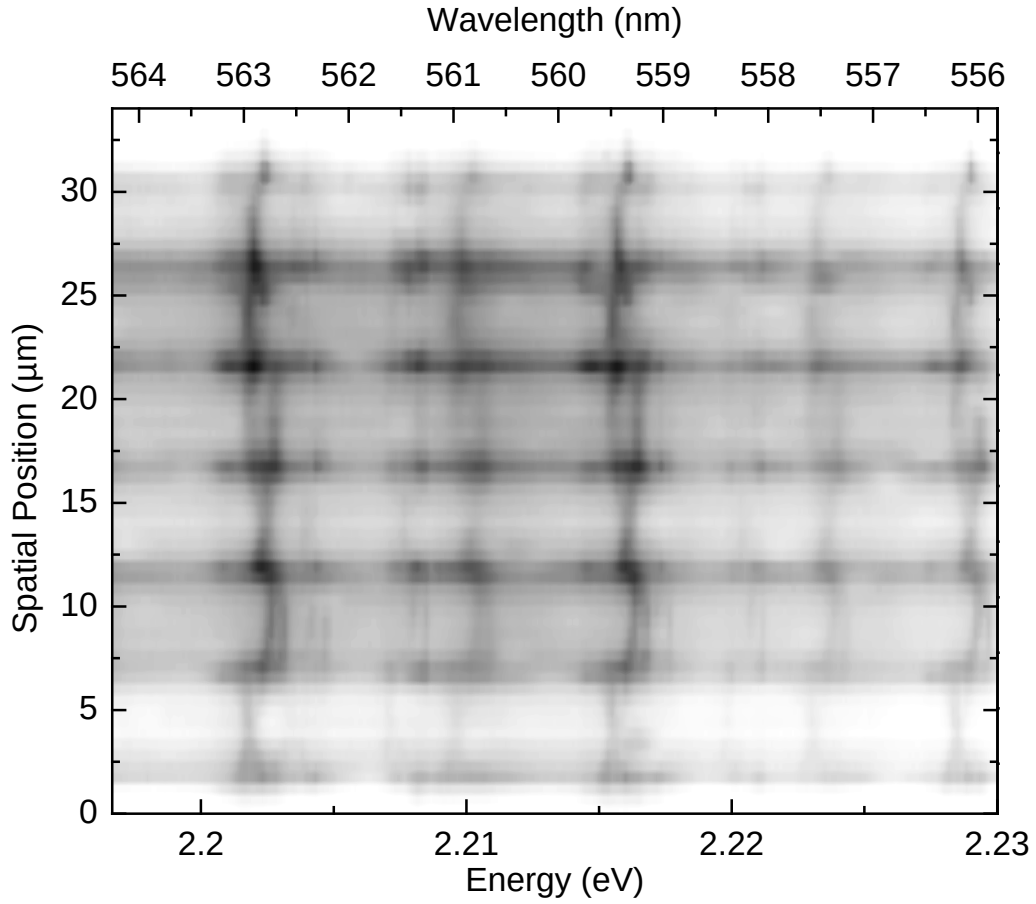

Figure 6.7: The coupling of multiple cavities leads to a pronounced splitting of resonances across the chain direction not observed in single microspheres.

most fully coupled resonator in diagram e): There, the broken spatial symmetry of the CROW pattern displays modes, which show an almost vanishing oscillator strength for a single resonator only without a mirror symmetric counterpart (see the two center modes at resonator number two). Thus, such a mode pattern might serve as a tool for the determination of CROW mode formation in case of slightly asymmetric CROW structures. An example is be given for the bent CROW mode discussed previously in fig. 6.8.

With the results obtained in the previous section, we are now able to schematically classify the relationships between different concepts concerning coupled-resonator phenomena and their analogous physical counterparts. Diagram 6.9. proposes one possible schematization:

The coupled-resonator optical waveguide, as has been proposed in its idealization of degenerate and infinitely extended structures by Yariv *et al.* in 1999 in close analogy to the tight-binding model formalism in solid-state physics is displayed on the left-hand side. In the previous section, we demonstrated, that this formalism of coupled resonators can be traced back further to the model of coupled harmonic oscillators. The model allows the truncation of the coupled resonator structure and therefore the generalization to the case of structures with arbitrary resonator numbers. For the case of perturbed CROWs with slightly detuned resonators, we have first used the tight-binding model for an infinite

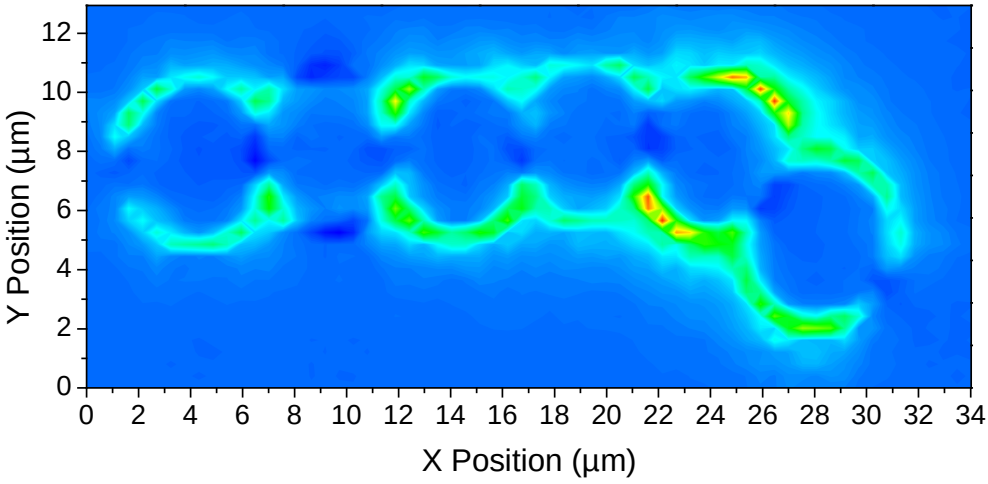

Figure 6.8: Polarization-sensitive intensity map of the bent microcavity chain (see chapter 5), resolving the fine structure of a TE_{30}^{2} mode. The second resonator remains almost field free.

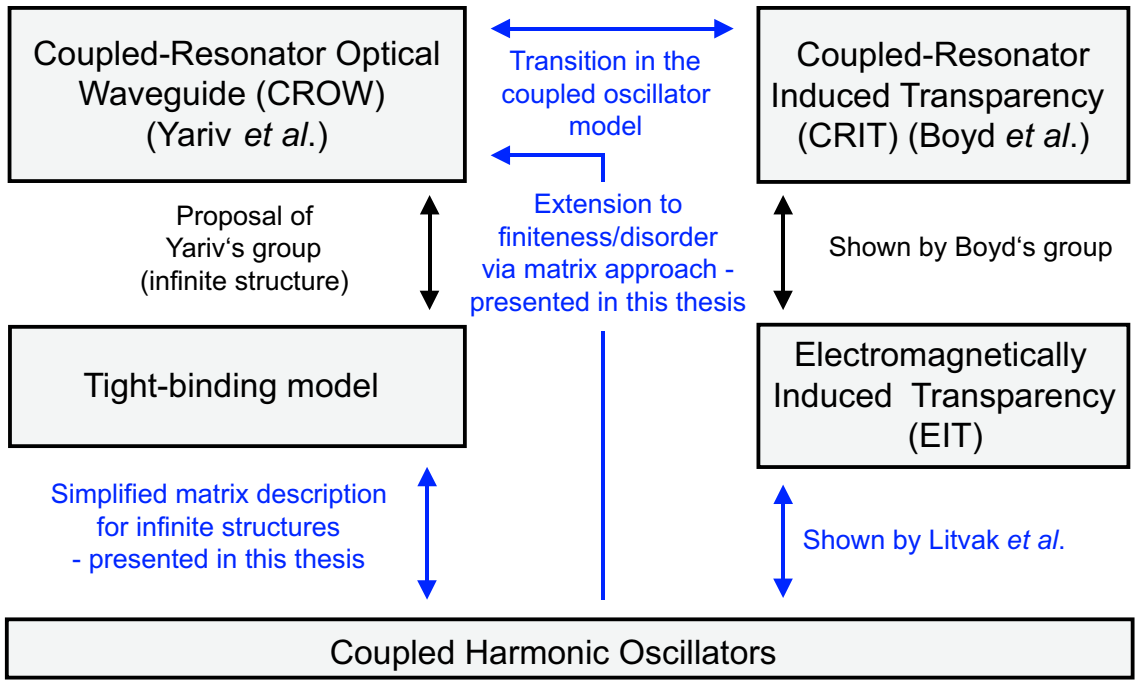

Figure 6.9: Various coupled-resonator effects together with their solid state analogies and their overall relationship with coupled harmonic oscillators.

structure of coupled photonic molecules. This calculation resulted in an expression for the modifications of the coupling terms, which could in turn be mapped onto the related modification of the coupling matrix in the coupled harmonic oscillator model.

On the right-hand side, the proposed concept of coupled resonators with different linewidths has been included. This proposal, worked out by Boyd *et al.* in 2004 and commonly labeled as CRIT (coupled-resonator induced transparency) has been introduced with an solid-state analogy as well, here related to the phenomenon of electromagnetically induced

transparency (EIT). Interestingly, as a second classical analogy for EIT phenomena, the coupling of classical harmonic oscillators has been suggested independently by Litvak *et al.* and Alzar *et al.* in 2002 [Lit02, Alz02]. Therefore, we obtain the analogy between coupled-resonator induced transparency and related transmission phenomena in a set of two coupled harmonic oscillators as well, mediated by their relation to EIT.

Thereby, CRIT phenomena and CROW phenomena can be described by harmonic oscillator models as their common basis. Here, the CROW end of the harmonic oscillator picture represents coupled oscillators with almost equal losses, in contrast to the CRIT side of the harmonic oscillators picture, where extremely different losses are required. One could also view the CROW- and CRIT-like regimes in terms of splittings in solid-state physics, where the CROW-regime of the harmonic oscillator fundament can be regarded as the Rabi-like regime, whereas the CRIT-regime of the model represents the Autler-Townes-like regime. The analogy of coupled two-cavity system with Rabi-splitting has been noted e.g. by Opatrny *et al.* [Opa01] and Smith [Smi04b].

6.6 Entanglement Swapping in Finite Coupled-Resonator Chains

Another possible application might be a slow entanglement transfer in a CROW structure. This will be examined in a three-cavity system as already discussed in subsection 4.0.4. Here, the set of cavity eigenstates can be expressed as

$$[\mathbf{k}_1, \mathbf{k}_2, \mathbf{k}_3] = \left[\begin{pmatrix} \sin(\frac{\pi}{4}) \\ \sin(\frac{\pi}{2}) \\ \sin(\frac{3\pi}{4}) \end{pmatrix}, \begin{pmatrix} \sin(\frac{\pi}{2}) \\ \sin(\pi) \\ \sin(\frac{3\pi}{2}) \end{pmatrix}, \begin{pmatrix} \sin(\frac{3\pi}{4}) \\ \sin(\frac{3\pi}{2}) \\ \sin(\frac{\pi}{4}) \end{pmatrix} \right] \tag{6.33}$$

$$= \left[\begin{pmatrix} \frac{1}{\sqrt{2}} \\ 1 \\ \frac{1}{\sqrt{2}} \end{pmatrix}, \begin{pmatrix} 1 \\ 0 \\ -1 \end{pmatrix}, \begin{pmatrix} \frac{1}{\sqrt{2}} \\ -1 \\ \frac{1}{\sqrt{2}} \end{pmatrix} \right] . \tag{6.34}$$

While, in general, the dispersion relation in finite structures (6.15) does not deviate from Yariv's original proposal for infinite structures (4.8), the slow and coherent propagation of gaussian pulses is not severely affected by the finiteness condition. However, another class of field evolution additionally occurs in finite structures: A type of signal propagation in a CROW we explore now involves all present frequencies derived from the dispersion relation, but exhibits strongly spatially peaked signals in the initial conditions:

Explicitly, the problem is described in a three-resonator system as follows: The light field is initially localized in two resonators at one end only (similar statements hold for the initial excitation of one resonator only, but two excited cavities will offer the use of coherently coupled cavities for slow entanglement transfer). Here, the eigenvectors have been normalized to the situation of two excited cavities, so that the absolute square of any of the vectors results in two. Now, we regard the initial condition, where two cavities

are equally excited at one CROW end. This condition can be expressed as a superposition of the CROW eigenstates noted above as

$$a \cdot \mathbf{k}_1 + b \cdot \mathbf{k}_2 + c \cdot \mathbf{k}_3 = \begin{pmatrix} 1 \\ 1 \\ 0 \end{pmatrix}, \text{ with } (a,b,c) = \left(\frac{1}{2} + \frac{1}{2\sqrt{2}},\ \frac{1}{2},\ -\frac{1}{2} + \frac{1}{2\sqrt{2}} \right) . \quad (6.35)$$

Including the harmonic time dependence for the individual eigenvectors, which obey slightly differing eigenfrequencies, the full time-dependent amplitude vector normalized to the individual cavity fields reads now

$$\mathbf{\Psi}(t) = e^{i\Omega t} \cdot \left[\begin{pmatrix} \frac{1}{2} \\ 0 \\ -\frac{1}{2} \end{pmatrix} + \cos\left(\frac{\kappa}{\sqrt{2}} \Omega t \right) \begin{pmatrix} \frac{1}{2} \\ 1 \\ \frac{1}{2} \end{pmatrix} + i \cdot \sin\left(\frac{\kappa}{\sqrt{2}} \Omega t \right) \begin{pmatrix} \frac{1}{\sqrt{2}} \\ \frac{1}{\sqrt{2}} \\ \frac{1}{\sqrt{2}} \end{pmatrix} \right] . \quad (6.36)$$

This amplitude vector is governed by two frequencies: An oscillating term with the oscillation frequency of a single resonator, and second, a slowly varying term, whose oscillation frequency scales linearly with the interresonator coupling constant κ. As we see from this expression, after a time evolution corresponding to a phase shift of π in the slowly varying amplitude arguments, we end up with a shifted CROW state:

$$\mathbf{\Psi}(t = \pi) = - \begin{pmatrix} 0 \\ 1 \\ 1 \end{pmatrix} . \quad (6.37)$$

This lights up the slow light transfer mechanism in a finite CROW structure. As can be noted from the time evolution after eq. (6.36), the fields in a finite CROW first dephase, and after a phase shift of π the fields undergo a *rephasing* at the other side of the coupled-resonator structure.

This might be — besides slowing down information transfer — of practical use for the field of quantum information processing. The practical usefulness of CROWs for quantum information processing has been theoretically suggested if ref. [Ang04] for the implementation of quantum gates; as I will discuss in this subsection, coupled-resonator optical waveguides could be utilized for slow entanglement transfer in a quantum network as well: Let us now have a closer look at the chosen initial condition in eq. (6.35). As we did already in the bisphere case in subsection 4.0.3, we can treat this initial condition — in the limit of a *single* photon impregnated in the superposition state of the two cavities — as a system of two entangled cavity Fock-states. If a superposition, e.g. a qubit is encoded in such Fock states, the time evolution of a finite CROW transfers the superposition state towards the other end of the CROW, and after a π evolution, the opposite pair of resonators contains — apart from a phase factor common to both cavities — the same entangled superposition state. Explicitly, we end up with an entanglement swapping relation

$$\begin{aligned} & \frac{1}{\sqrt{2}} \left(|1>_{\text{Cavity 1}} |0>_{\text{Cavity 2}} + |0>_{\text{Cavity 1}} |1>_{\text{Cavity 2}} \right) \cdot |0>_{\text{Cavity 3}} \\ \Rightarrow \quad & \frac{1}{\sqrt{2}} |0>_{\text{Cavity 1}} \cdot \left(|1>_{\text{Cavity 2}} |0>_{\text{Cavity 3}} + |0>_{\text{Cavity 2}} |1>_{\text{Cavity 3}} \right) . \end{aligned} \quad (6.38)$$

6.6 Entanglement Swapping in Finite Coupled-Resonator Chains

Another interesting approach for entanglement transfer has been worked out by Christandl *et al.*, which utilizes chains of next-neighbor coupled electron spins [Chr04], and the possibility to obtain quantum state mirrors with spin chains has been theoretically shown [Kar05]. Hence, the scheme presented here can be regarded as a photonic realization of entanglement transfer chains using single photons only in an otherwise passive device.

In general, this type of time evolution in a finite CROW consisting of N resonators can be described in a similar manner. In the following, I would like to briefly discuss the necessary calculation techniques required for the time evolution in a coupled-resonator structure of arbitrary length:

Let us now introduce a vector, which contains the electromagnetic field strength as initial conditions in a linear chain consisting of N resonators, $\mathbf{F}_{\text{initial}}$.

Then, we can express the formation of the initial conditions in terms of the eigenfunctions along a finite CROW:

$$\begin{aligned}\mathbf{F}_{\text{initial}} &= a_1 \cdot \begin{pmatrix} \sin(\frac{1\pi}{N+1}) \\ \sin(\frac{2\pi}{N+1}) \\ \vdots \\ \sin(\frac{N\pi}{N+1}) \end{pmatrix} + a_2 \cdot \begin{pmatrix} \sin(\frac{2\pi}{N+1}) \\ \sin(\frac{4\pi}{N+1}) \\ \vdots \\ \sin(\frac{2\cdot N\pi}{N+1}) \end{pmatrix} + \ldots + a_N \cdot \begin{pmatrix} \sin(\frac{N\pi}{N+1}) \\ \sin(\frac{2\cdot N\pi}{N+1}) \\ \vdots \\ \sin(\frac{N^2\pi}{N+1}) \end{pmatrix} \\ &= a_1 \cdot \mathbf{v}_1 + a_2 \cdot \mathbf{v}_2 + \ldots + a_N \cdot \mathbf{v}_N \ , \end{aligned} \tag{6.39}$$

where the vectors $\mathbf{v}_j$ label the corresponding eigenvectors and the numbers a_j the individual expansion coefficients. This can now be written as a matrix equation as follows:

$$\begin{aligned}\mathbf{F}_{\text{initial}} &= \begin{pmatrix} \sin(\frac{1\cdot\pi}{N+1}) & \sin(\frac{2\cdot\pi}{N+1}) & \ldots & \sin(\frac{N\cdot\pi}{N+1}) \\ \sin(\frac{2\cdot\pi}{N+1}) & \sin(\frac{4\cdot\pi}{N+1}) & \ldots & \sin(\frac{2\cdot N\cdot\pi}{N+1}) \\ \vdots & \vdots & \ddots & \vdots \\ \sin(\frac{N\cdot\pi}{N+1}) & \ldots\ldots\ldots\ldots & & \sin(\frac{N^2\cdot\pi}{N+1}) \end{pmatrix} \cdot \begin{pmatrix} a_1 \\ a_2 \\ \vdots \\ a_N \end{pmatrix} \\ &= \begin{pmatrix} \mathbf{v}_1 & \mathbf{v}_2 & \ldots & \mathbf{v}_N \end{pmatrix} \cdot \begin{pmatrix} a_1 \\ a_2 \\ \vdots \\ a_N \end{pmatrix} \ . \end{aligned} \tag{6.40}$$

From the theory of the diagonalization of matrices we know, that the matrix $\begin{pmatrix} \mathbf{v}_1 & \mathbf{v}_2 & \ldots & \mathbf{v}_N \end{pmatrix}$ constitutes an orthogonal matrix. Thus, we can estimate the expansion coefficients with ease through matrix inversion, where simply a normalization constant of $(N+1)/2$ comes into play:

$$\begin{pmatrix} a_1 \\ a_2 \\ \vdots \\ a_N \end{pmatrix} = \frac{N+1}{2} \cdot \begin{pmatrix} \sin(\frac{1\cdot\pi}{N+1}) & \sin(\frac{2\cdot\pi}{N+1}) & \ldots & \sin(\frac{N\cdot\pi}{N+1}) \\ \sin(\frac{2\cdot\pi}{N+1}) & \sin(\frac{4\cdot\pi}{N+1}) & \ldots & \sin(\frac{2\cdot N\cdot\pi}{N+1}) \\ \vdots & \vdots & \ddots & \vdots \\ \sin(\frac{N\cdot\pi}{N+1}) & \ldots\ldots\ldots\ldots & & \sin(\frac{N^2\cdot\pi}{N+1}) \end{pmatrix} \cdot \mathbf{F}_{\text{initial}} \ . \tag{6.41}$$

The time evolution of a CROW consisting of N resonators can thus be written as

$$\mathbf{F}(t) = \sum_{j=1}^{N} a_j \cdot \mathbf{v_j} \cdot e^{i\Omega_K^N t} \ , \tag{6.42}$$

where the coefficients a_j are determined by eq. (6.41).

7. Summary

The work covered in this thesis is devoted to coupling mechanisms in single microsphere resonators and resonator ensembles doped with semiconductor nanocrystals.

The influence of the elongation of the nanocrystals leading to semiconductor nanorod structures has been investigated. The resulting highly polarized emission identified semiconductor nanorods as ideal artificial dipole emitters. As such, elongated nanocrystals have been used as active light-emitting material with a specific orientation in polymeric microspheres ranging around $R = 2\lambda$ in size. An active mode control has been achieved via a tangential alignment of nanorods on the microsphere surface resulting in pronounced TE field emission and significant TM mode suppression. Hence, these findings demonstrate a clear optimization of the coupling efficiency of excitonic resonances with microsphere modes, which very recently has been applied in light-matter interaction studies [LeT05b].

The interresonator coupling of microsphere modes in various ensembles has been studied in the frame of recently proposed novel optical composite materials like photonic molecules and coupled-resonator optical waveguides and their possible application for molding the flow of light on the micrometer scale. Utilizing spherical nanocrystals as a local field probe, coherent coupling of microresonator fields has been demonstrated initially for a bisphere system, being reflected both in its spectral features and polarization-sensitive mode maps. Symmetry dependent signatures for the light localization of strongly and weakly coupled modes have been obtained, which allow for a convenient and unambiguous determination of coherent interresonator coupling. These symmetry dependent features establish a further criterion for coherent interresonator coupling. The polarization dependence have been determined according to the mode polarization of the single resonator modes of the constituents, leading to an unambiguous assignment of the obtained strongly split modes. The successful extension to one- and two-dimensional geometries and the corresponding modification of light localization strongly supported the tight-binding description of photon modes in coupled resonators.

Due to their weak broadening and the comparatively small split, the weakly coupled modes have been identified as promising candidates for a bottom-up approach to a waveguide structure utilizing coupled microsphere resonators.

Yariv's proposal concerning coupled-resonator optical waveguides (CROWs), originally established for hypothetically infinite systems, has been reexamined for its use in practical, thus finite systems. Unlike the conventional wisdom apparent in current literature, the conclusions derived in Yariv's proposal are applicable to finite systems to a large extent,

if quantization conditions due to finiteness are accounted for. A compact matrix model has been derived from the tight-binding description, which could trace back the CROW problem to the simplified picture of coupled harmonic oscillators. The theoretical analysis indicated the formation of modes with varying oscillator strengths for different resonators in finite coupled-resonator systems. An experimental verification of the predicted splitting has been successfully performed by measurements on a three-sphere system, which consists of the minimum number of resonators leading to an oscillator strength variation.

Yariv's model has been extended towards the case of perturbed finite resonator chains by integrating the photonic molecule picture. This offers a compact calculation method for arbitrary multiresonator systems without the expense of exact field computations. Thus, this approach could be regarded as a complementary approach for a CROW design, for which the properties can be roughly estimated applying this simplified model before performing an exact numerical computation of the whole structure.

With this simple formulation at hand, a connection to another approach for group velocity modification relying on coupled resonators — coupled-resonator induced transparency (CRIT) — has been drawn. Due to a common physical structure of CRIT phenomena and EIT effects, recent proposals for simplified model systems for EIT can be used in turn to model CRIT structures. It turned out, that for both CROW and CRIT effects, coupled harmonic oscillators could be regarded as a common language resulting in an unified description.

A first realization of a CROW structure, formed by a linear array of six microsphere resonators has been presented. The formation of coherently coupled extended multiresonator photon states has been evidenced both by the occurrence of weakly split modes with varying split energies and the application of a polarization-sensitive mode mapping technique. The distinction of the weakly coupled CROW modes from a superposition of simply pairwisely coupled two-sphere states was demonstrated. Investigations covered coupled resonators forming a bent CROW array with an angle of 30 degrees. The spatial localization of light both for the weakly coupled and strongly coupled modes exactly reflected the CROW geometry, which has been established as an additional criterion for CROW formation. A theoretical modeling of a six resonator structure predicted a particular resonator to remain free of intensity. A similar feature has been found in the experiment. This feature should remain even in the case of further modifications of a CROW dispersion in the presence of both higher order and lower order modes. Thus, the formation of Bloch modes with different oscillator strengths might serve as a convenient detection tool for successful CROW mode formation.

As a whole, the findings above demonstrate the successful realization of coupled-resonator structures and constitute a convenient tool box of experimental criteria and a concise and numerically inexpensive calculation frame, which allows for an experimental determination and a direct physical understanding of coherent mode evolution in coupled-resonator geometries. The successful realization and modeling, together with subsequently obtained experimental parameters, suggest an enormous potential of microsphere resonators for

slowing down light in an entirely passive linear optical device.

8. Outlook

For further investigations in this topic, an enhanced and reproducible fine control of the spatial arrangement of microsphere resonators is desired. To achieve this, two experimental methods sound very promising: One way might be the arrangement of spheres into microtemplates, which are directly impregnated into the sample substrate. This could be realized by wet chemical etching of micronsized V-shaped grooves [Har03], [Har05], so called V-grooves, in which the microspheres can be trapped by selfassembly in a drying droplet. The accuracy of the microtemplate could potentially lead to more extended microsphere assemblies. Even more curious arrangements might become feasible. A further impact of this method could concern a detailed study of the contact points between microspheres and the substrate. On a flat substrate, there naturally exists just one contact point, while in a V-groove, the microsphere sits on both sidewalls of the templated substrate. This might give a detailed insight in the optimization of losses due to the substrate.

A second applicable technique would be the use of so called *optical tweezers*. Here, a laser beam is strongly focussed into a spot of nearly resolution limited size. Because of the strong spatial field gradient of the tweezing laser field, a micronsized dielectric particle, ideally a microsphere, experiences a spatial gradient in the radiation pressure when the particle is slightly off-focussed. The resulting total force pulls the microsphere towards the focal point, i.e. *tweezes*. Optical tweezing of microspheres exhibiting sizes of just a few micrometers has been demonstrated and even the transport of individual microspheres over ranges of about 100 μm has been realized recently [Ben05]. This might give the opportunity to realize extended coupled microsphere structures in a directly controllable way. Furthermore, the possibility to move microspheres over large distances on a substrate appears to be useful for an efficient size selective sorting of microspheres, if luminescence spectra could be performed synchronously. Configurations, which open up this possibility, have been very recently reported, e.g. [Li05]. A fine size control is highly desirable for studies extending to disorder phenomena and photonic defect states. Being equally important, this could way enhance the monodispersity of the available microsphere ensemble and lead to quite accurate structures.

Possibly a combination of both methods might be useful, since a highly monodisperse start ensemble would also be attractive for arrangements in V-grooves, and a pre-patterned substrate in turn helps avoiding the agglomeration of multisphere ensembles in an optical tweezer.

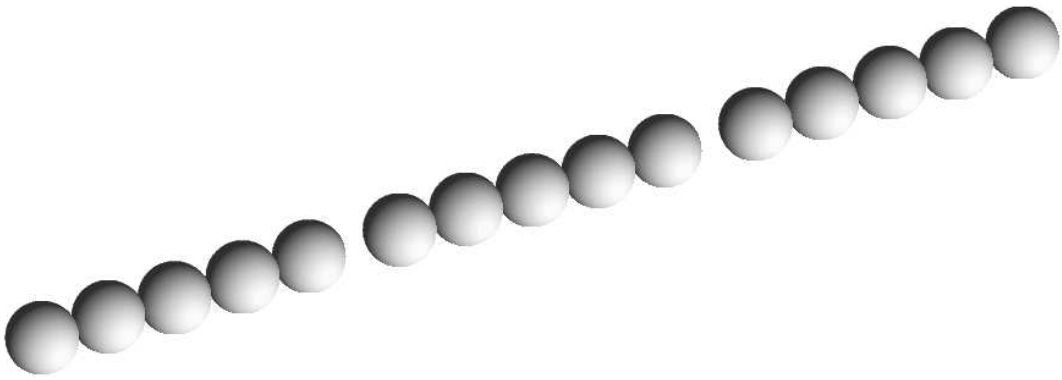

Figure 8.1: Scheme for a purely linear meta-CROW. Since the single resonator chains constitute itself resonators for the Bloch waves, a linear cascade of CROW structures might be feasible.

Furthermore, one could eliminate the residual losses in microsphere resonators applying different methods of coating. Spherical Bragg-reflectors grown in an onion-like fashion onto the microsphere surface have been theoretically discussed with respect to highly efficient optical confinement [Kal01], however, an experimental realization is still missing.

One complementary possibility to evaluate the transmission characteristics of coupled-resonator waveguides would be the utilization of a time-resolved SNOM technique, as has been applied recently for the pulse propagation in waveguides [Bal01], dispersive media [Ger03], and microresonators [Ger04]. Here, the investigation could be extended to explore dispersion relations in the direct time-regime of coupled-microresonator waveguides.

For the application direction, one could also explore the tuning possibility via nonlinear resonator materials or dopants [Mae05] and check for the transmission around ultra-sharp angles.

Possibly, the formalism developed here could be extended to the coupling of surface plasmons in arrays of metallic nanodots. Such arrays are currently debated for guiding light in nanometer dimensions, see e.g. [Cit05], [Ata04].

Additionally, one other interesting application would be the modification of spontaneous emission of active emitters incorporated into an extended long-range CROW, as has been recently discussed in theory [Yan04b], allowing for a modification with external tuning possibilities. This could be viewed as an extension to the so-called Purcell effect [Pur46], which has been shown for single cavities, see e.g. ref. [Art01b].

One more remote goal would be to investigate the question, whether and how CROW structures can be scaled to metastructures: As suggested by Yariv in his 1999 paper, one could build ring resonators from CROW lines. For example, one could not only think of conventional resonators as building blocks for a CROW construction, but merely of ring resonators consisting of a CROW structure itself. The impact of this appears to be a drastically reduced eigenfrequency, and thus to a multiplication of the CROW effect, which appears to be nearly impossible to achieve in a natural solid state. As turns out from the

discussion in chapter 6, even purely linear arrays do already constitute a *supercavity* with the ability to slow down light. Therefore, the construction of scaled coupled-resonator optical waveguides could possibly be performed using strictly linear geometries, which might allow to keep size requirements small, when the coupling conditions are solely engineered by interresonator distances. This proposal for a modified *meta-CROW* is depicted in fig. 8.1.

Bibliography

[Alt05a] H. Altug and J. Vučković: *Experimental demonstration of the slow group velocity of light in two-dimensional coupled photonic crystal microcavity arrays*, Appl. Phys. Lett. **86** (11), 111102 (March 2005)

[Alt05b] H. Altug and J. Vučković: *Polarization control and sensing with two-dimensional coupled photonic crystal microcavity arrays*, Opt. Lett. **30** (9), 982–984 (May 2005)

[Alz02] C. L. G. Alzar, M. A. G. Martinez, and P. Nussenzveig: *Classical analog of electromagnetically induced transparency*, Am. J. Phys. **70** (1), 37–41 (January 2002)

[And00] P. Andrew and W. L. Barnes: *Förster Energy Transfer in an Optical Microcavity*, Science **290**, 785–788 (October 2000)

[Ang04] D. G. Angelakis, M. F. Santos, V. Yannopapas, and A. Ekert: *Quantum computation in photonic crystals*, arXiv:quant-ph/0410189v4 (November 2004)

[Arn97] S. Arnold, S. Holler, N. L. Goddard, and G. Griffel: *Cavity-mode selection in spontaneous emission from oriented molecules in a microparticle*, Opt. Lett. **22** (19), 1452–1454 (October 1997)

[Arn03] S. Arnold, M. Khoshsima, I. Teraoka, S. Holler, and F. Vollmer: *Shift of whispering-gallery modes in microspheres by protein adsoption*, Opt. Lett. **28** (4), 272–274 (February 2003)

[Art01a] M. V. Artemyev, U. Woggon, and R. Wannemacher: *Photons confined in hollow microspheres*, Appl. Phys. Lett. **78** (8), 1032–1034 (February 2001)

[Art01b] M. V. Artemyev, U. Woggon, R. Wannemacher, H. Jaschinski, and W. Langbein: *Light Trapped in a Photonic Dot: Microspheres Act as a Cavity for Quantum Dot Emission*, Nano Letters **1** (6), 309–314 (2001)

[Art02] M. V. Artemyev: *private communication* (2002)

[Art03a] M. Artemyev, B. Möller, and U. Woggon: *Unidirectional Alignment of CdSe Nanorods*, Nano Letters **3** (4), 509–512 (April 2003)

Bibliography

[Art03b] M. V. Artemyev: *private communication* (2003)

[Ash76] N. W. Ashcroft and N. D. Mermin: *Solid State Physics*, Holt, Rinehart and Winston (1976)

[Ast04] V. N. Astratov, J. P. Franchak, and S. P. Ashili: *Optical coupling and transport phenomena in chains of spherical dielectric microresonators with size disorder*, Appl. Phys. Lett. **85** (23), 5508–5510 (December 2004)

[Ata04] T. Atay, J.-H. Song, and A. V. Nurmikko: *Strongly Interacting Plasmon Nanoparticle Pairs: From Dipole-Dipole Interaction to Conductively Coupled Regime*, Nano Letters **4** (9), 1627–1631 (September 2004)

[Bal01] M. L. M. Balistreri, H. Gersen, J. P. Korterik, L. Kuipers, and N. F. van Hulst: *Tracking Femtosecond Laser Pulses in Space and Time*, Science **294** (5544), 1080–1082 (2001)

[Bán93] L. Bányai and S. W. Koch: *Semiconductor Quantum Dots*, volume 2 of *World Scientific Series on Atomic, Molecular and Optical Physics*, World Scientific Publishing Co. Pte. Ltd. (1993)

[Bar96] M. D. Barnes, C.-Y. Kung, W. B. Whitten, J. M. Ramsey, S. Arnold, and S. Holler: *Fluorescence of Oriented Molecules in a Microcavity*, Phys. Rev. Lett. **76** (21), 3931–3934 (May 1996)

[Bar03] H. Barnum, E. Knill, G. Ortiz, and L. Viola: *Generalization of entanglement based on coherent states and convex sets*, Phys. Rev. A **68** (3), 032308 (September 2003)

[Bay98] M. Bayer, T. Gutbrod, J. P. Reithmaier, A. Forchel, T. L. Reinecke, P. A. Knipp, A. A. Dremin, and V. D. Kulakovskii: *Optical Modes in Photonic Molecules*, Phys. Rev. Lett. **81** (12), 2582–2585 (September 1998)

[Bay00] M. Bayindir, B. Temelkuran, and E. Ozbay: *Tight-Binding Description of the Coupled Defect Modes in Three-Dimensional Photonic Crystals*, Phys. Rev. Lett. **84** (10), 2140–2143 (March 2000)

[Ben05] O. Benson and F. Boczianowski: *Trapping and manipulating dielectric nanoparticles on Photonic Crystals using an optical tweezer*, Contribution HL 37.9, Spring Meeting of the German Physical Society, Berlin (2005)

[Bir66] R. R. Birss: *Symmetry in Magnetism*, volume 3 of *Series of Monographs on Selected Topics in Solid State Physics*, North-Holland Publishing Company — Amsterdam (1966)

[Boh96] C. F. Bohren and D. R. Huffman: *Absorption and Scattering of Light by Small Particles*, John Wiley & Sons (1996)

[Boh98] C. F. Bohren and D. R. Huffman: *BHMIE*, modifiziert von B. T. Draine, C-Übersetzung durch P. J. Flatau, `http://atol.ucsd.edu/~pflatau/scatlib/` (1998)

[Bor01] M. A. Borchers, C. Esen, and G. Schweiger: *Cascade lasing with spherical microparticles*, Opt. Lett. **26** (6), 346–348 (March 2001)

[Bos04] A. R. Bosco de Magalhães, S. G. Mokarzel, M. C. Nemes, and M. O. Terra Cunha: *Decay rate and decoherence control in coupled dissipative cavities*, arXiv:quant-ph/0405022v1 (May 2004)

[Bri53] L. Brillouin: *Wave propagation in periodic structures*, Dover Publications, Inc. (1953)

[Buc03] J. R. Buck and H. J. Kimble: *Optimal sizes of dielectric microspheres for cavity QED with strong coupling*, Phys. Rev. A **67** (3), 033806 (March 2003)

[Cas96] D. Cassagne, C. Jouanin, and D. Bertho: *Hexagonal photonic-band-gap structures*, Phys. Rev. B **53** (11), 7134–7142 (March 1996)

[Cha96] R. K. Chang and A. J. Campillo (editors): *Optical Processes in Microcavities*, volume 3 of *Advanced Series in Applied Physics*, World Scientific, Singapore (1996)

[Che76] H. Chew, P. J. McNulty, and M. Kerker: *Model for Raman and fluorescent scattering by molecules embedded in small particles*, Phys. Rev. A **13** (1), 396–404 (January 1976)

[Che03] Z. Chen, A. Taflove, and V. Backman: *Equivalent volume-averaged light scattering behavior of randomly inhomogeneous dielectric spheres in the resonant range*, Opt. Lett. **28** (10), 765–767 (May 2003)

[Che04] Y. Chen and S. Blair: *Nonlinearity enhancement in finite coupled-resonator slow-light waveguides*, Opt. Express **12** (15), 3353–3366 (July 2004)

[Chi87a] S. C. Ching, H. M. Lai, and K. Young: *Dielectric microspheres as optical cavities: Einstein A and B coefficients and level shift*, J. Opt. Soc. Am. B **4** (12), 2004–2009 (December 1987)

[Chi87b] S. C. Ching, H. M. Lai, and K. Young: *Dielectric microspheres as optical cavities: thermal spectrum and density of states*, J. Opt. Soc. Am. B **4** (12), 1995–2003 (December 1987)

[Chi96] E. S.-C. Ching, P.-T. Leung, and K. Young: *The Role of Quasinormal Modes*, in R. K. Chang and A. J. Campillo (editors), *Optical Processes in Microcavities*, volume 3 of *Advanced Series in Applied Physics*, World Scientific, Singapore (1996)

Bibliography

[Chr04] M. Christiandl, N. Datta, A. Ekert, and A. J. Landahl: *Perfect State Transfer in Quantum Spin Networks*, Phys. Rev. Lett. **92** (18), 187902 (May 2004)

[Cit05] D. S. Citrin: *Subwavelength nanoplasmonic ring resonators*, J. Opt. Soc. Am. B **22** (8), 1763 (August 2005)

[Deb09] P. Debye: *Der Lichtdruck auf Kugeln von beliebigem Material*, Annalen der Physik **30**, 57 (1909)

[Den05] S. Deng and W. Cai: *Discontinuous spectral element method modeling of optical coupling by whispering gallery modes between microcylinders*, J. Opt. Soc. Am. A **22** (5), 952 (May 2005)

[Din04] W.-Q. Ding, L.-X. Chen, and S.-T. Liu: *Finite size effects on one dimensional coupled cavity optical waveguides*, Opt. Commun. **242**, 437–444 (2004)

[Fan01] X. Fan, M. C. Lonergan, Y. Zhang, and H. Wang: *Enhanced spontaneous emission from semiconductor nanocrystals embedded in whispering gallery optical microcavities*, Phys. Rev. B **64** (11), 115310 (August 2001)

[Frö05] D. Fröhlich, G. Dasbach, G. B. H. von Högersthal, M. Bayer, R. Klieber, D. Suter, and H. Stolz: *High resolution spectroscopy of yellow 1S excitons in Cu_2O*, Solid State Commun. **134**, 139–142 (2005)

[Gay01] B. Gayral, J.-M. Gérard, B. Sermage, A. Lemaître, and C. Dupuis: *Time-resolved probing of the Purcell effect for InAs quantum boxes in GaAs microdisks*, Appl. Phys. Lett. **78** (19), 2828–2830 (May 2001)

[Gér01] J. M. Gérard and B. Gayral: *InAs quantum dots: artificial atoms for solid-state cavity-quantum electrodynamics*, Physica E **9**, 131–139 (2001)

[Ger03] H. Gersen, J. P. Korterik, N. F. van Hulst, and L. Kuipers: *Tracking ultrashort pulses through dispersive media: Experiment and theory*, Phys. Rev. E **68**, 026604 (August 2003)

[Ger04] H. Gersen, D. J. W. Klunder, J. P. Korterik, A. Driessen, N. F. van Hulst, and L. Kuipers: *Propagation of a femtosecond pulse in a microresonator visualized in time*, Opt. Lett. **29** (11), 1291–1293 (June 2004)

[Gma98] C. Gmachl, F. Capasso, E. E. Narimanov, J. U. Nöckel, A. D. Stone, J. Faist, D. L. Sivco, and A. Y. Cho: *High-Power Directional Emission from Microlasers with Chaotic Resonantors*, Science **280**, 1556 (1998)

[Gor99] M. L. Gorodetsky and V. S. Ilchenko: *Optical microsphere resonators: optimal coupling to high-Q whispering-gallery modes*, J. Opt. Soc. Am. B **16** (1), 147–154 (January 1999)

[Gri03] D. G. Grier: *A revolution in optical manipulation*, Nature **424**, 810–816 (August 2003)

[Guv05] K. Guven and E. Ozbay: *Coupling and phase analysis of cavity structures in two-dimensional photonic crystals*, Phys. Rev. B **71**, 085108 (February 2005)

[Han01] M. Han, X. Gao, J. Z. Su, and S. Nie: *Quantum-dot-tagged microbeads for multiplexed optical coding of biomolecules*, Nature Biotechnol. **19**, 631–635 (July 2001)

[Hap03] T. D. Happ, M. Kamp, A. Forchel, J.-L. Gentner, and L. Goldstein: *Two-dimensional photonic crystal coupled-defect laser diode*, Appl. Phys. Lett. **82** (1), 4–6 (January 2003)

[Har03] Y. Hara, T. Mukaiyama, K. Takeda, and M. Kuwata-Gonokami: *Photonic molecule lasing*, Opt. Lett. **28** (24), 2437–2439 (December 2003)

[Har05] Y. Hara, T. Mukaiyama, K. Takeda, and M. Kuwata-Gonokami: *Heavy Photon States in Photonic Chains of Resonantly Coupled Cavities with Supermonodispersive Microspheres*, Phys. Rev. Lett. **94** (20), 203905 (May 2005)

[Hau99] L. V. Hau, S. E. Harris, Z. Dutton, and C. H. Behroozi: *Light speed reduction to 17 metres per second in an ultracold atomic gas*, Nature **397**, 594 (February 1999)

[Hee02] J. E. Heebner, R. W. Boyd, and Q.-H. Park: *SCISSOR solitons and other novel propagation effects in microresonator-modified waveguides*, J. Opt. Soc. Am. B **19** (4), 722–731 (April 2002)

[Hee04] J. E. Heebner, P. Chak, S. Pereira, J. E. Sipe, and R. W. Boyd: *Distributed and localized feedback in microresonator sequences for linear and nonlinear optics*, J. Opt. Soc. Am. B **21** (10), 1818–1832 (October 2004)

[Hil96] S. C. Hill, H. I. Saleheen, M. D. Barnes, W. B. Whitten, and J. M. Ramsey: *Modeling fluorescence collection from single molecules in microspheres: effects of position, orientation, and frequency*, Appl. Opt. **35** (31), 6278–6288 (November 1996)

[Hil04] M. T. Hill, H. J. S. Dorren, T. de Vries, X. J. M. Leijtens, J. H. den Besten, B. Smalbrugge, Y.-S. Oel, H. Binsma, G.-D. Khoe, and M. K. Smit: *A fast low-power optical memory based on coupled micro-ring lasers*, Nature **432**, 206–209 (November 2004)

[Hin96] M. A. Hines and P. Guyot-Sionnest: *Synthesis and Characterization of Strongly Luminescing ZnS-Capped CdSeNanocrystals*, J. Phys. Chem. **100** (2), 468–471 (1996)

Bibliography

[Hu01] J. Hu, L. Li, W. Yang, L. Manna, L. Wang, and A. P. Alivisatos: *Linearly Polarized Emission from Colloidal Semiconductor Quantum Rods*, Science **292** (5524), 2060–2063 (June 2001)

[Iba90] Ibach and Lüth: *Festkörperphysik: Einführung in die Grundlagen*, Springer-Verlag Berlin Heidelberg, 3. edition (1990)

[Joh87] S. John: *Strong Localization of Photons in Certain Disordered Dielectric Superlattices*, Phys. Rev. Lett. **58** (23), 2486–2489 (June 1987)

[Kal01] M. A. Kaliteevski, S. Brand, R. A. Abram, V. V. Nikolaev, M. V. Maximov, C. M. Sotomayor Torres, and A. V. Kavokin: *Electromagnetic theory of the coupling of zero-dimensional exciton and photon states: A quantum dot in a spherical microcavity*, Phys. Rev. B **64**, 115305 (2001)

[Kar05] P. Karbach and J. Stolze: *Spin chains as perfect quantum state mirrors*, Phys. Rev. A **72** (3), 030301(R) (September 2005)

[Kaz04] M. Kazes, D. Y. Lewis, and U. Banin: *Method for preparation of semiconductor quantum-rod lasers in a cylindrical microcavity*, Adv. Funct. Mater. **14** (10), 957–962 (October 2004)

[Khu05] J. B. Khurgin: *Optical buffers based on slow light in electromagnetically induced transparent media and coupled resonator structures: comparative analysis*, J. Opt. Soc. Am. B **22** (5), 1062–1074 (May 2005)

[Kim04] Y. S. Kim and M. E. Noz: *Harmonic Oscillators as Bridges between Theories: Einstein, Dirac, and Feynman*, AIP Conference Proceedings Vol. 755, p. 61, ISIS International Symposium on Interdisciplinary Science (Louisiana, USA) (October 2004)

[Kit96] C. Kittel: *Einführung in die Festkörperphysik*, R. Oldenbourg Verlag München, 11. edition (1996)

[Kli95] C. F. Klingshirn: *Semiconductor Optics*, Springer Verlag (1995)

[Lab99] D. Labilloy, H. Benisty, C. Weisbuch, T. F. Krauss, C. J. M. Smith, R. M. D. L. Rue, D. Cassagne, and C. Jourmin: *Measuring the Optical Properties of Two-Dimensional Photonic Crystals in the Near Infrared*, in *Confined Photon Systems*, volume 531 of *Lecture Notes in Physics*, Springer-Verlag (1999)

[Lac03] S. Lacey, H. Wang, D. H. Foster, and J. U. Nöckel: *Directional Tunneling Escape from Nearly Spherical Optical Resonators*, Phys. Rev. Lett. **91** (3), 033902 (July 2003)

[LB82] Landolt-Börnstein: *Neue Serie, Gruppe III*, in *Zahlenwerte und Funktionen aus Naturwissenschaft und Technik*, volume 17 b, Springer-Verlag, Berlin, Heidelberg, New York (1982)

[Lee00] H.-W. Lee and J. Kim: *Quantum teleportation and Bell's inequality using single-particle entanglement*, Phys. Rev. A **63** (1), 012305 (December 2000)

[LeT05a] N. LeThomas, E. Herz, O. Schöps, U. Woggon, and M. V. Artemyev: *Exciton Fine Structure in Single CdSe Nanorods*, Phys. Rev. Lett. **94**, 016803 (January 2005)

[LeT05b] N. LeThomas, O. Schöps, U. Woggon, M. V. Artemyev, M. Kazes, and U. Banin: *Cavity QED with semiconductor nanocrystals*, Phys. Rev. (submitted) (July 2005)

[Li04] S.-B. Li and J.-B. Xu: *Quantum entanglement and Bell violation of two coupled cavity fields in a dissipative environment*, J. Opt. B **6**, 373 (June 2004)

[Li05] P. Li, K. Shi, and Z. Liu: *White Light Supercontinuum Optical Tweezer*, Contribution CFN 1, CLEO/QELS Conference, Baltimore (2005)

[Lit02] A. G. Litvak and M. D. Tokman: *Electromagnetically Induced Transparency in Ensembles of Classical Oscillators*, Phys. Rev. Lett. **88** (9), 095003 (February 2002)

[Mac01] M. P. MacDonald, L. Paterson, W. Sibbett, K. Dholakia, and P. E. Bryant: *Trapping and manipulation of low-index particles in a two-dimensional interferometric optical trap*, Opt. Lett. **26** (12), 863–865 (June 2001)

[Mae05] B. Maes, P. Bienstman, and R. Baets: *Bloch modes and self-localized waveguides in nonlinear photonic crystals*, J. Opt. Soc. Am. B **22** (3), 613 (March 2005)

[Man02] L. Manna, E. C. Scher, and A. P. Alivisatos: *Shape Control of Colloidal Semiconductor Nanocrystals*, J. Cluster Sci. **13** (4), 521–532 (December 2002)

[Man03] V. N. Manoharan, M. T. Elsesser, and D. J. Pine: *Dense Packing and Symmetry in Small Clusters of Microspheres*, Science **301**, 483–487 (July 2003)

[Mat05] A. B. Matsko, D. V. Strekalov, and L. Maleki: *On the dynamic range of optical delay lines based on coherent atomic media*, Opt. Express **13** (6), 2210–2223 (March 2005)

[Mel02] A. Melloni and M. Martinelli: *Synthesis of Direct-Coupled-Resonators Bandpass Filters for WDM Systems*, J. Lightwave Technol. **20** (2), 296–303 (February 2002)

[Mie08] G. Mie: *Beiträge zur Optik trüber Medien, speziell kolloidaler Metalllösungen*, Annalen der Physik **25** (IV. Folge), 377–445 (1908)

[Möl01] B. Möller: *Optische Spektroskopie an Halbleiter-Mikroresonatoren*, Diplomarbeit am Fachbereich Physik, Universität Dortmund (November 2001)

Bibliography

[Möl02] B. Möller, M. V. Artemyev, U. Woggon, and R. Wannemacher: *Mode identification in spherical microcavities doped with quantum dots*, Appl. Phys. Lett. **80** (18), 3253–3255 (May 2002)

[Möl03] B. Möller, U. Woggon, M. V. Artemyev, and R. Wannemacher: *Mode control by nanoengineering light emitters in spherical microcavities*, Appl. Phys. Lett. **83** (13), 2686–2688 (September 2003)

[Möl04] B. M. Möller, M. V. Artemyev, U. Woggon, and R. Wannemacher: *Photonic molecules doped with semiconductor nanocrystals*, Phys. Rev. B **70** (11), 115323 (September 2004)

[Mol05a] S. Molchanov and B. Vainberg: *Slowing down and reflection of waves in truncated periodic media*, arXiv:math.CA/0503075v1 (March 2005)

[Möl05b] B. M. Möller, M. V. Artemyev, and U. Woggon: *Coupled-resonator optical waveguides doped with nanocrystals*, Opt. Lett. **30** (16), 2116 (August 2005)

[Muk99] T. Mukaiyama, K. Takeda, H. Miyazaki, Y. Jimba, and M. Kuwata-Gonokami: *Tight-Binding Photonic Molecule Modes of Resonant Bispheres*, Phys. Rev. Lett. **82** (32), 4623–4626 (June 1999)

[Mur93] C. B. Murray, D. J. Norris, and M. G. Bawendi: *Synthesis and Characterization of Nearly Monodisperse CdE (E = S, Se, Te) Semiconductor Nanocrystallites*, J. Am. Chem. Soc **115**, 8706–8715 (1993)

[Nob04] T. Nobis, E. M. Kaidashev, A. Rahm, M. Lorenz, and M. Grundmann: *Whispering Gallery Modes in Nanosized Dielectric Resonators with Hexagonal Cross Section*, Phys. Rev. Lett. **93** (10), 103903 (September 2004)

[Oka03] H. Okamoto, M. Haraguchi, M. Fukui, and T. Okamoto: *Optical Filtering by Microring Resonators*, Jpn. J. Appl. Phys. **42**, 2692–2698 (2003)

[Ols04] Y. K. Olsson, G. Chen, R. Rapaport, D. T. Fuchs, V. C. Sundar, J. S. Steckel, M. G. Bawendi, A. Aharoni, and U. Banin: *Fabrication and optical properties of polymeric waveguides containing nanocrystalline quantum dots*, Appl. Phys. Lett. **85** (19), 4469 (November 2004)

[Opa01] T. Opatrný and D.-G. Welsch: *Coupled cavities for enhancing the cross-phase-modulation in electromagnetically induced transparency*, Phys. Rev. A **64**, 023805 (July 2001)

[Pal03a] P. Palinginis, S. Tavenner, M. Lonergan, and H. Wang: *Spectral hole burning and zero phonon linewidth in semiconductor nanocrystals*, Phys. Rev. B **67**, 201307(R) (2003)

[Pal03b] G. T. Paloczi, Y. Huang, A. Yariv, and S. Mookherjea: *Polymeric Mach-Zehnder interferometer using serially coupled microring resonators*, Opt. Express **11** (21), 2666–2671 (October 2003)

[Pal05] P. Palinginis, S. Crankshaw, F. Sedgwick, E.-T. Kim, M. Moewe, C. J. Chang-Hasnain, H. Wang, and S.-L. Chuang: *Ultraslow light (<200 m/s) propagation in a semiconductor nanostructure*, Appl. Phys. Lett. **87** (17), 171102 (October 2005)

[Pen00] X. Peng, L. Manna, W. Yang, J. Wickham, E. Scher, A. Kadavanich, and A. P. Alivisatos: *Shape control of CdSe nanocrystals*, Nature **404**, 59–61 (March 2000)

[Pet05] E. Peter, P. Senellart, D. Martrou, A. Lemaître, J. Hours, J.-M. Gérard, and J. Bloch: *Exciton-Photon Strong-Coupling Regime for a Single Quantum Dot Embedded in a Microcavity*, Phys. Rev. Lett. **95** (6), 067401 (August 2005)

[Pey93] N. Peyghambarian, S. W. Koch, and A. Mysyrowicz: *Introcuction to semiconductor optics*, Prentice-Hall, Inc. (1993)

[Poo04a] J. K. S. Poon, Y. Huang, G. T. Paloczi, A. Yariv, C. Zhang, and L. R. Dalton: *Wide-range tuning of polymer microring resonators by the photobleaching of CLD-1 chromophores*, Opt. Lett. **29** (22), 2584 (November 2004)

[Poo04b] J. K. S. Poon, J. Scheuer, S. Mookherjea, G. T. Paloczi, Y. Huang, and A. Yariv: *Matrix analysis of microring coupled-resonator optical waveguides*, Opt. Express **12** (1), 90–103 (January 2004)

[Poo04c] J. K. S. Poon, J. Scheuer, Y. Xu, and A. Yariv: *Designing coupled-resonator optical waveguide delay lines*, J. Opt. Soc. Am. B **21** (9), 1665–1673 (September 2004)

[Pur46] E. M. Purcell: *Spontaneous Emission Probabilities at Radio Frequencies*, Phys. Rev. **69**, 681 (1946)

[Rak03] Y. P. Rakovich, L. Yang, E. M. McCabe, J. F. Donegan, T. Perova, A. Moore, N. Gaponik, and A. Rogach: *Whispering gallery mode emission from a composite system of CdTe nanocrystals and a spherical microcavity*, Semicond. Sci. Technol. **18**, 914–918 (August 2003)

[Réc04] S. Réculusa, C. Mingotaud, E. Bourgeat-Lami, E. Duguet, and S. Ravaine: *Synthesis of Daisy-Shaped and Multipod-like Silica/Polystyrene Nanocomposites*, Nano Letters **4** (9), 1677–1682 (July 2004)

[Rei04] J. P. Reithmaier, G. Sęk, A. Löffler, C. Hofmann, S. Kuhn, S. Reitzenstein, L. V. Keldysh, V. D. Kulakovskii, T. L. Reinecke, and A. Forchel: *Strong coupling in a single quantum dot-semiconductor microcavity system*, Nature **432**, 197–200 (November 2004)

Bibliography

[Rol00] G. Roll and G. Schweiger: *Geometrical optics model of Mie resonances*, J. Opt. Soc. Am. A **17** (7), 1301–1311 (July 2000)

[Sha04] A. Shabaev and A. L. Efros: *1D Exciton Spectroscopy of Semiconductor Nanorods*, arXiv:cond-mat/0403768v1 (March 2004)

[Shi01] K. Shima, R. Omori, and A. Suzuki: *High-Q concentrated directional emission from egg-shaped asymmetric resonant cavities*, Opt. Lett. **26** (11), 795–797 (June 2001)

[Smi04a] D. D. Smith, H. Chang, K. A. Fuller, A. T. Rosenberger, and R. W. Boyd: *Coupled-resonator-induced transparency*, Phys. Rev. A **69**, 063804 (June 2004)

[Smi04b] D. D. Smith and H. Chank: *Coherence Phenomena in Coupled Optical Resonators*, J. Mod. Opt. **51** (16-18), 2503–2513 (December 2004)

[Ste98] N. Stefanou and A. Modinos: *Impurity bands in photonic insulators*, Phys. Rev. B **57** (19), 12127–12133 (May 1998)

[Tal01] D. V. Talapin, A. L. Rogach, A. Kornowski, M. Haase, and H. Weller: *Highly Luminescent Monodisperse CdSe and CdSe/ZnS Nanocrystals Synthesized in a Hexadecylamine-Trioctylphosphine Oxide-Trioctylphosphine Mixture*, Nano Lett. **1** (4), 207–211 (March 2001)

[Uet86] M. Ueta, H. Kanzaki, K. Kobayashi, Y. Toyozawa, and E. Hanamura: *Excitonic Processes in Solids*, volume 60 of *Springer Series in Solid-State Sciences*, Springer-Verlag (1986)

[Ush99] J. Ushida, T. Ohta, and K. Cho: *Radiative Lifetime of an Atom In- and Outside of Planar/Spherical Dielectrics*, J. Phys. Soc. Jap. **68** (7), 2439–2443 (July 1999)

[vK01] W. von Klitzing, R. Long, V. S. Ilchenko, J. Hare, and V. Lefèvre-Seguin: *Frequency tuning of the whispering-gallery modes of silica microspheres for cavity quantum electrodynamics and spectroscopy*, Opt. Lett. **26** (3), 166–168 (February 2001)

[Wan04a] D. Wang and H. Möhwald: *Template-directed colloidal self-assembly — the route to 'top-down' nanochemical engineering*, J. Mater. Chem. **14**, 459–468 (2004)

[Wan04b] R. Wannemacher: *private communication* (2004)

[War04] F. Warken and H. Giessen: *Fast profile measurement of micrometer-sized tapered fibers with better than 50-nm accuracy*, Opt. Lett. **29** (15), 1727–1729 (August 2004)

[Wog97] U. Woggon: *Optical Properties of Semiconductor Quantum Dots*, volume 136 of *Springer Tracts in Modern Physics*, Prentice-Hall, Inc. (1997)

[Wog03] U. Woggon, R. Wannemacher, M. V. Artemyev, B. Möller, N. LeThomas, V. Anikeyev, and O. Schöps: *Dot-in-a-dot: electronic and photonic confinement in all three dimensions*, Appl. Phys. B **77**, 469–484 (September 2003)

[Wos03] K. Wostyn, Y. Zhao, B. Yee, K. Clays, A. Persoons, G. de Schaetzen, and L. Hellemans: *Optical properties and orientation of arrays of polystyrene spheres deposited using convective self-assambly*, J. Chem. Phys. **118** (23), 10752–10757 (June 2003)

[Xia00] Y. Xia, B. Gates, Y. Yin, and Y. Lu: *Monodispersed Colloidal Spheres: Old Materials with New Applications*, Adv. Mater. **12** (10), 693–713 (2000)

[Yab87] E. Yablonovitch: *Inhibited Spontaneous Emission in Solid-State Phyics and Electronics*, Phys. Rev. Lett. **58** (20), 2059–2062 (May 1987)

[Yam00] Y. Yamamoto, T. Tassone, and H. Cao: *Semiconductor Cavity Quantum Electrodynamics*, volume 169 of *Springer Tracts in Modern Physics*, Springer-Verlag (2000)

[Yan04a] M. F. Yanik and S. Fan: *Time Reversal of Light with Linear Optics and Modulators*, Phys. Rev. Lett. **93** (17), 173903 (October 2004)

[Yan04b] V. Yannopapas: *Spontaneous emission through heavy photon bands*, J. Opt. B **6**, 283–288 (April 2004)

[Yar99] A. Yariv, Y. Xu, R. K. Lee, and A. Scherer: *Coupled-resonator optical waveguide: a proposal and analysis*, Opt. Lett. **24** (11), 711–713 (June 1999)

[Ye04] Y.-H. Ye, J. Ding, D. Y. Jeong, I. C. Khoo, and Q. M. Zhang: *Finite-size effect on one-dimensional coupled-resonator optical waveguides*, Phys. Rev. E **69**, 056604 (May 2004)

[Yin01] Y. Yin and Y. Xia: *Self-Assembly of Monodispersed Spherical Colloids into Complex Aggregates with Well-Definded Sizes, Shapes, and Structures*, Adv. Mater. **13** (4), 267–271 (February 2001)

[Yos04] T. Yoshie, A. Scherer, J. Hendrickson, G. Khitrova, H. M. Gibbs, G. Rupper, C. Ell, O. B. Shchekin, and D. G. Deppe: *Vacuum Rabi splitting with a single quantum dot in a photonic crystal nanocavity*, Nature **432**, 200–203 (November 2004)

[Zho03] X. Zhou, S. Li, and K. Stamnes: *Geometrical-optics code for computing the optical properties of large dielectric spheres*, Appl. Opt. **42** (21), 4295–4306 (July 2003)

Acknowledgements

This work has been made possible with help and support from many colleagues, friends and my family:

First of all, I want to thank Prof. Dr. Ulrike Woggon for her scientific guidance, her support and encouragement. Thank you as well for the opportunity to work on this fascinating subject and for various possibilities to communicate the results.

I cordially thank Prof. Dr. Klaus Wille for kindly accepting to referee this thesis.

I gratefully thank Drs. Michail Artemyev and Yuri Fedutik for the preparation of excellent samples, for many scientific discussions and for the open and kind working atmosphere in the labs.

I would like to thank Priv.-Doz. Dr. Reinhold Wannemacher for kindly discussing his MMP calculations.

I would like to thank all former and current members of the group EII, especially Dr. Stephan Schneider, Dr. Nicolas LeThomas, Dr. Vasili Temnov, Oliver Schöps, Vitali Anikeyev, Sabine Dommers, Dr. Andrew Ebbens and Dr. Marco Allione for joyful scientific discussions, helpful advice and support, and the nice atmosphere.

I gratefully thank Klaus Wiegers, Frank Plückebaum, Dirk Schemionek and Gisela Pike for excellent technical support and help during sample preparation.

Concerning technical issues, the mechanical workshop team around Susanne Fricke, the teams of the electronic workshop and the construction office kindly shared their expertise and provided many efficient solutions, for which I am really grateful.

I cordially thank Michaela Wäscher and Beate Schwertfeger for their kind advice concerning administrative issues and their engagement.

I thank the members of the graduate school GK 726 for inspiring discussions and a nice time in Riezlern.

The DFG is gratefully acknowledged for financing this project and for the possibility to participate in the priority program "Photonic Crystals".

Finally, I want to thank my family for great support, continuous encouragement and help at any time.